

# The Nansen Environmental and Remote Sensing Center



*a non-profit  
research institute affiliated with  
the University of Bergen*

*Thormøhlensgate 47,  
N-5006 Bergen  
Norway*


**NERSC Technical Report no. 397**

## **ESA PRODEX ISAR**

FINAL REPORT

by

**Morten Wergeland Hansen, Harald Johnsen, Geir Engen, Jeong-Won  
Park, and Artem Moiseev**

	<p><b>Nansen Environmental and Remote Sensing Center (NERSC)</b>          Thormøhlensgate 47          N-5006 Bergen, Norway          Phone: + 47 55 20 58 00          Fax: + 47 55 20 58 01          E-mail: <a href="mailto:post@nersc.no">post@nersc.no</a>  <a href="http://www.nersc.no">http://www.nersc.no</a></p>
---	--

<p><b>TITLE:</b> Improved knowledge of high latitude ocean circulation with Synthetic Aperture Radar (ISAR)</p>	<p><b>REPORT IDENTIFICATION:</b> 397</p>
<p><b>CLIENT:</b> European Space Agency</p>	<p><b>CONTRACT:</b> Prodex Arrangement No 4000108820</p>
<p><b>CLIENT REFERENCE:</b> C4000108820</p>	<p><b>AVAILABILITY:</b> Internal</p>
<p><b>INVESTIGATORS:</b> Morten W. Hansen Harald Johnsen (Norut) Geir Engen (Norut) Jeong-Won Park Artem Moiseev</p>	<p><b>AUTHORISATION:</b> Sebastian Mernild</p>
	<p><b>DATE:</b> 2018-11-01</p>
<p><b>SUMMARY:</b> The synthetic aperture radar (SAR) Doppler centroid shift has been demonstrated to contain geophysical information about sea surface wind, waves and current at an accuracy of 5 Hz and pixel spacing of 3.5 – 9 × 8 km<sup>2</sup>. This corresponds to a horizontal surface velocity of about 20 cm/s at 35° incidence angle. The ESA Prodex ISAR project aims to implement new and improved SAR Doppler shift processing routines to enable repro-</p>	

cessing of the wide swath acquisitions available from the Envisat ASAR archive (2002-2012) at higher resolution and better accuracy than previously obtained, allowing combined use with Sentinel-1 and Radarsat-2 retrievals to build timeseries of the sea surface velocity in the Nordic Seas.

This project has addressed the calibration and validation of geophysical Doppler shifts from Envisat ASAR Doppler centroid shift retrievals. The main focus has been the challenges related to estimation of geometric (satellite orbit and attitude) and electronic (antenna mis-pointing) contributions and corrections. Geophysical Doppler shifts from approximately three months of data in January, February and March 2010 have been analyzed with the goal of establishing a global calibration algorithm. At 8 km pixel spacing, the uncertainty of the retrieved geophysical Doppler shift is then about 2.5 Hz in subswaths 2-5, and 3.5 Hz in subswath 1. This is half the uncertainty of previous results. Following this, new and improved routines for near-surface wind and current retrieval in the Nordic Seas have been developed, and a validation framework has been established. The preliminary results are then presented.

Prodex ISAR  
Contract no. 4000108820  
Final report

Morten Wergeland Hansen<sup>1</sup>, Harald Johnsen<sup>2</sup>, Geir Engen<sup>2</sup>,  
Jeong-Won Park<sup>1</sup> and Artem Moiseev<sup>1</sup>

<sup>1</sup>Nansen Environmental and Remote Sensing Center, Bergen,  
Norway.

<sup>2</sup>Norut, Tromsø, Norway.

2018-11-01

**Abstract**

The synthetic aperture radar (SAR) Doppler centroid shift has been demonstrated to contain geophysical information about sea surface wind, waves and current at an accuracy of 5 Hz and pixel spacing of  $3.5 - 9 \times 8 \text{ km}^2$ . This corresponds to a horizontal surface velocity of about 20 cm/s at  $35^\circ$  incidence angle. The ESA Prodex ISAR project aims to implement new and improved SAR Doppler shift processing routines to enable reprocessing of the wide swath acquisitions available from the Envisat ASAR archive (2002-2012) at higher resolution and better accuracy than previously obtained, allowing combined use with Sentinel-1 and Radarsat-2 retrievals to build timeseries of the sea surface velocity in the Nordic Seas.

This project has addressed the calibration and validation of geophysical Doppler shifts from Envisat ASAR Doppler centroid shift retrievals. The main focus has been the challenges related to estimation of geometric (satellite orbit and attitude) and electronic (antenna mis-pointing) contributions and corrections. Geophysical Doppler shifts from approximately three months of data in January, February and March 2010 have been analyzed with the goal of establishing a global calibration algorithm. At 8 km pixel spacing, the uncertainty of the retrieved geophysical Doppler shift is then about 2.5 Hz in subswaths 2-5, and 3.5 Hz in subswath 1. This is half the uncertainty of previous results. Following this, new and improved routines for near-surface wind and current retrieval in the Nordic Seas have been developed, and a validation framework has been established. The preliminary results are then presented.

## Contents

<b>1</b>	<b>Introduction</b>	<b>2</b>
<b>2</b>	<b>Work packages</b>	<b>5</b>
2.1	WP1: Management . . . . .	5

2.2	WP2: Implementation, testing and operation of Norut's GSAR processor for Envisat ASAR . . . . .	6
2.3	WP3: Improvement of existing wind and ice retrieval schemes . .	8
2.4	WP4: Accuracy assessment and validation . . . . .	8
<b>3</b>	<b>Software developed in the project</b>	<b>8</b>
3.1	Doppler centroid shift estimator for Envisat ASAR . . . . .	8
3.2	OpenWind - a python package for estimating high resolution wind from SAR images . . . . .	10
3.3	Search, access, and analysis routines for geospatial datasets . . .	11
3.3.1	Geo-SPaaS . . . . .	11
3.3.2	Nansat ingestor for satellite EO raster datasets . . . . .	13
3.3.3	HF-radar . . . . .	15
3.3.4	Surface Lagrangian drifters . . . . .	17
3.3.5	NOAA wind buoys . . . . .	19
<b>4</b>	<b>SAR Doppler centroid terms and geophysical requirements</b>	<b>19</b>
4.1	Geophysical term . . . . .	19
4.2	Geometric term . . . . .	21
4.2.1	Satellite attitude . . . . .	22
4.2.2	Surface topography . . . . .	23
4.3	Electronic term . . . . .	24
4.3.1	Antenna gain variations . . . . .	24
4.3.2	Gain differences between antenna elements . . . . .	25
4.4	Residual error . . . . .	25
<b>5</b>	<b>Results and validation</b>	<b>26</b>
5.1	Bayesian wind retrieval . . . . .	29
5.2	Sea ice drift . . . . .	31
5.3	Sea surface current . . . . .	32
5.4	Initial investigations on wave-bias retrieval from WV mode . . .	35
<b>6</b>	<b>Conclusion</b>	<b>35</b>
	<b>Appendices</b>	<b>39</b>
<b>A</b>	<b>Prodex DESICE final report</b>	<b>39</b>

## 1 Introduction

The warm and saline surface Atlantic Water (AW) flowing into the Nordic Seas across the Greenland-Scotland ridge transports heat into the Arctic, maintaining the ice-free oceans and regulating sea-ice extent. The AW influences the region's relatively mild climate and is the northern branch of the global thermohaline overturning circulation. Heat loss in the Norwegian Sea is key for both heat transport and deep water formation. In general, the ocean currents in the Nordic Seas and the North Atlantic Ocean is a complex system of topographically steered barotropic and baroclinic currents of which the wind stress and its variability is a driver of major importance.

The upper ocean circulation, including wave-generated Stokes and wind drift, is an important component of the ocean dynamics. In the Nordic seas, this was early mapped by tracing drifting objects, and since the early 1990s, standardization of drifting buoys and associated international buoy campaigns enabled thorough analyzes related to the increasing concern for climate change in the 80s and 90s [1, 2, 3, 4]. Over the past few decades, satellite observations have also become important sources of information for our knowledge of the ocean surface circulation.

The only single operational method for measuring ocean currents from satellite employs sea surface height (SSH) measurements from radar altimetry. This method exploits the equilibrium between the Coriolis force and pressure caused by large-scale surface slope relative to the Earth's equipotential surface, or geoid, to calculate surface geostrophic current. However, the resolution in these products is limited to about 50 km, and mesoscale variability on the order of 10-100 km is not sufficiently covered, neither from satellite nor from in-situ measuring instruments. For example, the quality of the geostrophic current measured with altimetry is limited by both spatial resolution, reduced accuracy in shallow water and interference from land within 30-50 km of the coast. In comparison, in-situ measurements (e.g., from anchored current meters, ADCP, drifting buoys) are often scattered, with low spatial resolution, but high accuracy and good resolution in time. During the past 10-20 years, two new methods for calculating surface velocity with SAR have been developed. One method, called Along Track Interferometry (ATI), requires two receiver antennas [5, 6, 7], while the second method allows speed estimates of reduced resolution from a single antenna [8, 9, 10]. Both methods exploit the doppler shift resulting from the relative velocity between the radar and the sea surface.

Several recent publications (e.g., [11, 12, 13, 14, 15, 16, 17]) have confirmed and further demonstrated the geophysical value of the Doppler centroid shift,  $f_{Dc}$ , recorded with Synthetic Aperture Radar (SAR) for sea surface wind and current retrieval. As a result,  $f_{Dc}$  and the derived geophysical Doppler shift,  $f_g$ , are now standard products of the Sentinel-1 SAR instruments.

The wave contribution to the geophysical range Doppler shift is strongly related to wind speed and direction. Therefore, in order to calculate the ocean surface flow, the measured Doppler shift must be split into contributions from wind-waves and current, respectively. Fig. 1 shows the zonal component of the mean flow in the Nordic Seas between 2007 and 2011 from Envisat ASAR after subtraction of the contributions from wind-waves as demonstrated at the SeaSAR conference in 2012 [14]. The uncertainty in this component is down to 2 cm/s in the best covered areas, although some sampling related biases are expected. The uncertainty in the original single-scene retrievals is, however, much less: 5 Hz uncertainty in the total geophysical Doppler shift at a pixel spacing of 3.5-9×8 km<sup>2</sup>. This corresponds to a horizontal surface velocity of about 20 cm/s at 35° incidence angle.

A survey conducted in the ESA project GlobCurrent [18] summarizes the following user needs for information on ocean surface currents:

- A majority of users want global current data
- The spatial resolution should be 1-2 km in coastal areas and 10-25 km for

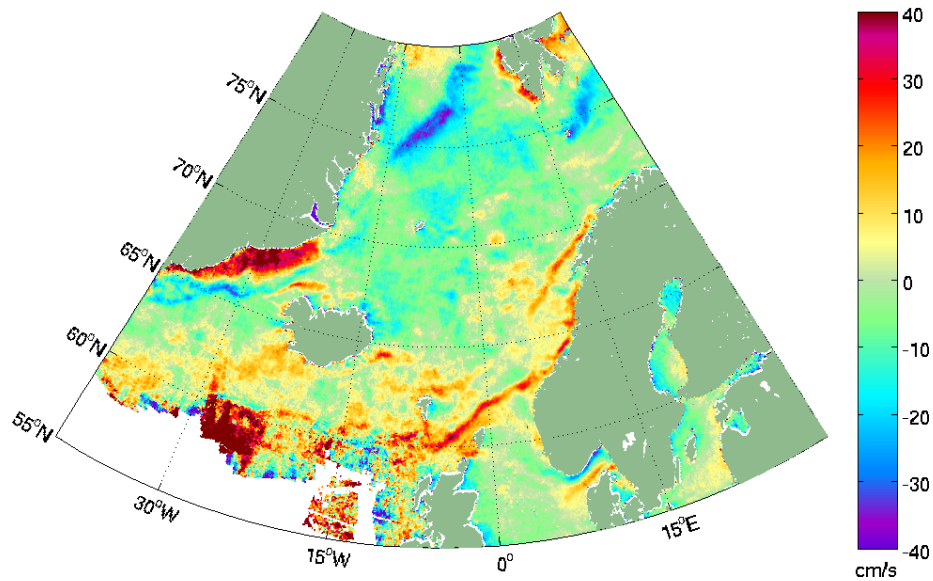


Figure 1: The zonal surface velocity component retrieved from Envisat ASAR range Doppler velocity measurements between 2007 and 2011 (from [14]).

open ocean

- The time resolution should be between one hour and one day
- The speed uncertainty should be between 5 and 30 cm/s and must be specified per data pixel
- Time series of 10 to 20 years are desired
- The majority of users want access to data in near real-time
- All data products should be compatible with the NetCDF-CF (Climate and Forecast variables) standard
- Quantification of contributions from Stokes and Ekman drift, and tidal currents is needed

To reach these goals, the SAR Doppler processing must be optimized – both for generation of timeseries, and for single-scene usage. Eventually, very large volumes of archived data should be analyzed to provide valuable near-surface wind and current information to be used in both climate research and operational oceanography.

The main goal of this project was to generate and deliver a new high-resolution dataset of the yearly, seasonal and monthly mean ocean circulation in the Nordic Seas from 2002 to 2012. In combination with radar altimetry data and GOCE based geoid estimates, this would then be used to estimate a new high-resolution Mean Dynamic Topography (MDT) for the region. In turn, this would help to advance the understanding of the regional ocean dynamics and energy content to validate ocean models, and extend assimilation systems.

In retrospect, these were very ambitious goals that in principle were unattainable given the size of the project. In particular, the need for software tools for proper data analysis involving many different types of observations and huge amounts of SAR data has caused delays in the project execution. To handle the processing and analysis in the most general and efficient way, the Nansat [19] and Geo-SPaaS tools have been developed in collaboration with other projects. Nansat and the core of Geo-SPaaS are open-source and available from GitHub (see <https://github.com/nanscenter/nansat> and <https://github.com/nanscenter/django-geo-spaas>). The software tools are presented in section 3. Also, challenges related to data access and calibration forced us to focus on only a short observation period of 2-3 months in 2010 from Envisat ASAR. However, this research has resulted in a much better understanding of the various contributions to the SAR range Doppler centroid shift and its geophysical calibration, as presented in section 4. Preliminary results in retrieval of high-resolution wind, sea ice drift, and sea surface current are presented in section 5. Concluding remarks are provided in section 6. In addition to this, a project management report is given in section 2.

## 2 Work packages

### 2.1 WP1: Management

There have been 6 project meetings including the project kick-off meeting at the ESA Living Planet Symposium in Edinburgh on 12 September 2013. A progress report was issued in May 2014.

The project officially finished in August 2017 after two extensions. Some remaining work has been performed after that with support from the projects “Upper ocean circulation in the Nordic Seas from the Sentinel and Earth Explorer satellites” (uSeaSat), funded by the Norwegian Research Council, “Drift Estimation of Sea Ice in the Arctic Ocean and sub-Arctic Seas” (DESIce) funded through the ESA Prodex program, and the Geo-SPaaS SIS project. The latter is a NERSC strategic institute commitment project funded via the national basic funding for environmental research institutes.

The list of action items agreed at project meetings is provided in Table 1. Detailed comments about each item are provided in the meeting minutes that are attached. Five of these action items have been canceled, and one has been changed.

To enable proper analysis of land reference data needed for calibration, we decided to focus on a limited period of global Envisat ASAR WSM acquisitions. As such, [AI-15], which focused on the Agulhas region only, is invalid. With the new calibration algorithm zonal and meridional current components from both ascending and descending pass in the Agulhas Current and the Gulf Stream can be estimated. The higher signal-to-noise ratio (SNR) in these regions make them excellent sites for assessing the 2-dimensional mean current retrieval. The weak currents (i.e., low SNR) in the Nordic Seas, however, cannot be adequately estimated for this short time period. The results are presented in section 5.3.



Since few consistent results were available at the time, the yearly reports were canceled in favor of focusing on further research and development ([AI-16] and [AI-22]).

Use of Alternating Polarization (AP) data for inspecting biases ([AI-17]) was not necessary. The biases could be analyzed and corrected using Wide Swath Mode (WSM) products, as described in section 4.

The peer reviewed papers planned in [AI-20] and [AI-21] have been postponed due to a very time consuming data collection and analysis of WSM data in January, February and March 2010. The papers are planned as follow-up tasks.

The project related work and results have been presented at the following conferences:

- World Ocean Science Congress, Kochi, Kerala, India, 5-8 February 2015
- ESA EO Open Science Conference, Frascati, Italy, 12-16 September 2016
- ESA Big Data from Space (BiDS), Santa Cruz de Tenerife, Spain, 15-17 March 2016
- ESA Living Planet Symposium, Prague, Czech Republic, 9-13 May 2016
- ESA GlobCurrent User Consultation Meeting, 21-23 March 2017
- EGU General Assembly, Vienna, Austria, 23-28 April 2017
- OSGeo FOSS4G-NO, Oslo, Norway, 31 August 2017
- ESA EO Open Science 2.0, Frascati, Italy, 25-28 September 2017
- EuroGOOS International Conference: Operational Oceanography serving sustainable marine development, Bergen, Norway, 3-5 October 2017
- ESA SeaSAR 2018, Frascati, Italy, 7-10 May 2018
- EUSAR 2018, Aachen, Germany, 4-7 June 2018

## **2.2 WP2: Implementation, testing and operation of Norut's GSAR processor for Envisat ASAR**

The GSAR processor was installed at NERSC in April 2015 with processing ability for ASAR Alternating Polarization (AP) mode. An extension of the software to also include Wide Swath (WS) mode processing was added in September 2015. Level-0 ASAR WS scenes over the Nordic Seas from January, February and March 2010 have been analyzed at NERSC. The results are presented in section 4 and 5. The GSAR WV processor was delivered to NERSC at the end of the project.

NORUT's main contribution to the project has been fulfilled, and remaining calibration and error correction of slightly less than 3 months of WSM acquisitions was performed with post-processing software at NERSC.

Table 1: Action items

	Date opened	Action	Date closed
[AI-1]	2013-09-12	MWH to order (initial) raw data by the end of September	2014-10-20
[AI-2]	2013-09-12	MWH to develop Sentinel-1 reader software by December 2013	2014-10-20
[AI-3]	2013-09-12	HJ to send example NetCDF to MWH for reader development by September 2013	2014-10-20
[AI-4]	2013-09-12	YL to work on the ASAR processor by December 2013	2014-10-20
[AI-5]	2013-09-12	EAH to check with his contacts in ESA regarding data quota and need for proposal submission to get more ASAR level-0 data	2014-10-20
[AI-6]	2013-09-12	Based on response to EAH from ESA MWH will request an extended quota	2014-10-20
[AI-7]	2013-09-12	MWH to order WS, IM and AP mode level-0 data over the Agulhas Current region	2014-10-20
[AI-8]	2014-02-27	NORUT to finish the Doppler processor and provide software and installation instructions to NERSC	2015-09-30
[AI-9]	2013-09-12	Duplicate of AI-2	2014-10-20
[AI-10]	2013-09-12	NERSC needs an IDL license	2015-06-16
[AI-11]	2013-09-12	Python version of CDOP	2014-10-20
[AI-12]	2014-02-27	MWH to implement the Bayesian algorithm of Mouche et al. 2012 in OpenWind ( <a href="https://github.com/nanscenter/openwind">https://github.com/nanscenter/openwind</a> )	2015-06-16
[AI-13]	2014-02-27	Start of WP4 when AI-8 is completed	2016-04-28
[AI-14]	2014-02-27	First progress report	2014-05-08
[AI-15]	2014-02-27	MWH to start processing VV polarization data in ascending pass over the Agulhas Current	Changed
[AI-16]	2014-02-27	MWH to organize progress report by February/March in preparation for the next project meeting	Canceled
[AI-17]	2015-06-16	MWH to order AP data over land for inspecting the range bias dependence on time and latitude	Canceled
[AI-18]	2015-06-16	MWH to start initial tests of the new Doppler product in OpenWind by the end of August	2018-11-01
[AI-19]	2015-06-16	MWH to gather wind validation data from in-situ platforms by the end of August	
[AI-20]	2015-06-16	HJ to outline and lead the technical paper by mid September	Postponed
[AI-21]	2015-06-16	MWH to outline and lead the surface currents paper by mid September	Postponed
[AI-22]	2015-06-16	MWH to initiate the yearly report by mid August	Canceled
[AI-23]	2015-06-16	MWH to plan the next meeting by mid September	2016-04-28
[AI-24]	2016-12-06	Transfer of 50 K€ to Norut to implement WV processing capability to the NERSC GSAR installation	2018-11-01?

The processing software is now being installed at the ESA G-POD services in order to process the full Envisat WSM archive following the procedures described in section 4.

### **2.3 WP3: Improvement of existing wind and ice retrieval schemes**

The work has consisted in further development of the Nansat (<https://github.com/nanscenter/nansat>) and OpenWind (<https://github.com/nanscenter/openwind>) software tools to allow use of the Bayesian minimization algorithm. The full integration of Doppler shift (level-0 products processed in GSAR), NRCS (level-1b products), and model wind field information from numerical models is implemented in the last development version of OpenWind.

Demonstrations of ice drift measurements with the SAR Doppler shift have been presented at the project meetings, and in the ESA Prodex DESIce project.

### **2.4 WP4: Accuracy assessment and validation**

The calibration, accuracy assessment and validation of the geophysical range Doppler shift is enabled by the Geo-Scientific Platform as a Service (Geo-SPaaS) [20]. Geo-SPaaS integrates local and remote data access and analysis tools in pre-configured virtual machines (vm's), e.g., for the Prodex ISAR project. The vm's can be installed on user computers such that several colleagues can work on the exact same system. The Geo-SPaaS data model follows international standards, including NASA DIF and GCMD keywords and the NetCDF-CF standard. The software behind the Geo-SPaaS is open-source, and available at <https://github.com/nanscenter/geo-spaas-vagrant>. Geo-SPaaS is presented in section 3.3.

Comparative validation of the new (processed with GSAR) versus the old (following the method described in [21]) ASAR Doppler retrievals were performed in connection to the Living Planet Symposium in May 2016. Further validation results are presented in Section 4. Due to challenges with calibration and error corrections (section 4), the accuracy and validation results are only preliminary and needs follow-up work. This will be done in the uSeaSat project funded by the RCN and also include results from the G-POD processing at ESA.

## **3 Software developed in the project**

### **3.1 Doppler centroid shift estimator for Envisat ASAR**

The Doppler centroid estimation algorithm implemented for ASAR is based on using single look complex (SLC) data, similar to the method described in [22], but extended to correct the azimuth spectra for energy aliased from neighboring areas (side-band effects). In case of raw data (RAW), a SAR focusing is integrated into the processing chain and performed as part of the Doppler

estimation. The high-precision Doppler frequency is thus estimated from a full-bandwidth processed SLC image with no windowing applied to the data, enabling the correction of side-band errors (i.e., aliasing). The ASAR Doppler algorithm follows the basics of the corresponding Sentinel-1 Level 2 algorithm. A detailed algorithm specification of this can be found in [23].

The algorithm models the expectation value of the azimuth spectra in terms of covariance coefficients over range of frequency bands taking into account the antenna coefficients, the true intensity and the white noise (thermal and quantization) contribution. The first order coefficient of the model is solved simultaneously with respect to phase providing an estimate of Doppler offset (i.e., centroid), and to envelope providing an estimate of the unbiased (noise corrected) intensity. The model is also used to calculate the standard deviation of the Doppler centroid estimate. The model of the azimuth spectrum of the complex SAR image is given by

$$P(\varpi; \mathbf{t}) = \sum_j \bar{I}(\mathbf{t} - \Delta\mathbf{t}_j) D^{(j)}(\varpi - \varpi_{dc}(\mathbf{t} - \Delta\mathbf{t}_j)) + b(\mathbf{t}) \quad (1)$$

Here,  $\bar{I}$  is the average target intensity inside the estimation area,  $\varpi_{dc}$  is the Doppler centroid frequency,  $b(\mathbf{t})$  is the additive noise, and  $D^{(j)}$  are the antenna profiles for each of the PRF-bands (indexed by  $j$ ) aliasing together. The 2D time variable  $\mathbf{t}$  is the center position of the sub-area in the SLC from where the azimuth direction spectrum is estimated, and  $\Delta\mathbf{t}_j$  are the 2D time offsets to the location of the different intensity contributions ( $\Delta\mathbf{t}_0 \equiv 0$  represent the position to the true intensity and  $\Delta\mathbf{t}_{j \neq 0}$  represents the position to ghost image intensities). The range direction component of  $\Delta\mathbf{t}_j$  is the range-migration and the azimuth component is  $j$ -times the PRF divided by the Doppler rate [24]. The corresponding first order inverse Fourier coefficients can be written as:

$$p_1(\mathbf{t}) = \sum_j f(\mathbf{t} - \Delta\mathbf{t}_j) d_1^{(j)} \quad (2)$$

where  $f(\mathbf{t}) \equiv \bar{I}(\mathbf{t}) e^{i\varpi_{dc}(\mathbf{t})\Delta\tau}$  provides estimate of the Doppler frequency,  $\varpi_{dc}$  and the true image intensity,  $\bar{I}$ . Inversion of (2) with respect to  $f$  is easily done by Fourier transforming the equation and introducing the Fourier transform  $\hat{p}_1$  of  $p_1$  with respect to the estimation position  $\mathbf{t}$ , yielding:

$$f(\mathbf{t}) = \frac{1}{(2\pi)^2} \iint d e^{i\cdot\mathbf{t}} \frac{\hat{p}_1(\cdot)}{\sum_j d_1^{(j)} e^{-i\cdot\Delta\mathbf{t}_j}} \quad (3)$$

The algorithm provides a fast and easy way to solve for Doppler frequency and true intensity, and simultaneously correcting for errors caused by aliasing of intensity from side-bands.

The Doppler frequency estimated from the single-look complex data consist in general of several terms:

$$\varpi_{dc} = \varpi_{dc}^{phys} + \varpi_{dc}^{geo} + \varpi_{dc}^{elec} + \Delta\varpi_{dc} \quad (4)$$

where  $\varpi_{dc}^{phys}$  is the geophysical term,  $\varpi_{dc}^{geo}$  is the geometric term,  $\varpi_{dc}^{elec}$  is the antenna electronic miss pointing, and  $\Delta\varpi_{dc}$  is the residual Doppler error coming

from unknown sources (for instance such effects as described in Section 3.3.2). The calibration of  $\varpi_{dc}$  consists in predicting and removing the last three terms on right hand side of (4) such that only the geophysical term,  $\varpi_{dc}^{phys}$  is left. The various terms contributing to (4) are described in detail in Section 4. Some performance results of the algorithm applied on ASAR SM data can be found in [25].

### 3.2 OpenWind - a python package for estimating high resolution wind from SAR images

The OpenWind python software has been prepared with a standard CMOD5 algorithm to produce high-resolution wind speed using wind direction from numerical wind forecast models (e.g., NCEP, HIRLAM, and AROME). In addition to the CMOD wind retrieval algorithm, a Bayesian wind inversion scheme following [15] has been implemented in OpenWind. This algorithm exploits all available wind information including model wind vectors ( $\mathbf{u}$ ), SAR NRCS ( $\sigma_0$ ) and geophysical Doppler shift ( $f_g$ ).

[15] concluded that the use of the SAR geophysical Doppler shift,  $f_g$ , could add noise to lower the performance of the inversion scheme when the forecast wind field and the NRCS,  $\sigma_0$ , are very consistent, but that its high sensitivity to the wind direction is useful to retrieve more realistic wind patterns in cases of complex and rapidly varying meteorological situations. The problem with this conclusion is the use of constant error estimates ( $\Delta\sigma_0 = 0.5\text{dB}$ ,  $\Delta f_g = 5\text{Hz}$ , and  $\Delta\mathbf{u} = [3, 3] \text{ m/s}$ ). Obviously, the uncertainty of a model forecast is lower in areas of uniform wind, and higher in frontal regions. Spatial variability of the relation between SAR observables ( $\sigma_0$  and  $f_g$ ) and the general wind field, e.g., due to rain, is also clearly an issue that should be considered. In this respect, the simple solution in OpenWind is to allow spatially variable uncertainties of  $f_g$  and  $\mathbf{u}$  by estimating their local spatial variance, including a lower limit of  $\Delta f_g = 5 \text{ Hz}$  and no lower limit for  $\mathbf{u}$ . For the NRCS, OpenWind applies an error factor of 7.8% as suggested by [26], i.e.,  $\Delta\sigma_0 = 0.078\sigma_0$ . Figure 2 shows the wind field derived from a Sentinel-1A acquisition over the southern part of the Norwegian Sea using the standard CMOD algorithm and the Bayesian inversion method without Doppler shift information. The effective use of the Bayesian methodology is evident in the reduced wind speed at the north-western and eastern parts of the inversion based result. This demonstrates that the OpenWind algorithm works technically. However, further investigations are required to establish the uncertainty estimations and to validate the method in comparison to other wind retrievals (e.g., wind measuring buoys). Wind retrievals from Envisat ASAR acquisitions also using Doppler shift information are presented in section 5 together with a limited evaluation in comparison to a NOAA wind measuring buoy dataset.

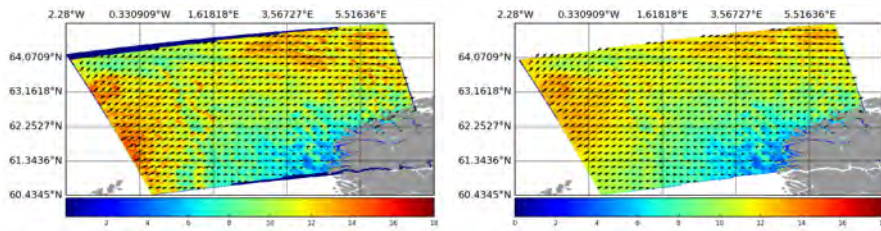


Figure 2: Wind field over the southern Norwegian Sea from a Sentinel-1A acquisition on 29th December, 2014, at 17:19 UTC. The left panel shows the CMOD wind (10 m height above sea level, and 500 m pixel size), and the right panel shows the wind field resulting from Bayesian inversion using NCEP model forecast wind and SAR NRCS.

### 3.3 Search, access, and analysis routines for geospatial datasets

To be able to efficiently post-process, calibrate, and analyze the SAR range Doppler shifts we have developed a generic data and workflow management system called Geo-Scientific Platform-as-a-Service (Geo-SPaaS). A generic geospatial data catalog is, here, coupled with the Nansat Python toolbox for processing and analyzing 2D satellite earth observation data.

As part of the Prodex ISAR project, the following datasets can now be accessed with Geo-SPaaS:

- Envisat ASAR range Doppler shift
- Envisat ASAR NRCS
- HF-radar
- Surface Lagrangian drifters from the Surface Velocity Program (SVP)
- In-situ wind measurements from NOAA NDBC standard meteorological buoys
- QuikSCAT and ASCAT wind measurements

#### 3.3.1 Geo-SPaaS

Geo-SPaaS builds on the NORMAP and NMDC infrastructure projects under the Norwegian Research Council (NRC) for satellite Earth observation data and marine in-situ observations. We adopt the same design objectives as in NORMAP, plus some extra objectives regarding the use of this data in data analysis and processing tools. The NORMAP design objectives (from the NORMAP System Design Document version 0.3) are summarized in Table 2.

The Geo-SPaaS concept is inspired by standard cloud computing service models, i.e., Infrastructure as a Service (IaaS), Platform as a Service (PaaS), and Software as a Service (SaaS). These models typically serve to improve software development speed, allowing the user to focus on the application itself, and to

Table 2: NORMAP design objectives, adopted in Geo-SPaaS.

Objective	Comment
Cost effective	The system should be cost efficient to develop, implement and maintain over time ensuring a sustainable system.
Expandable	The system should be easy to expand with additional storage capacity, bandwidth, etc.
Interoperable	The system should be able to interact with emerging international scientific data management systems like INSPIRE, WMO Information System, ESA LTDP, GEOSS, GCMD etc.
Modular	The system should be modular in design allowing modules with well defined functionality and interfaces to be changed during the lifetime of the system.
Reliable	The system should be reliable and stable during operation.
Secure	The system should ensure integrity of the data handled and document this for the users of the system.
Usable	The system should be intuitive to use for end users as well as for system operators.

reduce costs by outsourcing hardware and software maintenance to the service provider. As such, Geo-SPaaS shall help reducing the time and effort that scientists have to spend searching for data, and to develop their own tools for processing and analysis.

Geo-SPaaS integrates existing tools and data repositories. The software layers supporting this interoperability are implemented as modular open source components, allowing the whole system to be open, extendable and scalable. The design objectives are accomplished by integrating already developed tools to allow easy access to the data in a single platform. Employing the interactive tools for efficient prototyping, testing and operationalization of multi-sensor synergistic algorithms, is thus simplified.

The central part of Geo-SPaaS is the metadata catalog defined in the Django-Geo-SPaaS software package. This organizes granular metadata describing the structure, location and content of available satellite, model and in situ datasets. Information is stored in a relational database. The core table in the database aggregates the most common information relevant for each dataset, including spatial and temporal coverage (start/stop date, geographical reference, resolution, etc.), physical file name and access protocols (e.g. local file system or FTP or OpenDAP, etc.), and the source of the data (satellite/sensor or model, etc). More specific metadata, which is relevant to only a few datasets, is stored in separate tables linked to the core table.

The data access protocols provide seamless access to data from local and remote repositories, viewed as a single virtual distributed file system integrated with the tools, so that any Geo-SPaaS user's local data repository is virtually merged into a single shared distributed data archive. This data archive can contain all levels of satellite data, as well as model and in-situ data.

The data storage and access framework is aligned with international interoper-

erability efforts as described through the INSPIRE, WMO Information System (WIS) and GEOSS specifications. This ensures easy and open data access for the researchers. Existing infrastructures (see the following sections) are integrated employing internationally approved interoperability standards (e.g. OpeNDAP, OGC WCS, OGC CSW, ISO23950, ISO19115), favouring a distributed system. Geo-SPaaS supports metadata in accordance with CEOS IDN DIF and the GCMD Science Keywords, and adheres to the data design requirements in NORMAP and NMDC.

Geo-SPaaS has in part been developed to satisfy requirements in the Prodex ISAR project, and partly with funding from this project. It is used for the calibration of the geophysical Doppler shift employing data from multiple global acquisitions, as described in section 4. Furthermore, Geo-SPaaS is used for collocation of SAR geophysical Doppler shift data with auxiliary complementary data used both in validation and specific algorithms such as wind field and ice drift retrieval.

### 3.3.2 Nansat ingestor for satellite EO raster datasets

The generic approach of Geo-SPaaS and its coupling to Nansat allows simple management of any raster dataset readable by Nansat [19]. Any dataset that can be opened with Nansat is thus easily ingested to the database by a simple Python/Django bash command:

```
$ ./manage.py ingest <filename>
```

For the SAR Doppler processing and analysis, the following datasets are most relevant:

- Envisat ASAR level-1b scenes from the NERSC data archive (<http://sat.nersc.no>; GSAR does not provide calibrated NRCS)
- Numerical Weather Prediction (NWP) forecast and reanalysis wind fields from, e.g., NCEP, HIRLAM, AROME, ECMWF
- Satellite scatterometer wind fields, e.g., ASCAT
- Sea Surface Temperature from the Operational Sea Surface Temperature and Sea Ice Analysis (OSTIA) project
- Surface current products from the ESA GlobCurrent project

Collocation of example datasets with the SAR Doppler retrievals is done as follows (the actual data is shown in Figure 3):

```
import matplotlib.pyplot as plt
import numpy as np

from nansat.nansat import Nansat
from nansat.domain import Domain
from nansat.nsr import NSR

from django.utils import timezone
from django.contrib.gis.geos import WKTRReader

from geospaas.utils import nansat_filename
```



```

from geospaas.catalog.models import Dataset, DatasetURI

# Define region of interest (Agulhas Current)
d = Domain(NSR().wkt, '-te_10_-44_40_-30_-tr_0.125_0.125 ')
geometry = WKTReader().read(d.get_border_wkt(nPoints=1000))

# Define time of interest
start_time = timezone.datetime(2010,1,13,20,30,0,
                               tzinfo=timezone.utc)
end_time = timezone.datetime(2010,1,13,21,30,0,
                              tzinfo=timezone.utc)

# Find Doppler datasets
dop = Dataset.objects.get(
    entry_title__contains = 'Doppler',
    time_coverage_start__gt = start_time,
    time_coverage_end__lt = end_time,
    geographic_location__geometry__intersects = geometry)

# Find ASAR level-1b datasets
nracs = Dataset.objects.get(
    dataseturi__uri__contains='N1',
    time_coverage_start__gt = start_time,
    time_coverage_start__lt = end_time,
    geographic_location__geometry__intersects = geometry)

# Find NCEP NWP model wind field datasets
ncep = Dataset.objects.filter(
    source__platform__short_name = 'NCEP-GFS',
    time_coverage_start__gt =
        start_time - timezone.timedelta(hours=3),
    time_coverage_end__lt =
        end_time + timezone.timedelta(hours=3))[0]

# Find METOP-A ASCAT scatterometer datasets
scat = Dataset.objects.filter(
    source__instrument__short_name = 'ASCAT',
    time_coverage_start__gt =
        start_time - timezone.timedelta(hours=12),
    time_coverage_end__lt =
        end_time + timezone.timedelta(hours=12),
    geographic_location__geometry__intersects = geometry)

# Find GlobCurrent datasets
gc = Dataset.objects.get(
    entry_title__contains = 'globcurrent',
    time_coverage_start__gt =
        start_time - timezone.timedelta(hours=24),
    time_coverage_end__lt =
        end_time + timezone.timedelta(hours=24),
    geographic_location__geometry__intersects = geometry)

# Access data using Nansat
# Comments:
#         - nansat_filename() transforms the uri to
#           a regular filename (string),
dop0 = Nansat(nansat_filename(dop.dataseturi_set.get(
    uri__contains='subswath0').uri))
# ..
nracs = Nansat(nansat_filename(
    asar_llb.dataseturi_set.get().uri))
ncep_wind = Nansat(nansat_filename(

```

```

nscat0 = Nansat(
    ncep.dataseturi_set.get().uri))
nscat0 = Nansat(
    nansat_filename(scats[0].dataseturi_set.get().uri),
    quartile=scats[0].extrametadataset.get().quartile)
# - to simplify collocation with other data, each
# scatterometer file is split into 4 datasets in
# the geospaas catalog
nscat1 = Nansat(
    nansat_filename(scats[1].dataseturi_set.get().uri),
    quartile=scats[1].extrametadataset.get().quartile)
ngc = Nansat(gc.dataseturi_set.get().uri)

# Reproject the datasets to region of interest
dop0.reproject(d)
# and so on..

# Plot the fields of interest
from nansatmap.nansatmap import Nansatmap

fontsize = 8
plt.close('all')

nmap = Nansatmap(d, figsize=(8,10), resolution='i')
nmap.fig.tight_layout(pad=0)
nmap.pcolormesh(dop0['fdg'], vmin=-60, vmax=60)
nmap.pcolormesh(dop1['fdg'], vmin=-60, vmax=60)
nmap.pcolormesh(dop2['fdg'], vmin=-60, vmax=60)
nmap.pcolormesh(dop3['fdg'], vmin=-60, vmax=60)
nmap.pcolormesh(dop4['fdg'], vmin=-60, vmax=60)
nmap.draw_continents(zorder=0)
nmap.draw_meridians(np.arange(-180,180,10), labels=[0,1,1,0],
    fontsize=fontsize)
nmap.draw_parallels(np.arange(-90,90,5), labels=[1,0,0,1],
    fontsize=fontsize)
nmap.draw_coastlines(linewidth=0.5)
divider = make_axes_locatable(plt.gca())
cax = divider.append_axes("right", size="5%", pad=0.05)
cbar = nmap.fig.colorbar(plt.gcf(), cax=cax)
cbar.set_label('Geophysical_Doppler_shift_[Hz]',
    fontsize=fontsize)
nmap.fig.savefig(<filename>, bbox_inches='tight', pad_inches=0.1,
    dpi=300)

# and so on.. See Figure 3.

```

### 3.3.3 HF-radar

High frequency (HF) radar systems provide measurements of ocean surface currents at coastal domains (up to 200 km away from a coastline) in near real time. Thanks to a high temporal (about 1-hour averages) and spatial (in range from 500 m to 6 km depending on the radar frequency) resolution, HF-radars can be used for a range of applications, such as studies of ocean surface currents, waves and tides, water quality monitoring, marine navigation, and search and rescue operations.

Radial velocities obtained by HF-radars could also be used for validation of SAR range Doppler shift measurements. A Geo-SPaaS HF-radar ingestor has been developed for mapping and handling of radial velocity and 2D surface

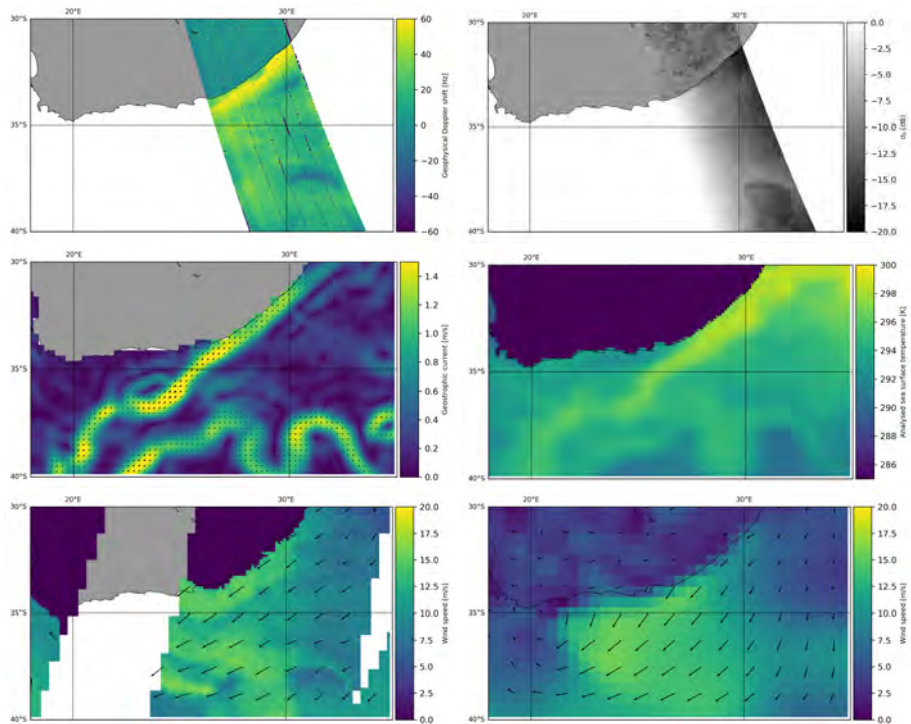


Figure 3: Envisat ASAR geophysical range Doppler shift (Hz; color) and SAR normalized radar cross section (NRCS) on 13 January 2010, collocated in (near) time and space with geostrophic current from the GlobCurrent project, sea surface temperature from the GHRSSST Level 4 OSTIA Global Foundation Sea Surface Temperature Analysis, NCEP wind forecast, and ASCAT wind. Note the clear current signature in the ASAR and ASCAT retrievals.

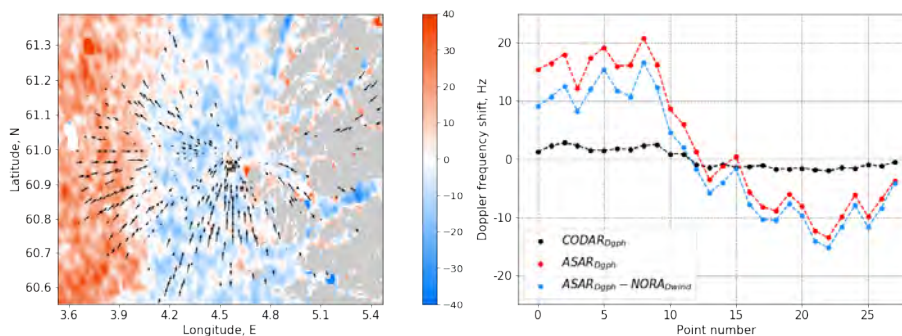


Figure 4: Envisat ASAR geophysical range Doppler shift (Hz; color; gray is land) collocated with radial velocities from the CODAR SeaSonde at Fedje (arrows) on 6 January 2010 at 10:00 UTC (left), and a comparison of the range Doppler shift before and after removal of the sea-state contribution with HF-radar radial velocities (only the measurements parallel to the SAR range direction is used in the analysis).

current products routinely provided by HF-radar systems to enable collocation with SAR data. The current version of the ingestor supports the CODAR SeaSonde HF-radar operated at the Norwegian west coast from 2002 to 2010, as demonstrated in Fig. 4. Radial velocities from the HF-radar are, here, collocated with geophysical range Doppler retrievals from Envisat ASAR. The established framework allows extension to support management of data from other HF-radar systems such as, e.g., the IOOS HF-radars system, USA.

### 3.3.4 Surface Lagrangian drifters

The Global Drifter Program (GDP) is managed by the National Oceanic and Atmospheric Administration (NOAA) with the objectives of maintaining an array of satellite-tracked surface drifting buoys to measure currents, sea surface temperature, atmospheric pressure, winds and salinity, and to enable scientific use of the data [27]. It was formerly known as the Surface Velocity Program (SVP). The drifters consist of a surface buoy and a subsurface drogue (sea anchor), attached by a long, thin tether centered at 15 meters depth. The GDP current measurements are highly relevant for comparison and evaluation of SAR range Doppler shift retrievals.

A Geo-SPaaS ingestor for surface drifters has been developed to allow easy collocation and comparison to the SAR retrievals, as illustrated in Fig. 5. The surface drifter datasets must be downloaded from <ftp://ftp.aoml.noaa.gov/pub/phod/buoydata> before ingestion. The downloaded files contain buoy measurements and metadata about each drifting buoy. Buoy datasets in Geo-SPaaS are defined for each separate drifter on 5 days intervals to be consistent with the timescales of mesoscale variability.

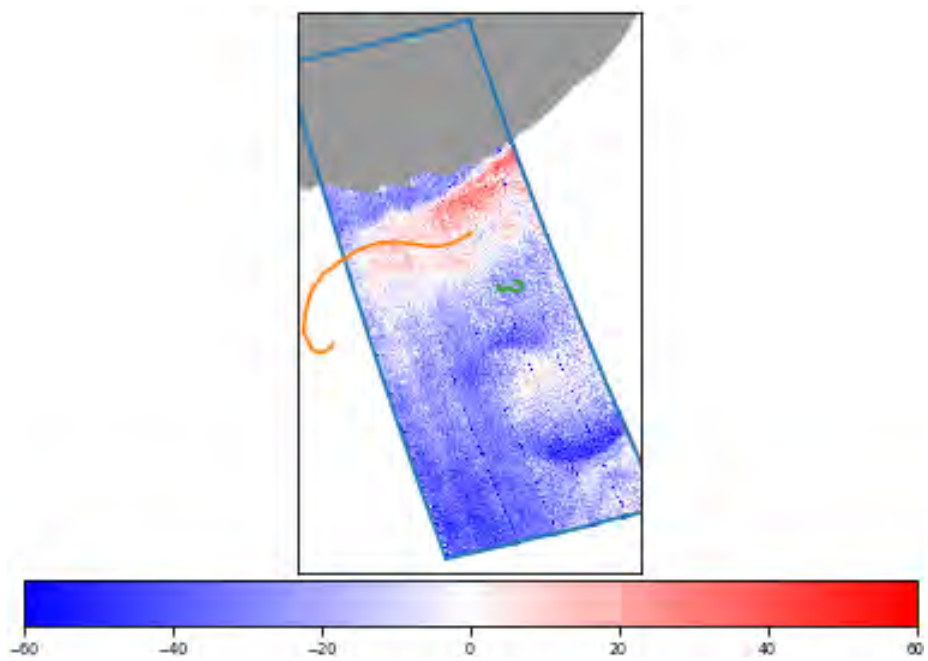


Figure 5: A surface drifter (orange line) captured in the Agulhas current and a surface drifter in calmer waters (green), collocated with a SAR acquisition on 19 January 2010 at 20:55 UTC. The time coverage of both drifters is 5 days and the total geophysical range Doppler shift is shown in Hz.

### 3.3.5 NOAA wind buoys

The NOAA National Data Buoy Center (NDBC) shares their meteorological and oceanographic data via their Distributed Oceanographic Data Systems (DODS) using the Thematic Real-time Environmental Distributed Data Services (THREDDS), which supports the Open Source Project for a Network Data Access Protocol (OPeNDAP). In short, the OPeNDAP access to data allows Geo-SPaaS to index the DODS database without having to download actual data. When NDBC buoys are collocated with, e.g., SAR imagery, the time-limited data from each buoy can be streamed from DODS, allowing very efficient data analysis without requiring extra local disk space.

The Geo-SPaaS NOAA NDBC ingestor is used to evaluate high resolution SAR wind retrievals. As an example, Fig. 6 shows an NDBC buoy (ID sjsn4) covered by a SAR acquisition. In total, we have found 13 overlapping SAR acquisitions for this buoy in January and February 2010.

## 4 SAR Doppler centroid terms and geophysical requirements

The estimated Doppler centroid shift consists in general of several terms:

$$f_{dc} = f_g + f_{geo} + f_{elec} + \Delta f_g, \quad (5)$$

where  $f_g$  is the geophysical term,  $f_{geo}$  is the geometric term,  $f_{elec}$  is the antenna electronic mis-pointing, and  $\Delta f_g$  is the residual error. The calibration of  $f_{dc}$  consists in estimating and subtracting the geometric and electronic terms on the right hand side of (5) from  $f_{dc}$ , such that only the geophysical term,  $f_g$ , and a residual error,  $\Delta f_g$ , are left.

### 4.1 Geophysical term

The geophysical Doppler shift is expressed as  $f_g = -k_R v / \pi$ , where  $k_R$  is the radar wavenumber, and  $v$  is the line-of-sight velocity of the target (defined positive if directed away from the radar). Following a two-scale decomposition, the sea surface consists of an ensemble of small-scale scattering facets (with local NRCS;  $\sigma_0$ ) which cover a large scale surface formed by superposition of longer surface waves. These scattering facets experience vertical and horizontal movements due to the longer surface waves, resulting in a spatially variable  $\sigma_0$  over the large-scale surface. In this case, the average Doppler shift reads ([9, 28]):

$$f_g = -\frac{k_R}{\pi} \frac{\overline{(u \sin \theta - w \cos \theta) \sigma_0(\theta + \Delta\theta)}}{\overline{\sigma_0(\theta + \Delta\theta)}}, \quad (6)$$

where  $u$  and  $w$  are the horizontal and vertical velocities of the scattering facets in the radar incidence plane, and  $\Delta\theta$  is the local modification of the incidence angle  $\theta$  due to waves. The geometry in Eq. 6 is illustrated in Fig. 6 of [9]. As noticed, the geophysical Doppler shift depends on the ocean wave-state and

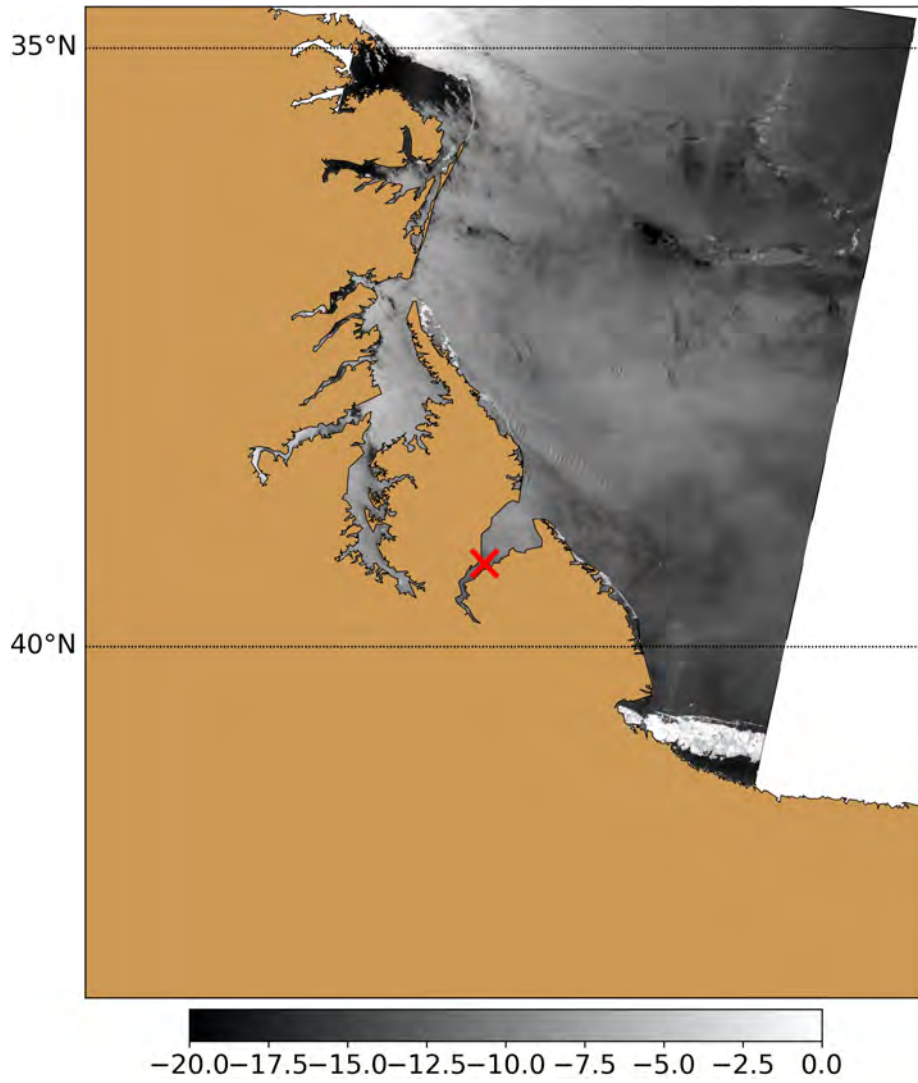


Figure 6: NDBC buoy sjsn4 collocated with a SAR acquisition on 23 February 2010 at 02:50 UTC. The NRCS is shown in dB.

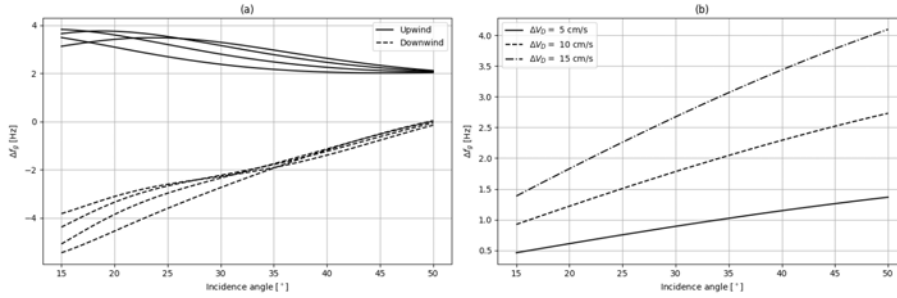


Figure 7: The required Doppler shift accuracy as function of incidence angle, translated from geophysical acceptance levels of (a) wind speed ( $\Delta u_{10} \in \pm \{6 - 4, 8 - 6, 10 - 8, 12 - 10\} \text{ m s}^{-1}$ ), and (b) horizontal surface velocity ( $\Delta V_{Dh} \in \{5, 10, 15\} \text{ cm s}^{-1}$ ).

the surface current. In the absence of current, the geophysical Doppler shift is mostly related to the local wind speed and direction (e.g., [9, 15]). As such, [15] proposed an empirical model relating the wind-dependent Doppler shift at C-band to wind speed and direction,  $f_w = C_{DOP}(\phi, u_{10}, \theta, pp)$ , where  $\phi$  is the wind direction,  $u_{10}$  is the wind speed at 10 m height,  $\theta$  is the radar wave incidence angle, and  $pp$  is the polarization state, HH or VV.

Rough estimates of the required accuracy of the retrieved geophysical Doppler shift,  $f_g$ , may be obtained via its relation to retrieval requirements for wind ( $\Delta u_{10}$ ) and current ( $\Delta V_{Dh}$ ), i.e.,  $\Delta f_g(\Delta u_{10}, \phi, \theta) \approx C_{DOP}(\phi, \Delta u_{10}, \theta)$  and  $\Delta f_g(\Delta V_{Dh}) = \frac{k_R \Delta V_{Dh} \sin \theta}{\pi}$ , where  $\Delta V_{Dh}$  is the uncertainty of the horizontally projected range Doppler velocity. An accuracy,  $\Delta u_{10} \leq 2 \text{ m s}^{-1}$  should be expected for useful wind retrieval used in scientific or operational applications, whereas users request a current retrieval accuracy of 5-10  $\text{cm s}^{-1}$ , as summarized in [18].

Figure 7 shows  $\Delta f_g(\theta)$  for different values of  $\phi$ ,  $\Delta u_{10}$  ( $u_{10} \in \{6, 8, 10, 12\}$ , and  $\Delta f_g \approx C_{DOP}(\phi, u_{10}, \theta) - C_{DOP}(\phi, u_{10} - 2, \theta)$ ), and  $\Delta V_{Dh}$ . For incidence angles  $\theta \in [25^\circ, 40^\circ]$ ,  $\Delta f_g$  should be 1.5 Hz or less in order to measure  $V_{Dh} = 10 \text{ cm/s}$ <sup>1</sup>. This should also be sufficient to retrieve the wind speed at 2 m/s uncertainty. Note that the information contained in  $f_g$  is useful to determine wind directions, even at lower accuracies,  $\Delta f_g$  (Fig. 7a).

## 4.2 Geometric term

The geometric Doppler shift results from the relative velocity between the antenna phase center and the ground target at beam center. The sensitivity to orbit and attitude variations is illustrated in Figure 8. As illustrated in Figure 8b, a pointing accuracy of about 0.35  $\text{m}^\circ$  in pitch and 0.75  $\text{m}^\circ$  in yaw is required to keep the accuracy of the Doppler shift within 1.5 Hz. According to personal communication with Berthyl Duesmann at ESA/ESTEC, it is only

<sup>1</sup>For simplicity, we here only consider the total velocity  $V_{Dh}$ , related to the combined signal from wind, waves, and current. Further uncertainty is added when splitting the signals into the given components.



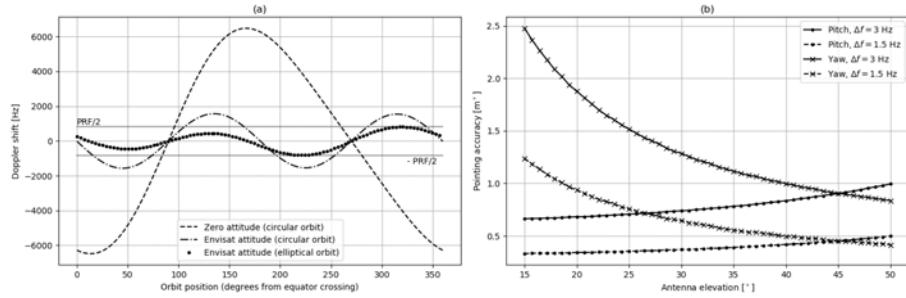


Figure 8: (a) Orbital variations of the Doppler shift at  $20^\circ$  elevation angle given circular orbits with and without attitude steering, and Envisat ASAR. (b) Required pointing accuracies in yaw and pitch, given 3 and 1.5 Hz acceptance levels for the geophysical Doppler shift accuracy,  $\Delta f$ .

possible to accomplish this level of pointing accuracy with orbit and attitude control systems that are presently only used in cosmology applications.

#### 4.2.1 Satellite attitude

Envisat ASAR monthly reports available from ESA summarizes the instrument and product quality status as derived from data acquired during the given month (see, e.g., [29]). As seen from Doppler centroid evolution plots in these reports, the impact of platform orbit and attitude instabilities is significant (within  $\pm 100$  Hz, assuming a nominal satellite orbit). In order to get a more accurate geophysical Doppler shift estimate, these biases can be reduced by employing information available in Envisat restituted attitude files (AUX\_FRA\_AX) and precise orbital state vectors from the Doppler Orbitography and Radio-positioning Integrated by Satellite (DORIS) products, and by using DC estimates over land to correct for residual errors.

The geometric Doppler shift is calculated according to the approach described in [24]. The attitude steering for any position in the orbit is defined by the Envisat yaw steering law with rotation amplitudes,  $C_X$ ,  $C_Y$ ,  $C_Z$  (from restituted attitude files), and the satellite hour angle,  $\gamma_h$  (computed from orbital state vectors):

$$\begin{aligned}
 \gamma &= C_Y \sin \gamma_h \\
 \psi &= C_X \sin(2\gamma_h) \\
 \phi &= C_Z \cos \gamma_h \left( 1 - \frac{(C_Z \cos \gamma_h)^2}{3} \right)
 \end{aligned} \tag{7}$$

where  $\gamma$ ,  $\psi$ , and  $\phi$ , are the roll, pitch, and yaw angles of the satellite. Figure 9a shows the distribution of global DCA measurements over land in HH polarization. Most noticeable, is a gradient along the look elevation angle caused by erroneous yaw angles used in the calculation of the geometric Doppler shift, most likely connected to the displacement of the antenna phase center from the

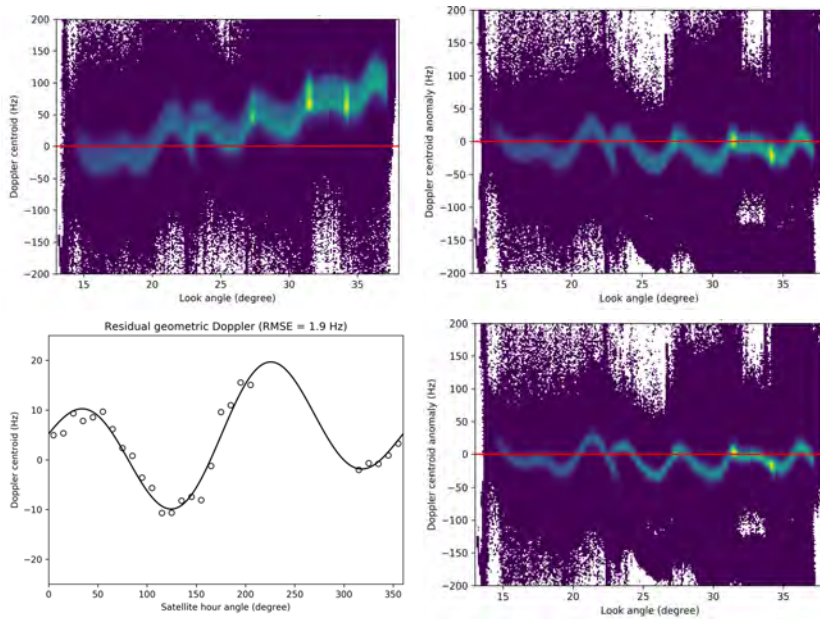


Figure 9: Distributions of global Doppler centroid anomaly (DCA; HH polarization) measurements over land (a) before geometric correction, and (b) after attitude correction. Panel (c) shows the DCA drift along one orbital period, and panel (d) shows the DCA distribution after also correcting for the orbital drift.

satellite's center of mass. The linear trend and mean offset of the DCA profile can be corrected by finding appropriate corrections to the attitude angles. Thus, Fig. 9b is obtained by setting the corrections  $\Delta\gamma = 0.025^\circ$  [30],  $\Delta\psi = 0.026^\circ$ , and  $\Delta\phi = 0.209^\circ$  (manual fit). The pitch and yaw corrections are similar to previous reported numbers, e.g., [31].

However, the histograms in Fig. 9 (a) and (b) both display several maxima for each look elevation angle bin. Fig. 9c shows the mean DCA in  $10^\circ$  bins of the satellite hour angle and the best fit curve. As noticed, there is also a residual Doppler shift that varies with the satellite hour angle (its osculating true latitude). The best fit curve was estimated by adopting a model function combining slightly modified forms of the yaw steering law (7), i.e.:

$$\begin{aligned}\gamma &= a \sin(\gamma_h + b) - c \\ \psi &= d \sin(2\gamma_h + e) + f,\end{aligned}\tag{8}$$

giving  $a = -6.2$ ,  $b = 0.15$ ,  $c = -90.5$ ,  $d = 10.2$ ,  $e = 0.15$ , and  $f = 90.9$ . The resulting DCA distribution is shown in Fig. 9d. Clearly, the variance is reduced, although errors are still evident.

#### 4.2.2 Surface topography

In addition to the satellite orbit and attitude, the terrain height must also be known for precise estimation of  $f_g$ . The terrain height affects the Doppler shift

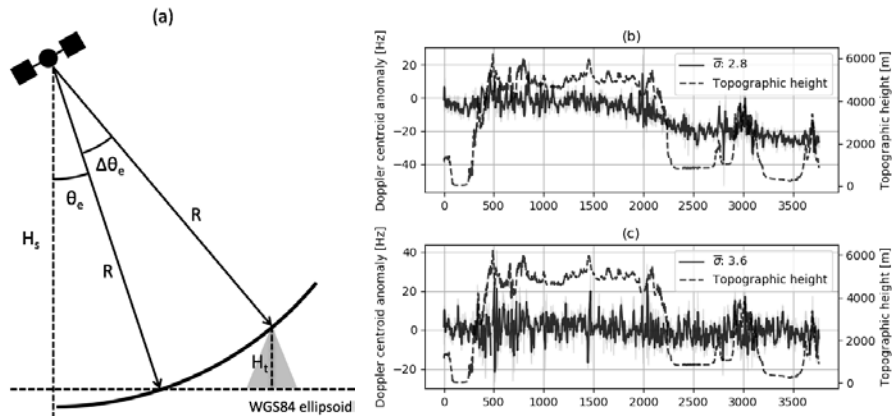


Figure 10: Terrain height effects on the Doppler centroid anomaly (DCA); (a) target positions on the WGS84 ellipsoid and an elevated surface for a given target range, (b) uncorrected DCA for an ASAR acquisition over the Himalaya mountains on 7th January 2010, and (c) corrected DCA for the same acquisition. The mean standard deviation,  $\bar{\sigma}$ , within a box average low pass filter smoothing window of 11 km is indicated in the legends of (c) and (d), respectively. The standard deviations around the mean DCA are 10.1 and 5.5 Hz in (b) and (c), respectively.

as illustrated in Figure 10a. At a given slant range,  $R$ , the target position is ambiguous without exact knowledge of the target height. In this case, the target position on the Earth ellipsoid (WGS84) is not the same as the real target position on an elevated surface for a given slant range distance. The look angle differs with  $\Delta\theta$  between the two reference systems. This causes a slightly different Doppler shift between, e.g., mountain and sea areas. Quantitatively, a height difference of 1 km at  $25^\circ$  incidence angle induces 2.7 Hz geometric Doppler shift and a look angle shift of  $0.13^\circ$  compared to the WGS84 reference. Since land reference is used for calibrating the Doppler shift, a correction of the nominal WGS84 referenced look angle and Doppler shift, in slant range geometry, is therefore required (see, e.g., [32]). The DCA before and after correction for terrain height is shown as function of azimuth in Figure 10 b and c, respectively. The main remaining error is caused by electronic mis-pointing.

### 4.3 Electronic term

#### 4.3.1 Antenna gain variations

We have discovered an unexpected DC error source coming from a small alternating bias in the raw data intensity ( $< 0.1dB$ ) between successive calibration pulse periods (1024 lines in SM data) [16]. These gain variations in the raw data cause an azimuthal scalloping of the Doppler with a period of  $1024/PRF$  and with an amplitude of around 2 hertz. In Fig. 11a is shown the intensity offset between successive calibration pulses periods in ASAR SM data. The

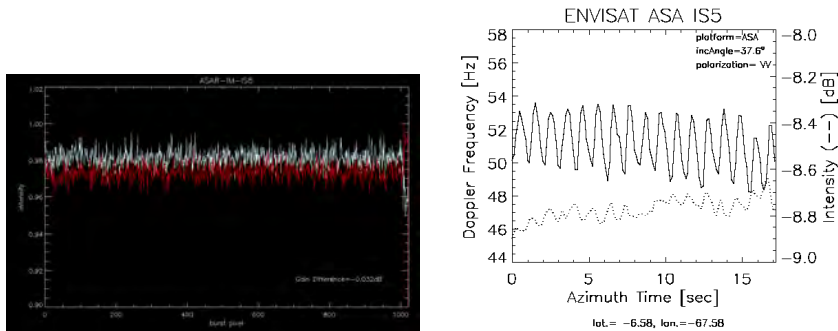


Figure 11: Left: Rawdata intensity average over many successive calibration pulse periods. Right: Average azimuth DC profile and corresponding intensity profile from ASAR S5 data acquired over rain forest.

corresponding DC azimuth scalloping is shown in Fig. 11b. Note that the scalloping is also observable in the mean intensity profile along azimuth as shown in Fig. 11b. The same type of Dc scalloping is observed in the AP and ScanSAR modes but the period is different. However, the raw data gain variations can be estimated and compensated for as part of the Doppler estimation. This has been done in the latest version of the ASAR ScanSAR Doppler processor with good results.

#### 4.3.2 Gain differences between antenna elements

Malfunctioning and/or temporal gain changes of individual antenna elements cause mis-pointing of the antenna beam around the theoretical zero Doppler shift. This is a slow-varying function of time that can be corrected with land reference following the geometric correction. The mis-pointing correction is accomplished by organizing the median DCA values in look angle bins of, e.g.,  $0.05^\circ$  in look-up tables (LUTs) covering a selected time period based on antenna stability information provided in the Envisat ASAR monthly reports (e.g., [29]). Fig. 12 represents the antenna mis-pointing in sub-swaths 1 and 2 for the HH and VV polarization channels in January 2010. The accuracy of the antenna mis-pointing correction is then represented the ability to smooth the data in the range direction. A last correction of the mean offset from zero over land is necessary to fully calibrate the data.

#### 4.4 Residual error

The residual error (RMSE) in each subswath is, here, defined as the root-mean-square difference from zero over land in acquisitions covering the Amazon. At the highest resolution, the RMSEs are 7.6, 5.4, 8.6, 5.5, and 6.9 Hz in subswaths 1-5, respectively (see Figure 13). The larger RMSEs of subswaths 1, 3, and 5 are caused by aliasing due to the low azimuth sampling rate (about 1700 Hz) in those subswaths, compared to subswaths 2 and 4 (about 2100 Hz). Reduced resolution improves the RMSEs as demonstrated in Figure 13. Previous estimates of the

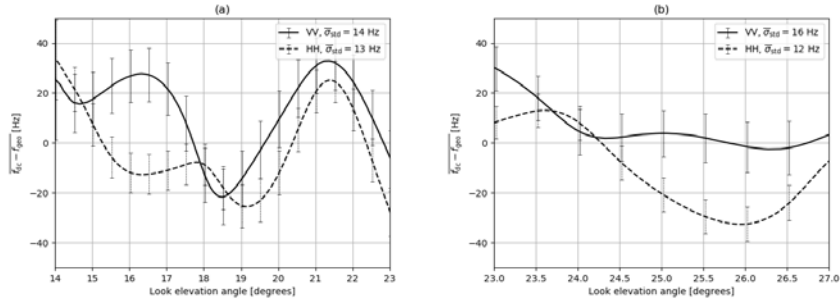


Figure 12: Estimated Doppler shift resulting from antenna electronic mis-pointing in sub-swaths 1 (a) and 2 (b) in January 2010. The error-bars show the standard deviations,  $\sigma_{\text{std}}$ , in each look elevation angle bin (of  $0.05^\circ$ ), and the legends provide the mean standard deviations,  $\bar{\sigma}_{\text{std}}$ .

RMSE over the Amazon by [21] using the Doppler centroid grid (pixel spacing of 9km in near range and 3.5 km in far range) provided in the ASAR level-1 wide swath mode products since 2007 are 2.5 and 2.6 Hz in HH and VV polarization, respectively. The present results are comparable at the same spatial scales, both with our new method and the simple correction using land reference in each scene (*method (i)* in [21]). Note, however, that the new method presented here is a global approach that should give the same uncertainties in other areas containing less uniform land reference. This is a significant improvement from previous results.

## 5 Results and validation

The geophysical Doppler shift obtained from the reprocessed (VV polarized) acquisitions in January 2010 are compared to old results obtained from the methods described in [21] in Figs. 14 and 15. Most noticeable is the improvement of resolution, which allows measurements also inside fjords (Fig. 14a) and likely observations of ships (Fig. 15). Apart from this, the new and old results compare well.

The geophysical Doppler shift contains contributions from both wind, waves, and current. Fig. 16 shows two acquisitions over the Gulf Stream region. The current is here strong enough to clearly show up in the range directed geophysical Doppler shift, which is here compared to surface geostrophic current (overlaid arrows) retrieved from GlobCurrent [18]. Clearly, both the main core of the Gulf Stream and several eddies are evident in the Doppler shift data. Due to signal contributions from wind-waves, also a wind front is clearly evident in Fig. 16(a). The minimum Doppler shift in the eddy that is seen in Fig. 16(b) is biased toward zero due to wind blowing against the current direction. Further work, incorporating methods to separate signals from wind-waves and current, e.g., employing CDOP [15] combined with radar imaging forward models, is needed to improve both SAR wind and surface current retrieval algorithms. The present work is fundamental to this effort, and will be employed in a full

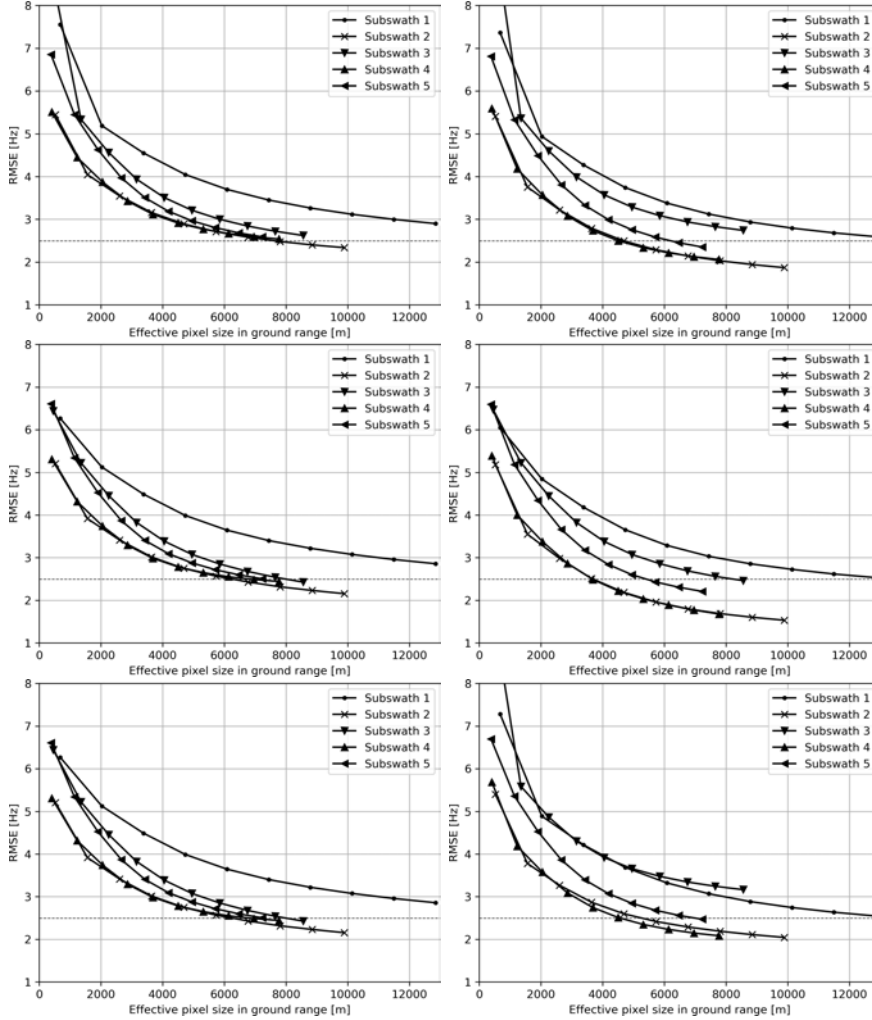


Figure 13: Residual errors (RMSE) at various resolutions for each subswath estimated from Doppler centroid anomaly retrievals over the Amazon. Left column shows the RMSE after corrections following the procedure presented in section 4, and right column shows the RMSE after a simple correction using land reference in each individual scene. The first row shows results without removal of outliers or topographic height restrictions, whereas the second row displays the results after removal of outliers (defined as pixels deviating from the mean by more than three times the standard deviation), and the third row displays the results after outlier removal and only using pixels below 200 m height. The latter is in line with the RMSE examination method presented in [21], of which the best estimate for HH polarization was 2.5 Hz as indicated by the horizontal dashed line in each plot. The numbers provided in the legend parentheses are the number of pixels in range direction at highest resolution.

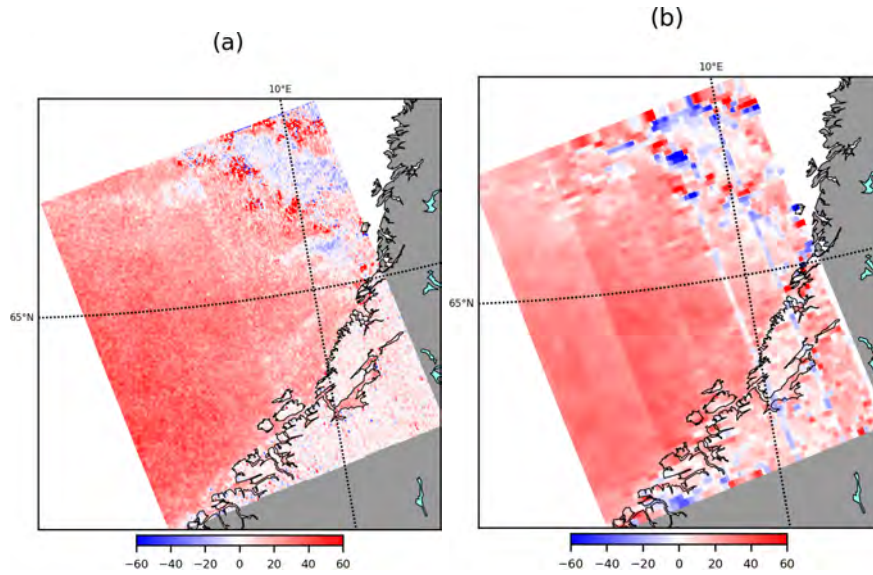


Figure 14: New (left) versus old (right) geophysical Doppler shift product. Processing from the SLC product allows resolution down to 1 km grid cells, as opposed to a previous grid of 4-9 km by 8 km (range, azimuth).

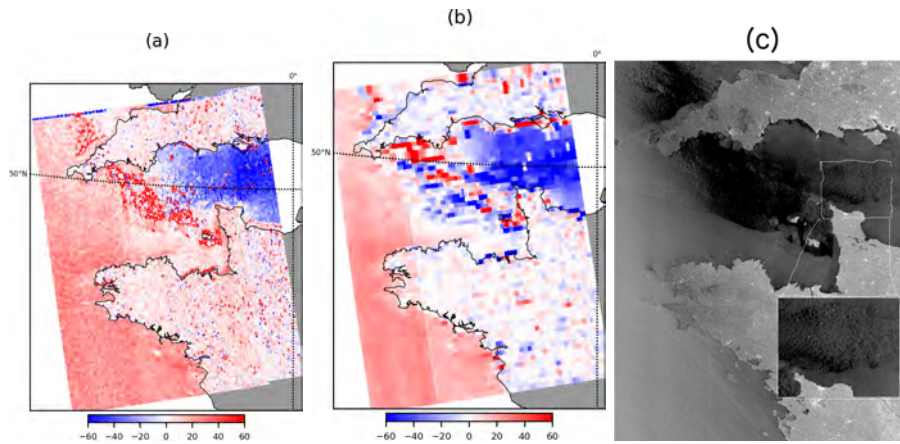


Figure 15: Geophysical Doppler shift on 2010-01-02 over the English Channel - (a) new and (b) old data. The normalised radar cross-section (NRCS) is shown in panel (c) at -20 to 0 dB. Notice the wind front and calm sea area causing noise in the middle of the Doppler shift images and the likely appearance of ships in the English channel (all panels).



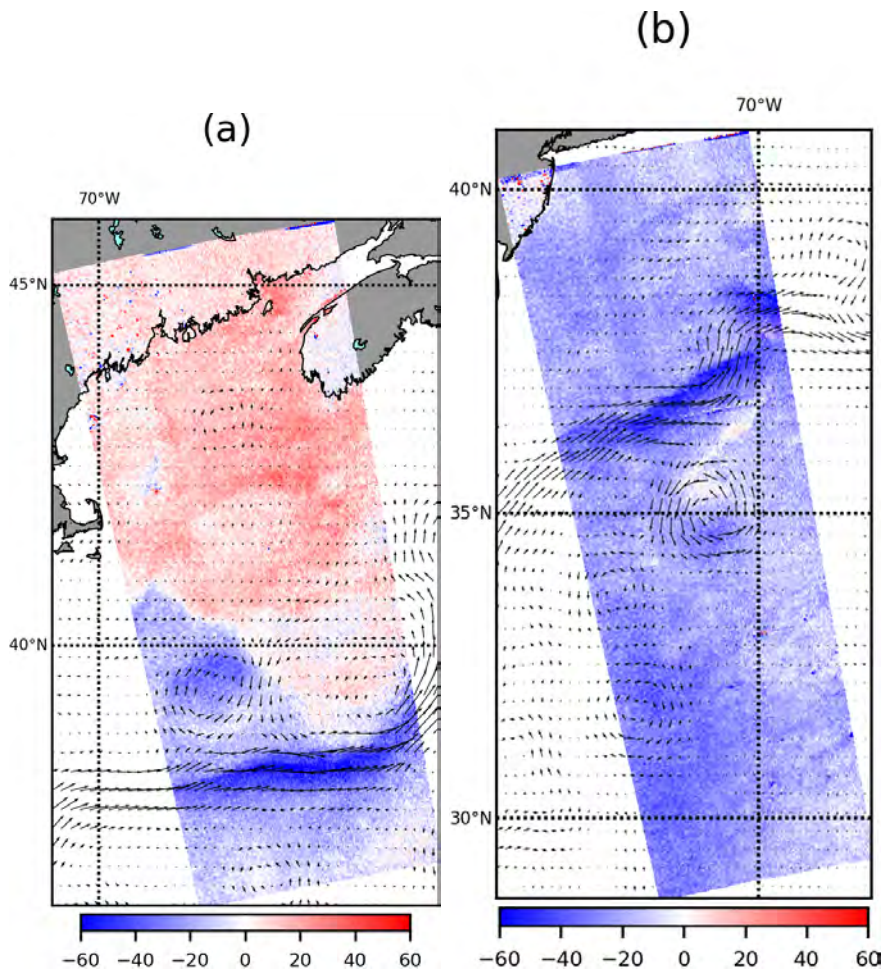


Figure 16: Geophysical Doppler shift (combined wind, waves, and current signal; 2010-01-01 [left] and 2010-01-13 [right]) over the Gulf Stream region overlaid geostrophic sea surface current from the ESA GlobCurrent project.

reprocessing of the Envisat ASAR ScanSAR wide archive with data available from 2002 to 2012.

## 5.1 Bayesian wind retrieval

Figure 17 shows wind signatures in SAR NRCS and geophysical Doppler shift, and the associated NCEP model forecast on 23 February 2010 at 02:50 UTC. Both CMOD and the Bayesian approach with and without the geophysical range Doppler shift has been used to estimate the wind field from combination of SAR and model data. The NDBC buoy sjsn4 is marked by a red cross and has been collocated with 12 other SAR acquisitions.

The comparison of the SAR wind retrievals from 13 acquisitions with the NDBC buoy is shown in Fig. 18. The root mean square deviation (RMSD) between



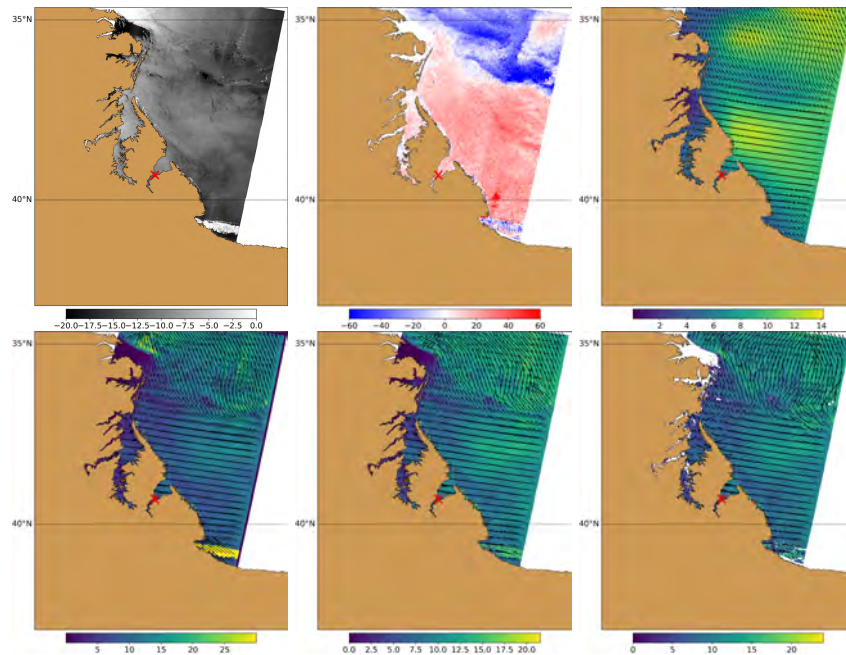


Figure 17: Wind signatures in SAR NRCS (left) and geophysical Doppler shift (center), and the associated NCEP model forecast (right; top panels) on 23 February 2010 at 02:50 UTC. The lower panels show the CMOD wind speed with model directions (left), and the wind fields estimated with Bayesian inversion of the NRCS and NCEP (center), and NRCS, Doppler and NCEP (right) datasets, respectively. The location of meteorological measurements from a National Oceanic and Atmospheric Administration (NOAA) National Data Buoy Center (NDBC) weather buoy is marked by a red cross in all the images.

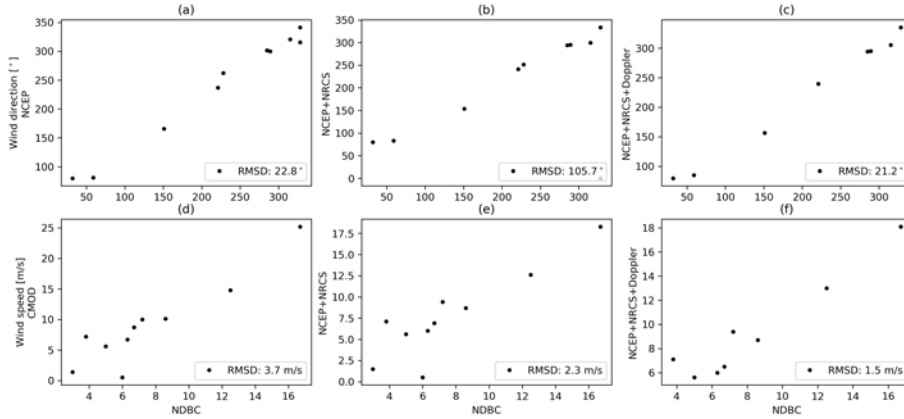


Figure 18: Comparison of SAR and NDBC wind retrievals. Panels (a)-(c) show the wind directions from NCEP, Bayesian minimization of NCEP and SAR NRCS, and Bayesian minimization of NCEP, SAR NRCS, and SAR Doppler, respectively. Panels (d)-(f) show the wind speed from CMOD (d) and Bayesian minimization as for panels (b) and (c).

the NCEP model and buoy wind directions is  $23^\circ$ . The Bayesian minimization using model and NRCS results in a much higher RMSD of  $106^\circ$ , whereas the Doppler shift helps to reduce the RMSD to  $21^\circ$ . The RMSDs between SAR and buoy wind speed retrievals decreases gradually from 3.7 m/s with the CMOD method to 2.3 m/s and 1.5 m/s, with and without Doppler, in the Bayesian approach.

Given the buoy's close proximity to land, these results are promising. However, our SAR dataset is very limited, and further investigations are needed to better evaluate the method and the new geophysical Doppler shift retrieval scheme.

## 5.2 Sea ice drift

The improvement of ice drift retrieval has been demonstrated in the ESA funded Prodex DESICE project also led by NERSC. The final report from that project is attached in Appendix A. To summarize, sea ice drift in the Fram Strait was derived in Prodex DESICE using both NRCS pattern matching and Doppler shift from 22 SAR scenes in January 2010. The correlation between instantaneous range-directed drift velocity derived from the individual range Doppler shifts and drift speed derived from pairs of NRCS images is quite low due to noise in the SAR Doppler shift, and the differences in the temporal scales. Inter-comparison of monthly averages in January 2010, however, showed overall high consistency of the two products (RMSE: 0.15 m/s, slope: 1.15). The difference is largest for the first sub-swath (RMSE: 0.36 m/s, slope: 0.9) and decays with incidence angle (RMSE: 0.2 m/s, slope: 0.99). Despite the low signal-to-noise ratio, low effective resolution and only one component of the drift vector, the Doppler algorithm proves to be very useful for complementing

the pattern-matching algorithm in the MIZ and ice deformation zones.

### 5.3 Sea surface current

Based on a simple geometrical consideration of SAR viewing angles in ascending and descending satellite pass it is possible to estimate mean zonal and meridional components from the following two equations for the range Doppler velocity in ascending and descending satellite pass configuration:

$$\begin{aligned} v_{ai} &= u_i \cos \alpha_i + v_i \sin \alpha_i \\ v_{dj} &= -u_j \cos \delta_j + v_j \sin \delta_j \end{aligned} \quad (9)$$

where  $v_{ai}/v_{dj}$  is the range Doppler velocity (negative/positive toward the radar in ascending/descending pass) and  $\alpha_i/\delta_j$  is the angle between the geographical east-west and the radar look axis from an acquisition in ascending/descending satellite pass configuration, and  $u_{\{i,j\}}/v_{\{i,j\}}$  is the zonal/meridional current component at the time of observation. To account for uncertainties and varying angles  $\alpha_i$  and  $\delta_j$ , data from several observations weighted by the inverse of their error variances can be summed according to

$$\begin{aligned} \sum_i \frac{v_{ai}}{\sigma_{ai}^2} &= u \sum_i \frac{\cos \alpha_i}{\sigma_{ai}^2} + v \sum_i \frac{\sin \alpha_i}{\sigma_{ai}^2} \\ \sum_j \frac{v_{dj}}{\sigma_{dj}^2} &= -u \sum_j \frac{\cos \delta_j}{\sigma_{dj}^2} + v \sum_j \frac{\sin \delta_j}{\sigma_{dj}^2}, \end{aligned} \quad (10)$$

where  $v_{ai}/v_{dj}$  is the range Doppler velocity with uncertainty  $\sigma_{ai}/\sigma_{dj}$  retrieved from a given acquisition ( $i/j$ ) in ascending/descending satellite pass. Mean zonal ( $u$ ) and meridional ( $v$ ) velocity components, as well as uncertainties, can then be expressed as

$$\begin{aligned} u &= \frac{V_a s_d - V_d s_a}{s_a c_d + s_d c_a} \\ v &= \frac{V_a c_d + V_d c_a}{s_a c_d + s_d c_a} \\ \sigma_u &= \frac{1}{s_a c_d + s_d c_a} \sqrt{s_d^2 \sum_i \frac{1}{\sigma_{ai}^2} + s_a^2 \sum_j \frac{1}{\sigma_{dj}^2}} \\ \sigma_v &= \frac{1}{s_a c_d + s_d c_a} \sqrt{c_d^2 \sum_i \frac{1}{\sigma_{ai}^2} + c_a^2 \sum_j \frac{1}{\sigma_{dj}^2}} \end{aligned} \quad (11)$$

where  $V_a = \sum_i v_{ai}/\sigma_{ai}^2$ ,  $c_a = \sum_i \cos \alpha_i/\sigma_{ai}^2$ ,  $s_a = \sum_i \sin \alpha_i/\sigma_{ai}^2$ ,  $V_d = \sum_j v_{dj}/\sigma_{dj}^2$ ,  $c_d = \sum_j \cos \delta_j/\sigma_{dj}^2$ , and  $s_d = \sum_j \sin \delta_j/\sigma_{dj}^2$ .

The reconstructed orthogonal mean surface velocity components in the Agulhas Current and the Gulf Stream, including uncertainties, are shown in Figures 19 and 20 for the period from 1 January 2010 to 31 March 2010. The uncertainties in the zonal component ( $u$ ) are about 10-15 cm/s in the best covered areas. Since both the ascending and descending look directions are near parallel to the zonal direction, the meridional velocity component ( $v$ ) is much more noisy than

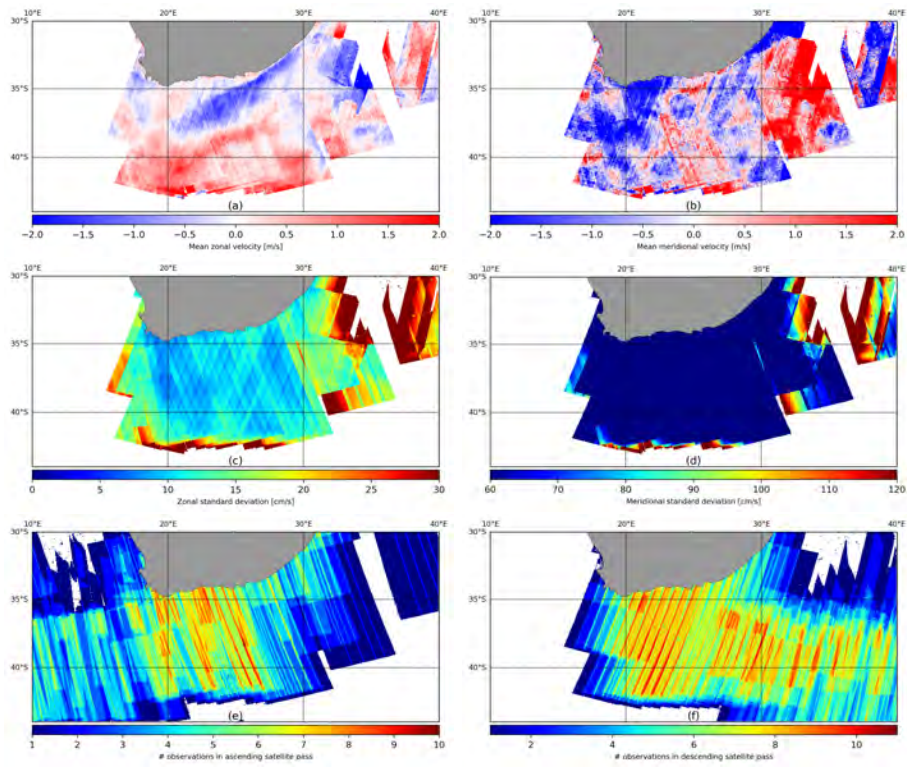


Figure 19: Zonal (a) and meridional (b) surface velocity components and their respective uncertainties (c,d) in the Agulhas Current retrieved from Envisat ASAR range Doppler velocity measurements. The lower panels show the number of observations in ascending (e) and descending (f) passes.

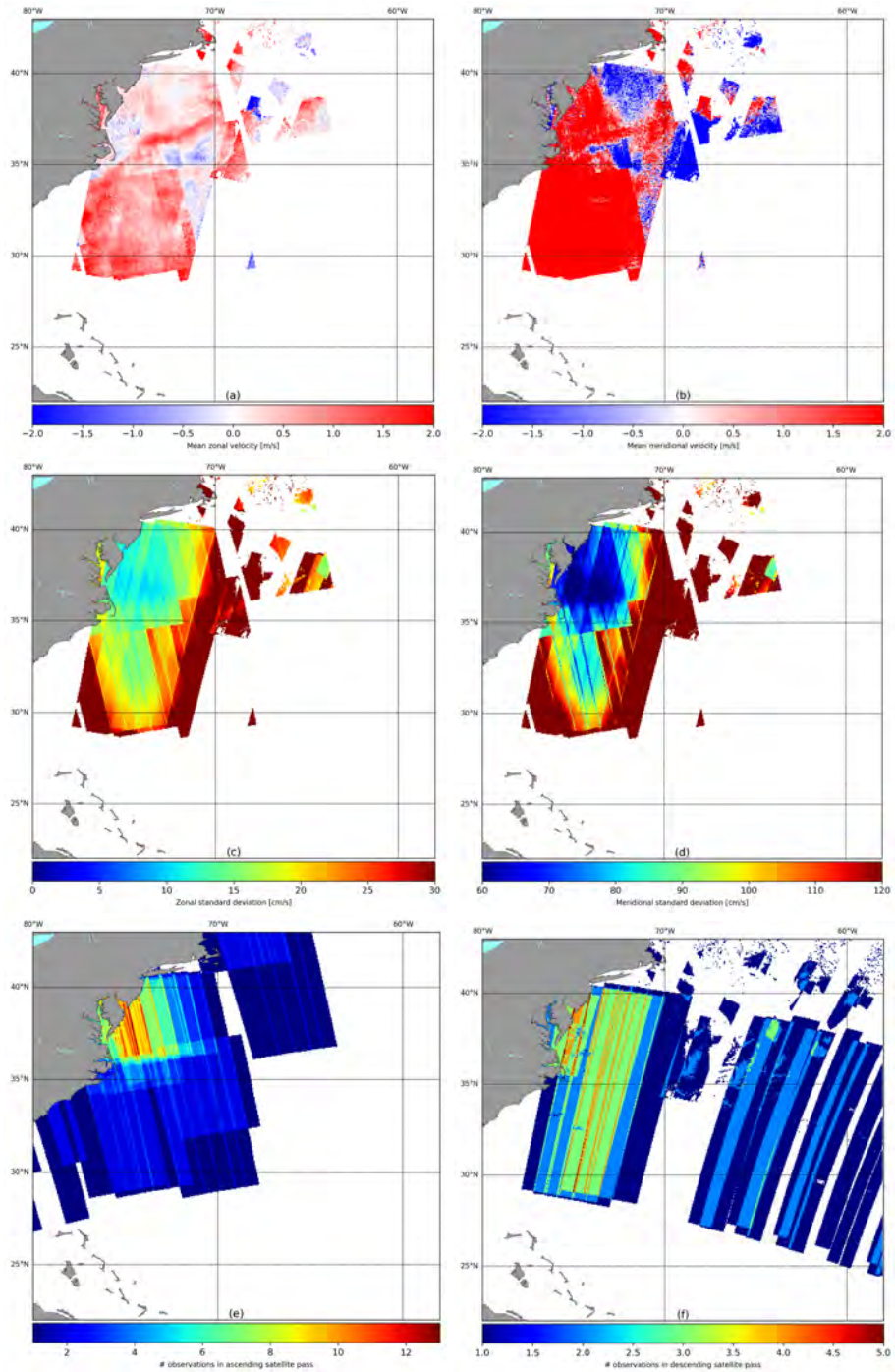


Figure 20: Zonal (a) and meridional (b) surface velocity components and their respective uncertainties (c,d) in the Gulf Stream retrieved from Envisat ASAR range Doppler velocity measurements. The lower panels show the number of observations in ascending (e) and descending (f) passes.

the zonal component, and it has much higher uncertainty ( $\sigma_v > 30$  cm/s in the Agulhas Current, and  $\sigma_v > 60$  cm/s in the Gulf Stream).

More data over a longer time span is needed to obtain higher certainty in both components. The present data amount in the Nordic Seas is too small to reveal any evidence of the upper ocean circulation in that region. This should, however, be possible to estimate over longer time spans following full reprocessing of the Envisat ASAR wide swath mode data archive.

#### 5.4 Initial investigations on wave-bias retrieval from WV mode

The Doppler centroid (DC) processor can also process radial velocity field from ASAR WV mode data on single-look complex (SLC) format. It is basically the same processor as used for ASAR SM and Sentinel WV mode. However, the ASAR WV mode processor also includes a cross spectra estimation and wave and wind inversion module. The output product from the ASAR WV mode processor is the same format (netCDF) as the Sentinel WV mode OCN product. Examples of DC, wave and wind fields are shown in Figure 21. In Figure 22 the cross-spectra and wave spectra from one single imagette is shown.

Recently, it was proposed to use the high-frequency part of the signed cross-spectra (i.e., wind sea driven part) to improve the calibration of the Sentinel WV mode Level 2 Doppler centroid. It turns out that the signed cross-spectra energy taken at high range wavenumbers is a good proxy for the range wind speed, and thus also for the "Wave Bias Dc" (see SeaSAR2018). The ASAR WV mode has significantly lower range bandwidth than Sentinel 1 WV mode. It is therefore of importance to check if there is a correlation between the ASAR WV mode Doppler centroid and the signed cross-spectra energy. This is assessed in Figure 23 showing strong correlation between the DC anomaly and the estimated cross-spectra energy of short waves (CSE). This opens up for using the same approach as proposed for S1 to calibrate the DC using the CSE parameter, and successively retrieve the surface current from WV mode data.

## 6 Conclusion

The main goal of this project was to generate and deliver a new high-resolution dataset of the yearly, seasonal and monthly mean ocean circulation in the Nordic Seas from 2002 to 2012. In combination with radar altimetry data and GOCE based geoid estimates, this would then be used to estimate a new high-resolution Mean Dynamic Topography (MDT) for the region.

In retrospect, these were very ambitious goals that in principle were unattainable given the size of the project. In particular, the need for software tools for proper data analysis involving many different types of observations and huge amounts of SAR data has caused delays in the project execution. To handle the processing and analysis in the most general and efficient way, the Nansat [19]

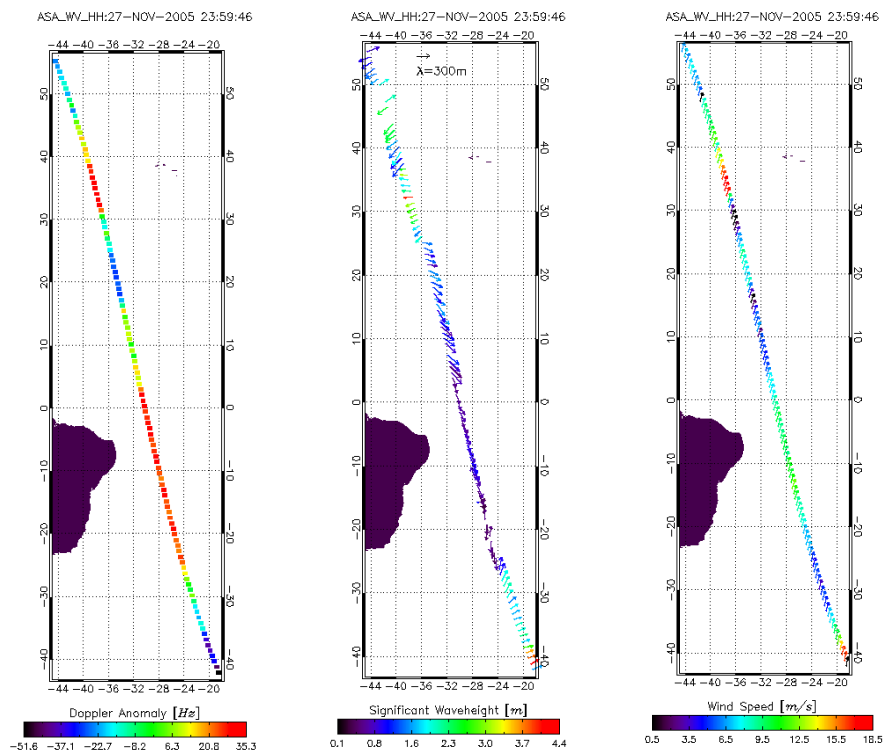


Figure 21: Left: ASAR WV mode Doppler anomaly (i.e., estimated Doppler minus geometric Doppler). Center: Dominant wavelength and direction. Left: Wind speed and direction.



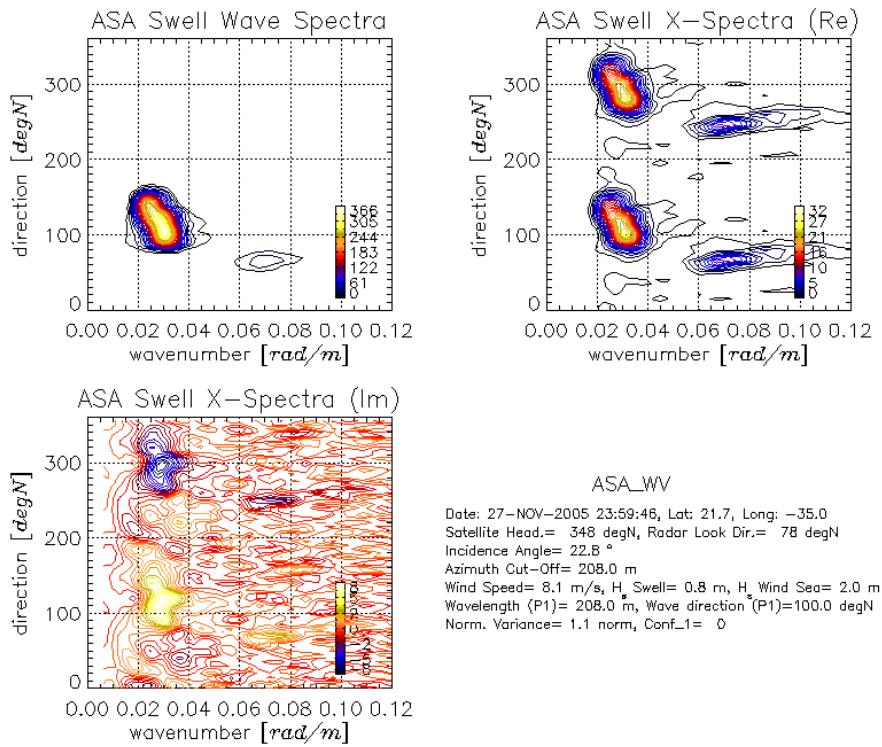


Figure 22: ASAR WV mode wave spectra and cross-spectra (real and imaginary parts) extracted from one single imagette.

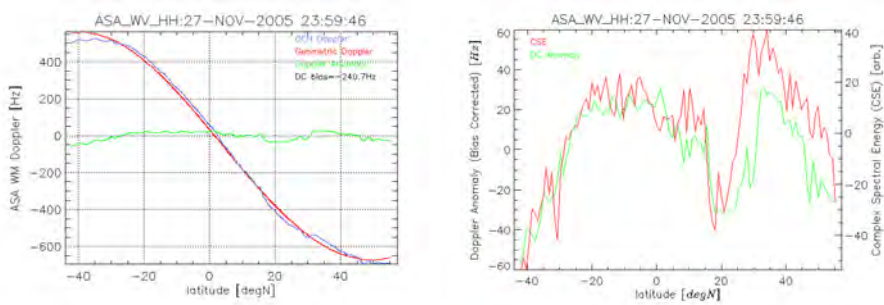


Figure 23: Left: Doppler centroid shift (blue), predicted geometric Doppler shift (red) (offset of 240 Hz removed), and Doppler centroid anomaly (green) along the satellite orbit as function of latitude. Right: Ocean wind wave cross-spectral energy parameter (CSE, red) and the Doppler anomaly (green) as function of latitude. Note that the latitude dependency in the CSE and also in the DC anomaly are very well correlated with the wind field (see Figure 21).



and Geo-SPaaS tools have been developed in collaboration with other projects. Nansat and the core of Geo-SPaaS are open-source and available from GitHub (see <https://github.com/nansencenter/nansat> and <https://github.com/nansencenter/django-geo-spaas>). Challenges related to data access and calibration forced us to focus on only a short observation period of 2-3 months in 2010 from Envisat ASAR. However, this research has resulted in a much better understanding of the various contributions to the SAR range Doppler centroid shift and its geophysical calibration.

The main challenge in estimating the geophysical range Doppler shift lies in the estimation of an accurate geometric Doppler shift and correction of antenna mis-pointing. Three main issues must thus be considered: (1) The satellite orbit and attitude must be known to high accuracy, (2) the geometric Doppler shift and the antenna pointing must be referenced to the absolute surface target position using a high-resolution Digital Elevation Model (DEM), and (3) electronic noise due to gain variations in the antenna causes mis-pointing that must be corrected by the use of land reference if it is not known.

Based on a user survey in the ESA GlobCurrent project and general wind retrieval requirements, future SAR missions should target a maximum uncertainty of 1.5 Hz in the geophysical range Doppler shift. This corresponds to an uncertainty of  $V_{Dh} = 10$  cm/s at  $25^\circ$  incidence angle. Note that  $V_{Dh}$  relates to the combined signal from wind, waves, and current, and that further uncertainty is added when splitting the signals into the given components. The uncertainty  $\Delta f_g = 1.5$  Hz corresponds to a pointing accuracy of about  $0.35$  m° in pitch and  $0.75$  m° in yaw. Some relaxation of this requirement should be possible if the orbit and attitude is sufficiently stable over time to allow the use of land reference from acquisitions before and after the ocean scene under consideration.

Thanks to the high stability of the Envisat attitude, the geophysical Doppler shift has been calibrated to about 2.5 Hz accuracy at 8 km grid using land reference data and orbit and attitude estimates from Envisat restituted orbit and attitude files. With the previous methods, e.g., published by [21], the uncertainty was comparable over the Amazon but the global RMSE was twice as high. The new method presented here is a global approach that should give the same uncertainties in other areas containing less uniform land reference. This is a significant improvement from previous results.

The examples of well calibrated data in section 5 clearly shows the combined effects of wind and surface current, and also ships in the English channel. The use of SAR range Doppler centroid shift for improved wind retrieval is demonstrated by comparison of wind field measurement using Bayesian inversion to wind measurements by a NOAA NDBC wind buoy. These results are promising, although our SAR dataset is very limited and further investigations are needed to better evaluate the method.

Despite a low signal-to-noise ratio, low effective resolution and only one component of the drift vector, the range Doppler algorithm also proves to be useful for complementing the pattern-matching algorithm for sea ice drift retrieval in the marginal ice zone (MIZ) and ice deformation zones.

The reconstructed mean zonal surface velocity components in the Agulhas Current and the Gulf Stream from 1 January 2010 to 31 March 2010 are estimated

with uncertainties about 10-15 cm/s in the best covered areas. More data over a longer time span is needed to obtain higher certainty in both the zonal and meridional current components. The present data amount in the Nordic Seas is too small to reveal any evidence of the upper ocean circulation in that region.

The signed cross-spectra energy taken at high range wavenumbers in S1 WV mode acquisitions has been shown to be a good proxy for the range wind speed, and thus also for the wave bias in the ocean geophysical range Doppler shift. Any correlation between the ASAR WV mode Doppler centroid and the signed cross-spectra energy was therefore also assessed, and revealed strong correlation between the DC anomaly and the estimated cross-spectra energy of short waves (CSE). This opens up for using the same approach as proposed for S1 to calibrate the DC using the CSE parameter, and successively to retrieve the surface current from WV mode data.

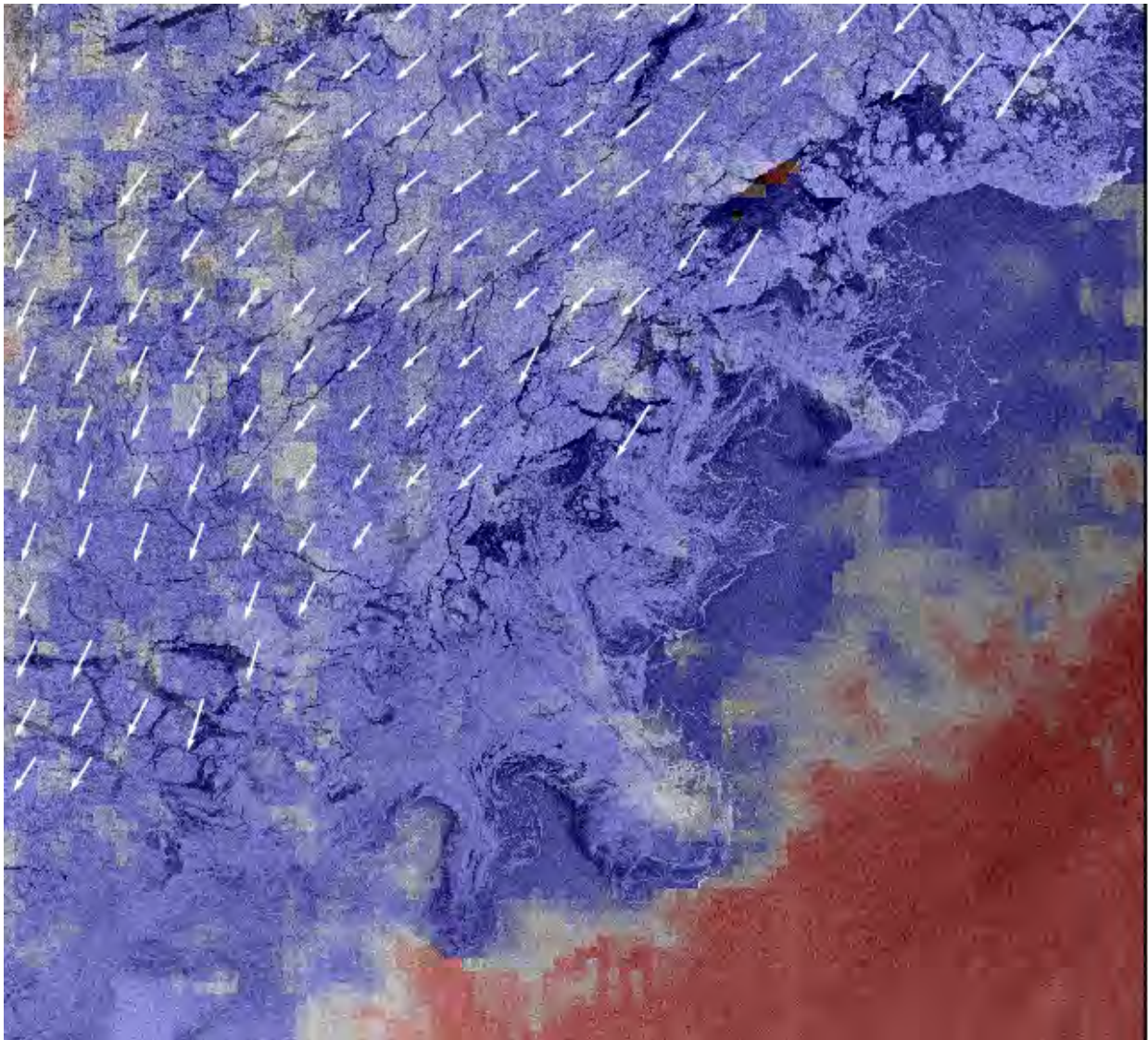
A full reprocessing of the Envisat ASAR wide swath and wave mode data archives is now being implemented at the ESA Grid Processing on Demand (G-POD) for Earth Observation Applications service. The reprocessed Doppler shift retrievals will then be used to produce new long-term timeseries of wind and sea surface current from SAR, also to allow improved Mean Dynamic Topography (MDT), and combined use of SAR and altimetry for better sea surface current monitoring, particularly in the climatically important Nordic Seas region.

Following the work done in this project, the focus should now be shifted to Sentinel-1. The ESA ground segment does not process all Sentinel-1 IW and EW acquisitions to level-2, and to obtain a consistent and long-term dataset that can be used in, e.g., studies on Arctic and high latitude climate, routine and systematic Doppler retrieval should be achieved. Also, since the ESA level-2 processing does not provide surface current but only the radial velocity field, Norut's and NERSC's Doppler processing chain should be extended to enable extraction of the geophysical Doppler shift from Sentinel-1 SAR IW and EW modes, and to quantify the contributions from wind and waves (e.g., Stokes and Ekman drift) to retrieve the underlying surface current. The processing should start with level-0 data to allow increased flexibility by the new possibility to control all processes from raw data to final product. The goal is then to have a fast and stable processing chain that can be integrated into the Norwegian ground segment. This involves a good portion of research and development, but by solving the challenges related to using the Doppler centroid shift in Sentinel-1 SAR data, there is a good opportunity to obtain information about ocean currents in the Nordic seas and the Arctic to users in near real-time.

## Appendices

### A Prodex DESICE final report

# PRODEX Arrangement – Contract No. 4000115940



**Project title:** Drift Estimation of Sea Ice in the Arctic Ocean and sub-Arctic Seas

**Short name:** DESIce

**Project duration:** 01.01.2017 to 28.02.2018

**Reporting period:** Final Report (01.01.2017-28.02.2018)

**Authors:** Jeong-Won Park, Anton Korosov, Morten W. Hansen, Johnny A. Johannessen, and Mohamed Babiker

**Contact person:**

Prof. Johnny A. Johannessen

Tel: +47-55-20-58-00

email: [johnny.johannessen@nersc.no](mailto:johnny.johannessen@nersc.no)

## Table of contents

<b>Overall project goal and short description</b>	3
<b>WP 1. Management</b>	3
<b>WP 2. Pattern recognition based sea ice motion algorithm</b>	4
WP2.1 - Acquisition and pre-processing of Envisat ASAR data	4
WP2.2 - Application of the algorithm on co- and cross-polarisation data	4
WP2.3 - Evaluation and validation of results	6
<b>WP 3. Sea ice motion from combining pattern recognition and Doppler shift</b>	7
WP3.1 - Retrieval of sea ice motion fields from SAR Doppler shift information	7
3.1.1. Doppler Calibration	7
3.1.2. Sea ice motion field from SAR Doppler shift	11
WP3.2 Doppler velocities in areas with little features	17
WP3.3 Add Doppler velocities to pattern tracking vectors	18
WP3.4 Evaluation of the combined algorithm	20
3.4.1 Limitations and advantages of the combined algorithm	20
<b>Summary and Outlook</b>	22
Key findings	22
Outlook for processing of Sentinel-1 data	23
<b>References</b>	24

## Overall project goal and short description

Since the mid-1990's sea ice displacement estimates based on low-resolution scatterometers and passive microwave radiometers have been widely used for determination of the sea ice motion and its long-term monitoring. In recent years Synthetic Aperture Radar (SAR) data have demonstrated abilities to estimate high-resolution sea ice displacement and deformation fields (see [1] for refs). With the growing amount of SAR data (Radarsat-2, Sentinel-1A/1B) now gradually becoming available for near real-time sea ice monitoring it is timely to develop and implement a systematic processing system to determine SAR-based sea ice drift and deformation. Such a system would efficiently allow for better contribution of SAR data to:

- quantify the distribution of sea-ice mass and freshwater equivalent;
- assess the sensitivity of sea ice to climate change;
- understand thermodynamic and dynamic feedbacks to the ocean and atmosphere;
- assimilate sea ice motion into coupled sea ice-ocean models;
- secure uptake of this monitoring capability into the Copernicus Marine Environment Monitoring Service (CMEMS).

Originally the DESICE project aimed to exploit SAR data from Sentinel-1 to generate new sea ice motion fields based on combined use of pattern matching and Doppler shift data with spatial resolution of order 1 km and temporal resolution of 3-5 days. Such high-resolution sea ice drift data are not yet systematically provided and will be important to study sea ice deformation (divergence, convergence and shear), lead formation, ridging and opening and formation of thicker and thinner sea ice as well as other regional and local sea ice processes. The resulting products provided with a given accuracy will also ensure real time application including sea ice forecasting, environmental monitoring, tracking pollution embedded in ice, and support to ice operations and navigation.

The project implementation capitalizes on the results of another ESA funded project (PRODEX ISAR), led by Morten W. Hansen, from which processing routines and data access are provided.

**Table 1:** Description of Work-packages

Work-package	Description
WP1	Management
WP2	Pattern recognition based sea ice motion algorithm
WP3	Sea ice motion from combining pattern recognition and Doppler shift

### WP 1. Management

The problems and delays with the Sentinel-1 Doppler shift estimation had severely impacted the project. This unfortunate long delay was not foreseen at the onset of the project. As there is no firm indication of exact dates for when a solution for these problems can be found a fall-back solution was proposed and agreed in the fall of 2017 whereby the project is entirely refocused to apply and study the recently reprocessed archive of Envisat ASAR data over the Arctic Ocean and sub-polar seas. Nevertheless the approach and results of this refocused study is expected to be highly valuable for later analyses of Sentinel-1 based Doppler velocities over sea ice.

A consequence of this refocusing, moreover, lead to a rotation and change of key personnel. As such Dr. Anton Korosov stepped in while Dr. Jeong-Won Park was replaced with Dr. Mohamed Babiker. Dr. Jeong-Won Park is contributing to the project in kind. These changes in study objectives and personnel have had no financial implication for PRODEX funded DESIce project.

## WP 2. Pattern recognition based sea ice motion algorithm

The combined feature tracking and pattern matching algorithm, initially developed for Sentinel-1 data [1], was adapted for processing data ENVISAT/ASAR and applied for retrieving sea ice drift at high spatial resolution from ASAR scenes in the Fram Strait in January 2010. The quality of the algorithm was improved by using the cross-polarisation channel as input and accounting for rotational movement of the sea ice. In addition the Hessian of maximum cross-correlation matrix was utilized for improving robustness of sea ice drift retrieval.

### WP2.1 - Acquisition and pre-processing of Envisat ASAR data

A total of 1740 raw Envisat ASAR images has been acquired for the range Doppler processing. For the intercomparison of sea ice drift estimates based on the Doppler retrieval method and the pattern recognition algorithm a subset of 44 L1 ENVISAT ASAR images has been used. The open-source Python toolbox 'Nansat' [2] developed at NERSC was used for opening the ASAR files and calculating the Normalized Radar Cross Section (NRCS).

### WP2.2 - Application of the algorithm on co- and cross-polarisation data

An efficient algorithm was developed for processing the SAR data based on the combination of feature tracking (FT) [3] and pattern matching (PM) [4] techniques. At the first step, FT is applied to a pair of SAR images covering the same area at a given time interval  $dT$ .

FT automatically identifies keypoints (distinct features) in the images and describes each keypoint with a vector of 256 binary descriptors [3]. The keypoints are matched using the brute-force matching (all keypoints on one image are compared to all keypoints on another image) and the Hamming distance (number of the descriptors in the vector with different values). For each keypoint on the first image, a ratio between the smallest and the second smallest Hamming distance to keypoints on the second image is computed. If the ratio is below a threshold, the keypoints with the smallest Hamming distance are considered as matched.

As a result, FT provides the location of matched features characterized by pixel/line coordinates on the first image  $(x_1, y_1)$  and corresponding coordinates on the second image  $(x_2, y_2)$ . Although FT is very fast, the generated vectors are heterogeneously distributed in space. Note that in this form, this set of drift vectors cannot be used further for studying, e.g., sea ice deformation, as it is a scale-dependent dynamical process. Therefore, the ice drift is to be further estimated on a regular grid with a given resolution.

At the second step, the FT results are approximated at the regular grid or, generally speaking, in any point inside the overlap between the two SAR images. The approximation by a linear interpolation [5] is performed in the geographic space between the matched keypoints. In the surrounding area, the approximation is performed using an N-th-order polynomial.

At the third step, the approximated ice drift is used as the first guess for the precise PM technique in the following order. Azimuth angle  $(a_0)$  between the SAR scenes is calculated based on the georeference information. A template  $t$  is subset from Image 1 around a starting point of interest with coordinates  $X_1, Y_1$  and size  $T \times T$  pixels (Fig. 2-1, A).

The template  $t$  is rotated within the range of angles  $[a_0 - b, a_0 + b]$  with step  $b_0$ . For each rotation, cross-correlation matrix  $r$  is calculated between the rotated template  $t_{rot}$  and  $s$  (Fig. 2-1, B and C). The rotation that provides maximum cross-correlation is recorded (Fig. 2-1, D). The position  $(X_2, Y_2)$  of the cross-correlation maximum  $r_{max}$  is found in the cross-correlation matrix  $r$  [4].

Ice drift components  $U$  and  $V$  are found by converting  $X_1, Y_1$  and  $X_2, Y_2$  into geographic coordinates and calculating corresponding eastward and northward displacement. If the cross-correlation maximum  $r_{max}$  is below a predefined threshold  $r_{min}$ , the derived drift vector is discarded as unreliable.



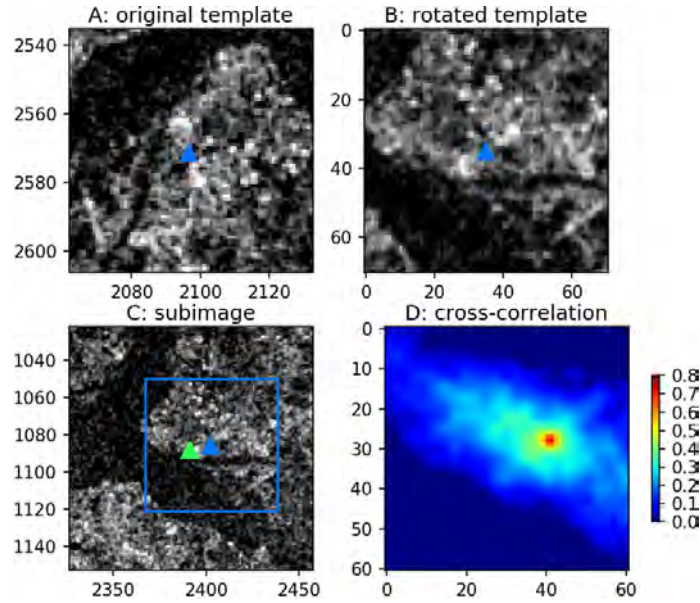


**Figure 2-1.** Explanation of the maximum cross-correlation (MCC) method with rotation. (A) Template  $t$  ( $71 \times 71$  pixels) is taken from Image 1 around the starting point shown as the blue triangle; (B) the template is rotated by  $210^\circ$  ( $t_{rot}$ ); (C) sub-image  $s$  ( $101 \times 101$  pixels) is taken from Image 2 around the first guess point (green triangle); the blue boundary and the blue dot indicate the position and the center of the template, which corresponds to the best match; (D) the cross-correlation matrix  $r$  is computed from the rotated template  $t_{rot}$  and the subimage  $s$ .

The combined FT and PM ice drift algorithm was initially developed for Sentinel-1 SAR data and had to be adapted for ENVISAT ASAR. Several changes have been applied comparing to the default parameters described in [2]:

- Only co-polarization channel (HH) was used as the cross-pol channel was not available;
- The ASAR image was not downscaled to keep resolution of the end product sufficiently high;
- The incidence angle correction of NRCS for sea ice [7] was applied;
- The NRCS values from HH were converted from floating point to integer datatype by linear scaling from the range  $[-5, -20]$  dB;
- The FT algorithm was initialized from 200000 points to assure sufficient number of matched features;
- Size of template was chosen to be  $50 \times 50$  pixels;

A major improvement of the PM algorithm was the introduction of a new measure of ice drift retrieval quality. We discovered that the sharpness of the peak on the cross-correlation matrix corresponds to retrieval error. Low, flat peaks are usually found on images with low contrast where retrieval errors are high. If the image is sharp and ice doesn't undergo significant deformation, then retrieval errors are low and the peak is very high and sharp. It was decided to characterize the peakiness by the Hessian vector - the values of second partial spatial derivative of the cross correlation matrix at the location of cross-correlation maximum:

$$H_{ij} = \left[ \frac{\partial^2 r}{\partial x^2}, \frac{\partial^2 r}{\partial y^2} \right],$$

where  $r$  is cross-correlation matrix,  $x$  and  $y$  are row and column directions,  $i$  and  $j$  are coordinates of the cross-correlation maximum.

It was found that in most of the cases correlation of Hessian and MCC is quite high (elongated cloud of dark violet points on Fig. 2-2) and high values of H or MCC correspond to low error. There are, however, quite many points which have high MCC but also quite high error (yellow - green points in the lower part of the scatter-plot on Fig. 2-2). That indicates that high MCC is not always a good indicator of high ice drift retrieval quality. At the same time, there are almost no points that have high Hessian and high error. A threshold of 0.12 can therefore be safely used for discarding potentially rogue drift vectors.

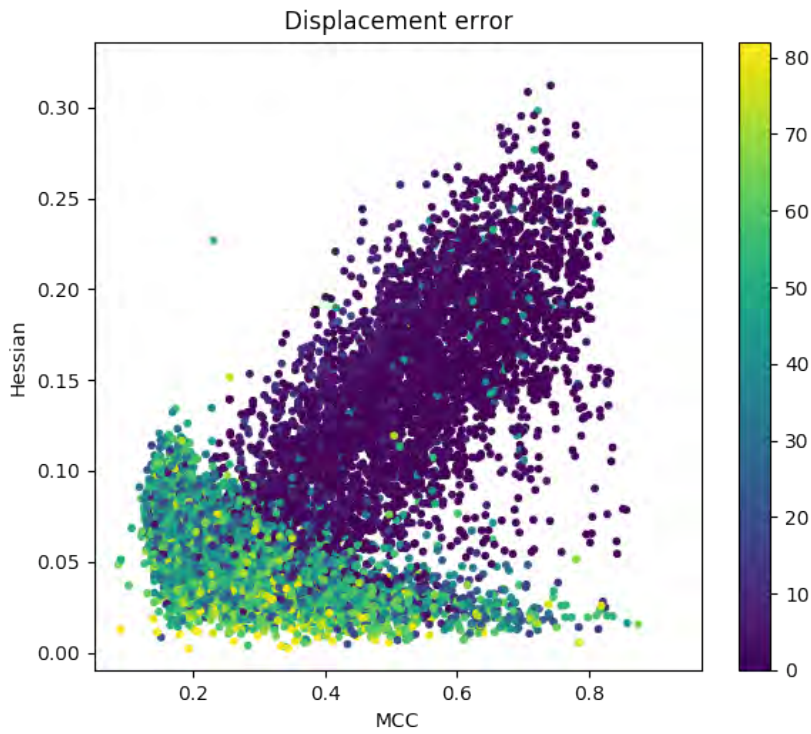


**Figure 2-2.** Comparison of maximum cross-correlation (X), Hessian (Y) and retrieval error (color) for Sentinel-1 SAR matchups with drifting buoys from the N-ICE experiment.

### WP2.3 - Evaluation and validation of results

Validation of the algorithm was performed on an independent subsample of Sentinel-1 SAR match-ups with in situ ice drifting buoys from the N-ICE2015 experiment [6]. The combined algorithm is capable of deriving sea ice drift with high accuracy ( $r = 0.99$ ,  $E = 286 \pm 3$  m) for a wide range of displacement magnitude (up to 300 km). The retrieved drift is negligibly biased ( $-39$  and  $71$  m in X- and Y-directions), and the error is log-normal distributed.

Sea ice drift velocity retrievals from co-polarization channel (HH) and from cross-polarization channel (HV) were compared. We found that in the HV channel the contrast between ice and water backscatter is higher. As a result the number of matchups with high correlation and with lower RMSE is also higher when we apply the HV channel (Fig. 2-3).

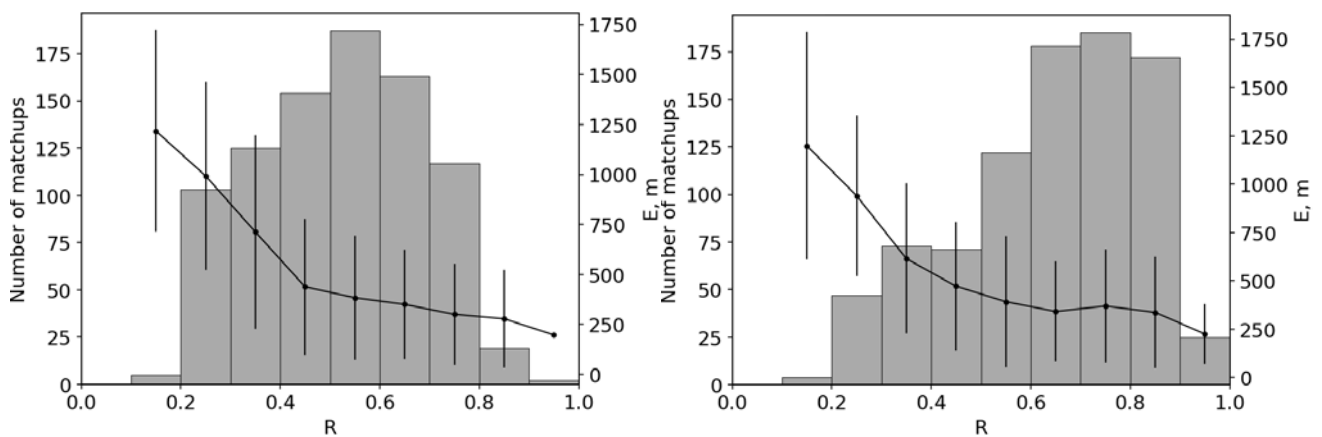


**Figure 2-3.** Dependence of the number of match-ups (left axis, gray bars) and retrieval error  $E$  (right axis, black solid line with error bars) on maximum cross-correlation (X-axis) for HH (left) and HV (right) polarizations.



## WP 3. Sea ice motion from combining pattern recognition and Doppler shift

### WP3.1 - Retrieval of sea ice motion fields from SAR Doppler shift information

SAR Doppler is a unique application that can extract instantaneous range-directed velocity field at no extra cost in all kinds of existing SAR system. The Doppler shift in the received echo after a proper calibration is directly related to the target's motion in line-of-sight (LOS) direction, and the conversion factor from the Doppler shift to the ground projected velocity is as follows:

$$v = \frac{\lambda}{2 \sin \theta} f_D \quad (1)$$

where  $\lambda$  is the wavelength,  $\theta$  is the incidence angle,  $f_D$  is the Doppler frequency, and  $v$  is the target velocity. The main applications of SAR Doppler were ocean wind and/or surface current retrieval [8] and ground moving target indication [9], and recently the Doppler measurements were tested for retrieving sea ice drift field [10,11].

The main challenges for extending Doppler application to sea ice motion are the low speed of the sea ice drift, which ranges from 2-23 cm/s in Fram Strait [12], and several uncertainties in the Doppler estimation procedure. Regarding the former issue, the measurement precision must be higher than the expected Doppler shift. However, the instantaneous speed can be higher than the known averaged speed considering typical non-linearity of the drift. In terms of Doppler frequency, an error of 1 Hz would translate to an error in the ground velocity of 6.7 cm/s at 25° incidence angle using Envisat ASAR system. Hence the accuracy of the absolute Doppler should be better than 2 Hz for detecting the moderate ice drift. The latter issue is related to the system and processing related calibration. Previous studies were only able to suppress the measurement uncertainty down to 5 Hz [10-12], which is not enough for sea ice application. If possible, the Doppler processor must be calibrated precisely so that the uncertainty does not exceed the lower limit for sea ice application, 2 Hz here.

In this section, we examine an extensive set of Envisat ASAR ScanSAR data to improve the Doppler calibration, and then evaluate the feasibility of extending Doppler measurement for retrieving sea ice motion field with combined use of the conventional cross-correlation (CC) based drift estimation.

#### 3.1.1. Doppler Calibration

The Doppler centroid shift measurement from any SAR sensor must be calibrated for non-geophysical biases. We follow the approach described in [13] with several improvements that makes the calibration more precise. The raw uncalibrated Doppler shifts can be modelled as follows:

$$f_{D,raw} = f_{D,geo} + f_{D,elec} + f_{D,phys} \quad (2)$$

where  $f_{D,geo}$  is the geometric Doppler which is related to the relative motion between the SAR antenna and the rotating Earth surface,  $f_{D,elec}$  is the electronic mispointing originated by misalignment and failure of antenna transmit/receive module, and  $f_{D,phys}$  is the geophysical Doppler that induced by the true motion of the target. The raw Doppler,  $f_{D,raw}$ , was calculated using NORUT GSAR processor which includes full azimuth band SAR focusing and side-band correction [14]. Doppler calibration is a procedure that eliminates non-geophysical terms,  $f_{D,elec}$  and  $f_{D,phys}$ , from  $f_{D,raw}$ .

For establishing and validating calibration parameters, we collected the entire Envisat ASAR ScanSAR mode data acquired for one full repeat cycle (35 days) from January 1 to February 4, 2010. The number of processed strips were 1328 and 414 for HH and VV polarization, respectively.

##### 3.1.1.1. Geometric Doppler ( $f_{D,geo}$ )

The geometric Doppler can be calculated by solving the range-Doppler equations as described in [15]. For Envisat ASAR, key parameters like roll, pitch, and yaw steering angles, and orbital state

vectors are available with high precision so that the uncertainty is expected to be sufficiently low. The yaw and pitch steering for each position along the satellite orbits are defined by the Altitude and Orbit Control System (AOCS) rotation amplitudes,  $\alpha_{\theta}$ ,  $\alpha_{\phi}$ ,  $\alpha_{\psi}$ , and the satellite hour angle (satellite osculating true latitude in the true of date coordinate system, see [16]),  $\theta_{\theta}$ , as follows:

$$\alpha_{\theta} = \alpha_{\theta} \cos \theta_{\theta} \quad (3)$$

$$\alpha_{\phi} = \alpha_{\phi} \sin 2\theta_{\theta} \quad (4)$$

$$\alpha_{\psi} = \alpha_{\psi} \cos \theta_{\theta} \left(1 - \frac{(\alpha_{\theta} \cos \theta_{\theta})^2}{3}\right) \quad (5)$$

The AOCS rotation amplitudes and pitch, roll and yaw mispointing with respect to the controlled reference frame are in Envisat common restituted attitude auxiliary files (AUX\_FRA\_AX). Precise orbital state vectors are available from the DORIS product (DOR\_VOR\_AX). In this way, it should be possible to predict accurate geometric Doppler. However, the attitude control is not perfect in most time so that normally the predicted geometric Doppler is biased from the actual measurements by few tens of Hz as in Fig. 3-1. This is because even small amount of antenna misalignment along satellite body axes can make significant Doppler offset as reported in [17].

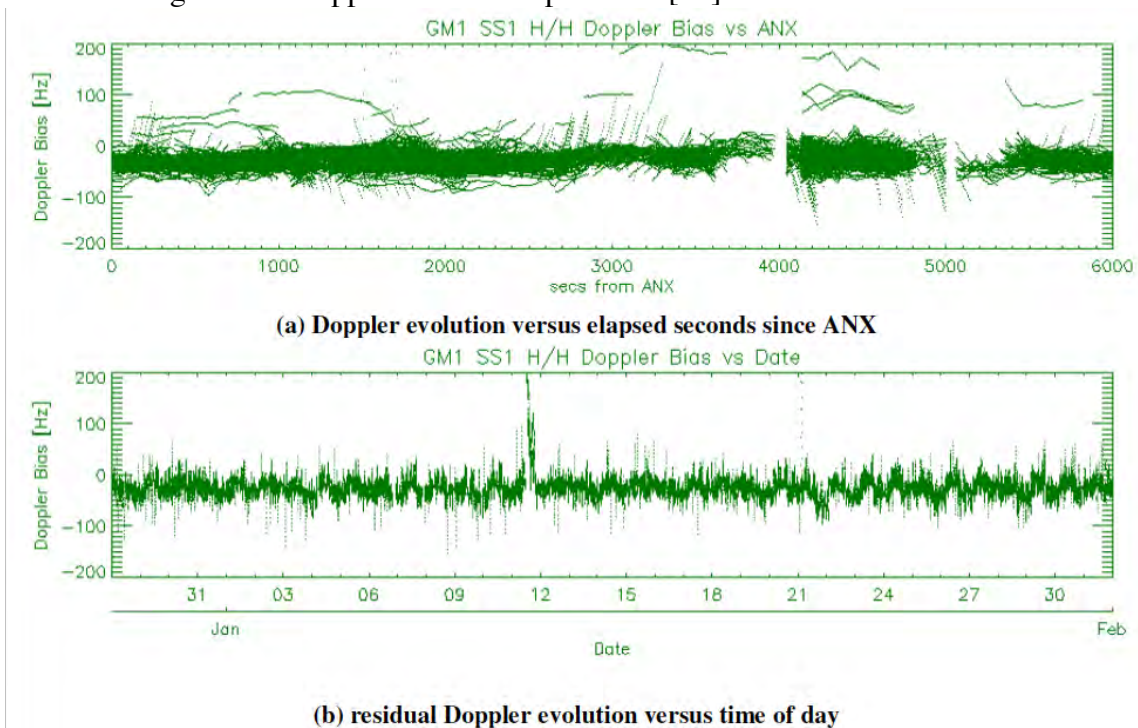


**Figure 3-1.** Residual Doppler centroid evolution for GM1 data (copied from Fig. 4.5 in [18])

Considering any unexpected/untracked attitude anomalies along the orbits during the mission, this misalignment contribution must be estimated from the data by comparing estimated Doppler centroid with predicted Doppler centroid over land coverage. The idea is to examine the shape of residual Doppler centroid along range axis after compensating the expected geometric Doppler. If the geometric Doppler was correctly calculated, only the effects from electronic mispointing remains in the residual Doppler over land pixels. However, when yaw and pitch angles include errors, the Doppler shift changes with range position (equivalently look angle) in a linear manner and is biased from 0 Hz. Fig. 3-2 shows exemplary residual Doppler profiles with and without attitude errors. The linear slope (orange dashed line) in the top panel indicates positive error in yaw angle, while the pitch angle error induces offset. By finding appropriate angles that make the residual Doppler profile be detrended and unbiased, the antenna misalignment angles can be retrieved. Using this approach, the derived misalignments were  $0.209^\circ$  and  $0.026^\circ$  in yaw and pitch angle, respectively. These numbers are similar to the previously reported values in [17], which are  $0.21^\circ$  and  $0.02^\circ$ .

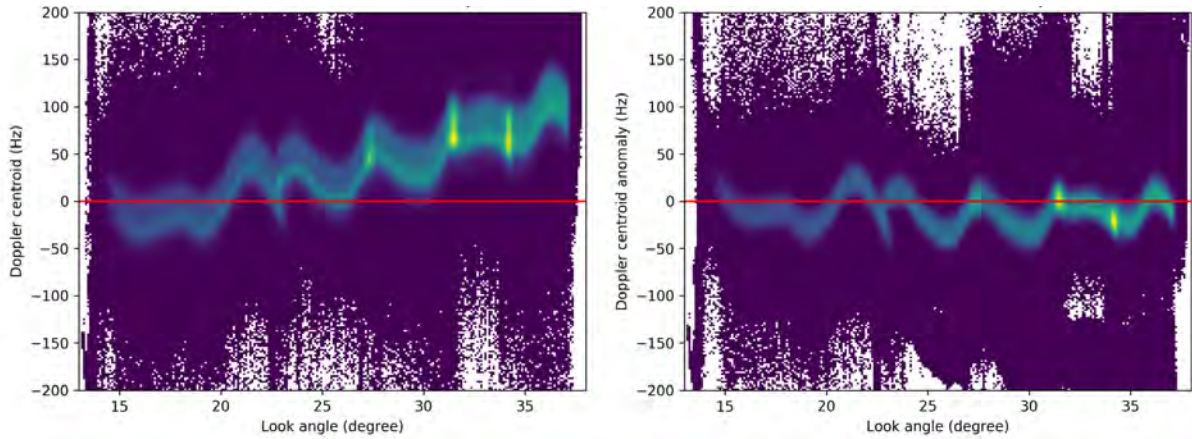


**Figure 3-2.** Averaged residual Doppler profile of HH-polarization from many strips after compensating the geometric Doppler. (Left) Combined effect of incorrect yaw and pitch angles. If the yaw angle has error, there is a linear trend along range axis, while pitch angle induces offset from 0 Hz. (Right) The same range profile after correcting errors in yaw and pitch angles.

After removing  $\Delta f_{\text{geom}}$  from  $\Delta f_{\text{res}}$ , there were residual Doppler shift changes associated with satellite hour angle (or satellite osculating true latitude). Fig. 3-3 shows the averaged residual Doppler in 10-degree-bin of the satellite hour angles and their best fit curve. The pattern is very similar to a typical geometric Doppler itself, however the amplitude is much lower and the sign is opposite. The best fit curve was made by adopting a model function that combines slightly modified form of the Envisat's steering law in (3) and (4).

$$[-6.2 \times \sin^2(\theta_{\text{sat}} + 0.15) - 90.5] + [10.2 \times \sin^2(2\theta_{\text{sat}} + 0.15) + 90.9] \quad (6)$$

where  $\theta_{\text{sat}}$  is the satellite hour angle. Since the best fit curve follows the estimation with RMSE of 1.9 Hz, the geometric Doppler correction combined with the residual drift correction using (6) can be considered qualified for estimating small changes in Doppler shift. As shown in Fig. 3-4, the averaged Doppler profile looks much clearer after correcting the residual geometric Doppler.

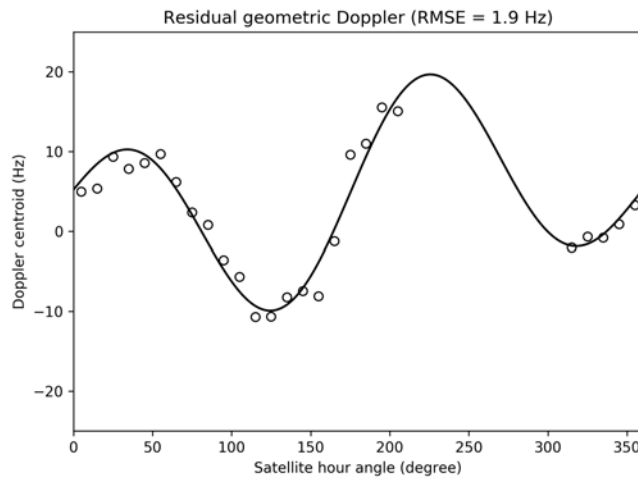


**Figure 3-3.** Estimated residual Doppler drift after compensating the geometric Doppler. Solid line represents the best-fit curve.

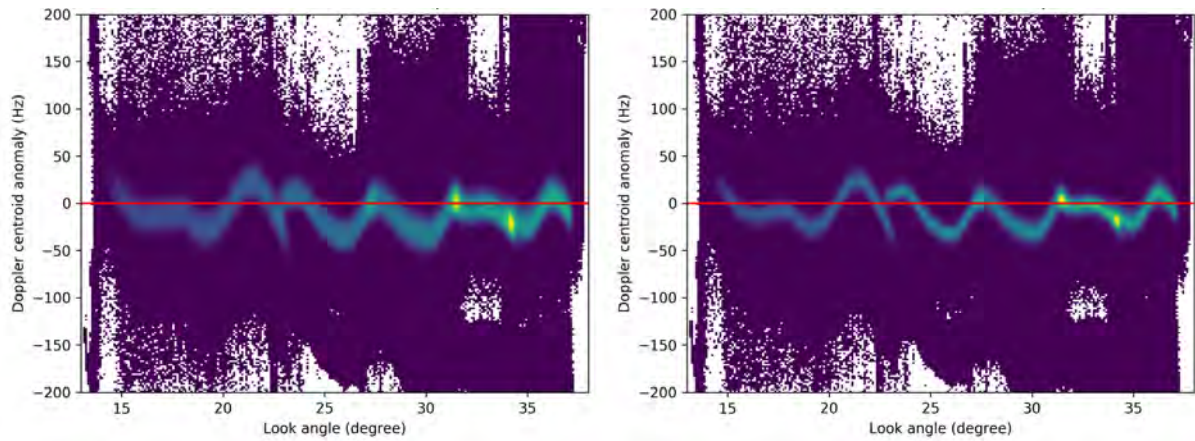


**Figure 3-4.** Averaged residual Doppler profile of HH-polarization before (Left) and after (Right) residual geometric Doppler correction.

### 3.1.1.2. Electronic mispointing ( $\Delta\theta$ )

The electronic mispointing can be derived either from the antenna model or directly from the observed SAR data. The former requires several parameters that are not publicly available, and the error is up to 5 Hz [19], which translates to a velocity difference of 33 cm/s at an incidence angle of  $25^\circ$ . Considering the range of the monthly-averaged sea ice drift speed, this error is too large. Since the electronic mispointing is a function of antenna look angle, a look-up table can be made from extensive Doppler measurements over land pixels by taking the mean Doppler anomaly corrected for the geometric Doppler at each look angle bin.

Antenna look angle is an important information that must be calculated precisely during the computation of the geometric Doppler. Topographic height must be considered in order to get actual look angle rather than taking nominal values from sensor-target distances. Fig. 3-5 shows how the local topography affects the actual look angle. When the sensor-target distance,  $R$ , is given with satellite position, the actual target position is ambiguous without target's height information. The nominal look angle, which is displayed as  $\theta$  in Fig. 3-5, refers to the angle when the radar beam hits the ground on the Earth ellipsoidal model. However, there is a top of mountain at the same distance  $R$ , and the look angle for this point is different from  $\theta$  by  $\Delta\theta$ . By nature of the radar system, the backscattered signal from these two points are registered in the same position in the slant range geometry. Hence the actual look angle must be calculated for each pixel in the SAR image by adopting topography information. In practice, this is done in the step of the geometric Doppler computation where the antenna pointing vector is calculated for solving range-Doppler equation for each pixel in the image.

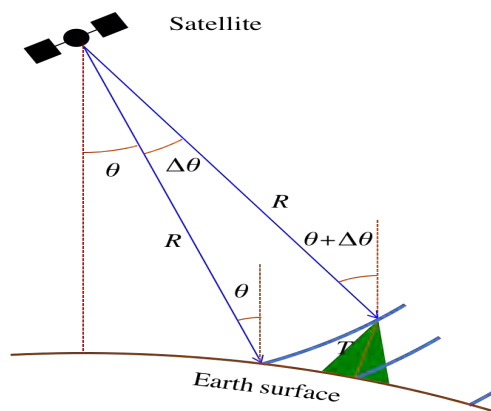


**Figure 3-5.** Nominal and actual look angles for the point at the same distance.

The previous approach for estimating electronic mispointing was to take an azimuth-averaged Doppler anomaly for each range bin with limited use of land pixels which have topographic height lower than 100 m [13]. However, the number of samples should be large and the geographic



distribution should be diverse in order to make a reliable look-up table. Fig. 3-6 shows an extreme case of look angle changes by topographic height in a single scene. Clearly the Doppler shift induced by electronic mispointing is not consistent at each range bin, and the shift is correlated with topographic height.

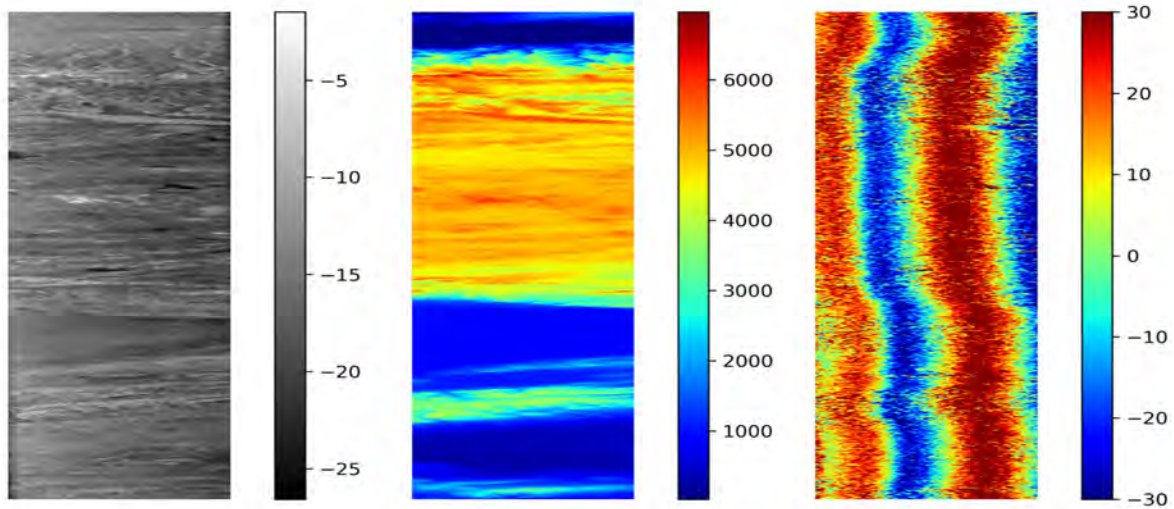


**Figure 3-6.** An extreme case showing the correlation between topographic height and electronic mispointing. (Left) sigma naught, (Center) radar-coded topographic height, (Right) Doppler frequency corrected for geometric Doppler.

This topography induced look angle shift is important both in computing the geometric Doppler and in estimating electronic mispointing from real data, because the height changes over land ranges up to 9 km around the Earth surface. Note that 1 km of height difference at a  $25^\circ$  incidence angle induces 2.7 Hz of geometric Doppler and a  $0.13^\circ$  look angle shift.

After calculating the correct look angles for land pixels from many strips, a look-up table for electronic mispointing can be made by taking median values of Doppler frequency for each look angle bins. Fig. 3-7 represents the Doppler mispointing of all five sub-swaths (SS1-SS5) for HH and VV polarization channels. Once a look-up table is generated, it can be used for compensating Doppler mispointing from any image. This look-up table approach is particularly important when retrieving geophysical Doppler for an image which does not have enough coverage for entire range bins, which is a very typical case over ocean/sea ice.

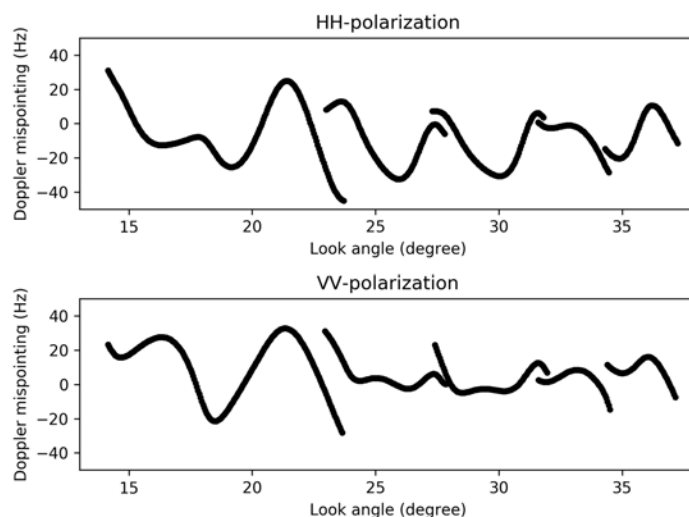


**Figure 3-7.** Estimated Doppler frequency anomaly caused by electronic antenna mispointing: (Top) HH-polarization, (Bottom) VV-polarization.

### 3.1.2. Sea ice motion field from SAR Doppler shift

Among the collected ScanSAR strips over the Fram Strait, we applied the developed Doppler calibration algorithm for image strips over north-east Greenland Sea where the sea ice motion is

relatively fast. Considering the acquisition geometry, we selected images from the ascending path only. Fig. 3-8. shows monthly average of sea ice motion field in January 2010.

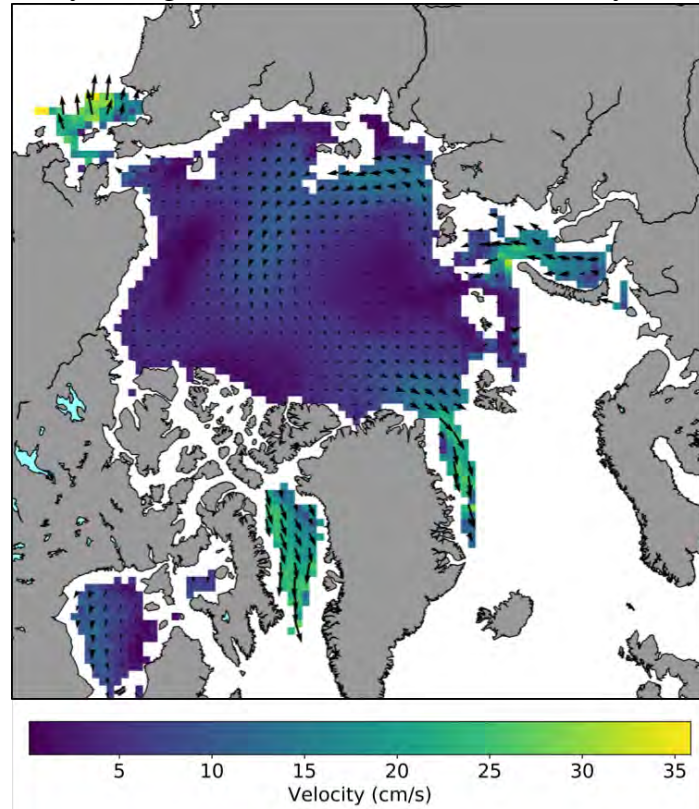


**Figure 3-8.** Averaged sea ice motion field in January 2010 (source data from OSI SAF, <http://osisaf.met.no>)

### 3.1.2.1 Intercomparison of individual SAR Doppler scenes

Fig. 3.9 shows an example of Doppler-derived instantaneous velocity field and its corresponding pattern matching based mean velocity field. The image was taken over north-eastern part of Greenland on 1st of January, 2010. The SAR Doppler based velocity (Fig. 3.9(b)) was available for almost every pixels in the image while the pattern matching based velocity (Fig. 3.9(d)) was determined only where distinct feature/pattern exists. The overall velocity directions and magnitudes match well. Since the instantaneous velocity can be different from the mean velocity, motion vectors are different locally. Note that the overall measurements from Doppler looks more noisier. Fig. 3.10-11 display similar examples taken on different dates. Although the magnitudes of the two velocities cannot be directly compared considering the non-linearity of general sea ice motion, the overall pattern shows good correlation: Contrast between non-moving fast ice and the drifting ice, and the moving direction. In general, the Doppler measurements for the sub-swath 1 (SS1) include distortions which come from incomplete corrections for electronic mispointing. Unlike other sub-swaths (SS2-SS5), the sub-swath 1 has more complex shape in the electronic mispointing as shown in Fig. 3.7, and the conversion factor in the Eq.3-1 is higher, which means that a small error can result in more severe error in the subswath\_1.

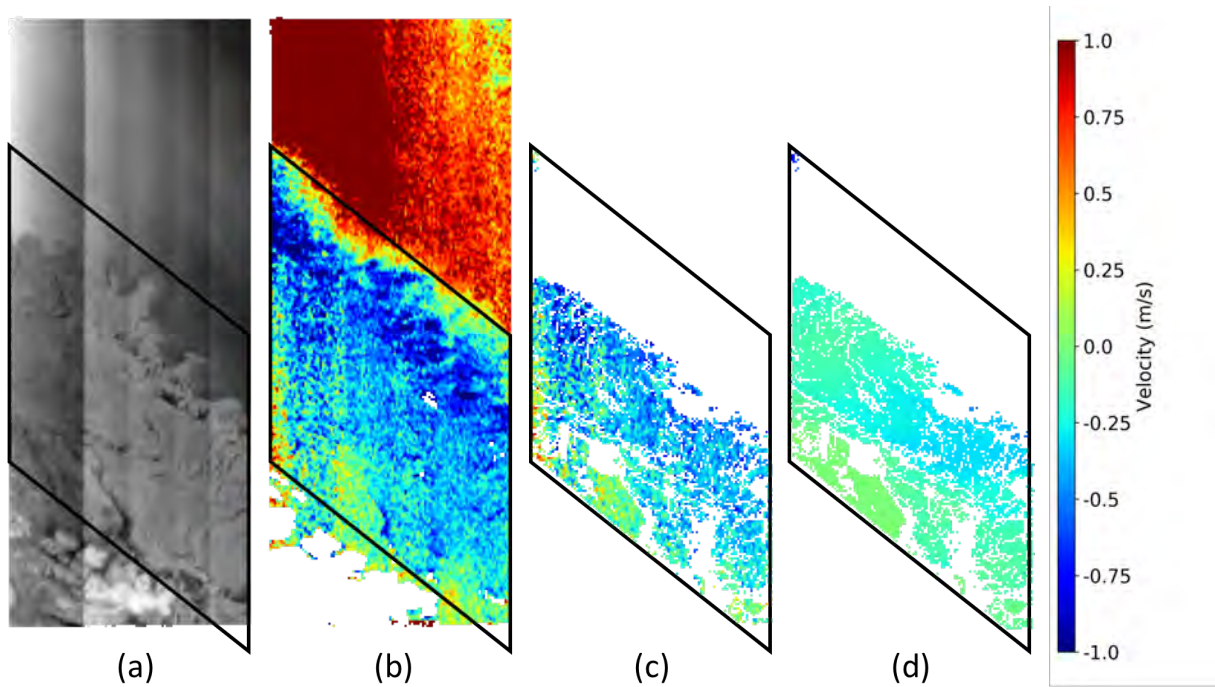


**Figure 3-9.** Comparison of the SAR Doppler derived instantaneous velocity and the pattern recognition based mean velocity (ASA\_WS\_\_OPNPK20100101\_205338\_000001612085\_00358\_40993\_3764.N1). (a) backscattering intensity, (b) Doppler derived instantaneous velocity, (c) masked version of (b) using the valid points in (d) pattern matching derived mean velocity.

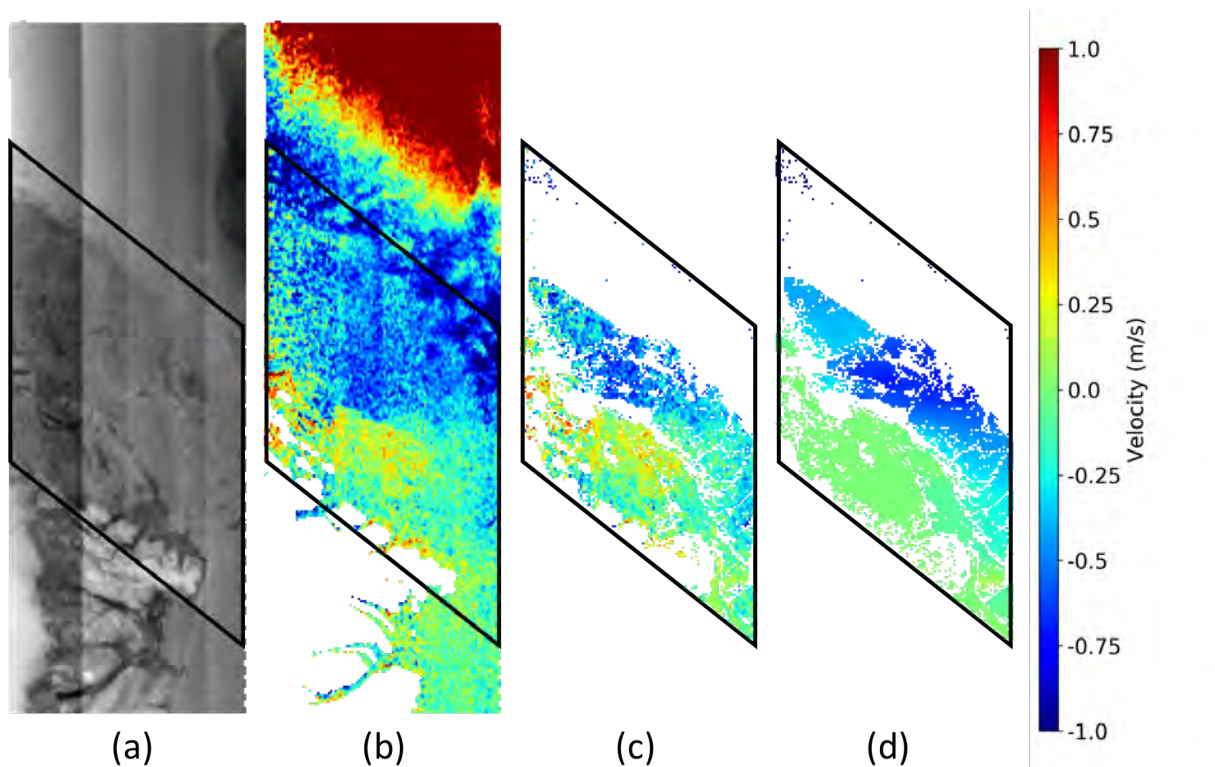


**Figure 3-10.** Comparison of the SAR Doppler derived instantaneous velocity and the pattern matching based mean velocity (ASA\_WS\_\_OPNPK20100126\_210800\_000002252086\_00215\_41351\_4245.N1). (a) backscattering intensity, (b) Doppler derived instantaneous velocity, (c) masked version of (b) using the valid points in (d) pattern matching derived mean velocity.



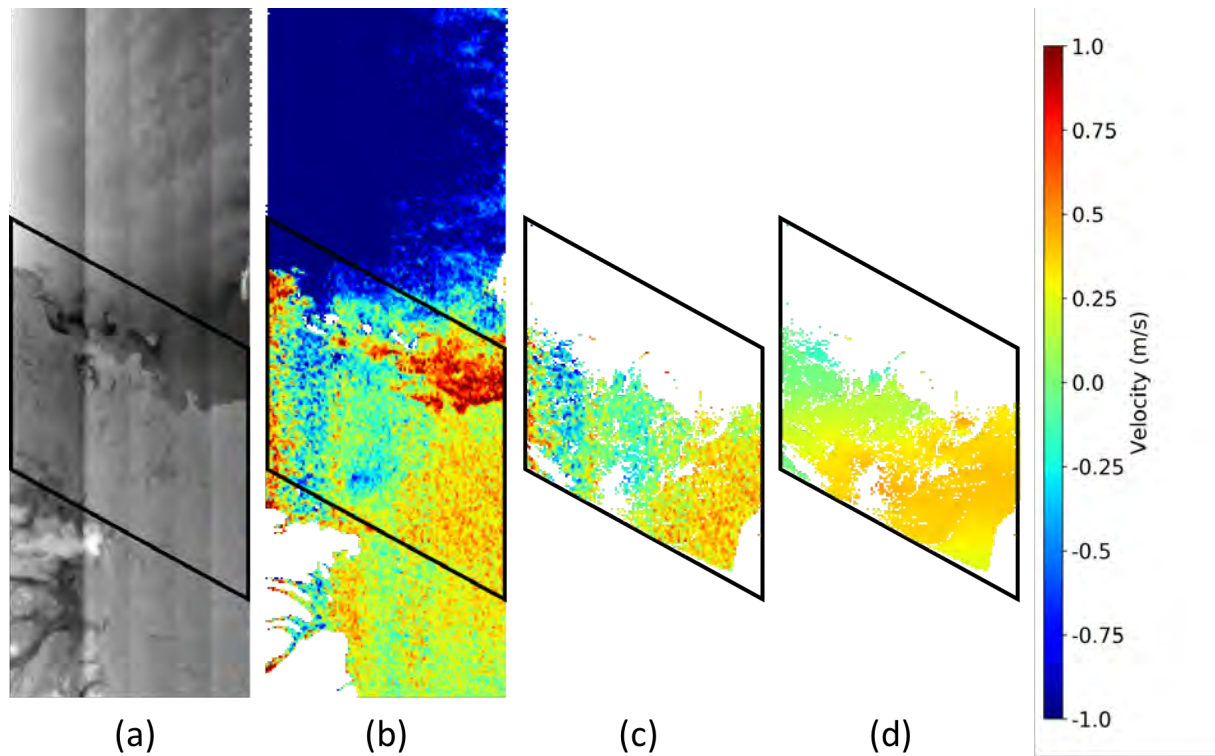


**Figure 3-11.** Comparison of the SAR Doppler derived instantaneous velocity and the pattern matching based mean velocity (ASA\_WS\_0PNPDK20100203\_201518\_000003332086\_00329\_41465\_4404.N1). (a) backscattering intensity, (b) Doppler derived instantaneous velocity, (c) masked version of (b) using the valid points in (d) pattern matching derived mean velocity.

### 3.1.2.1 Intercomparison of time averaged sea ice drift

In order to evaluate the similarity between the two velocities from two different methods, time averaged data were compared. We selected 10 image strips over nearly the same area, and averaged the derived velocities. Table 3-1 summarizes the data used for averaging.

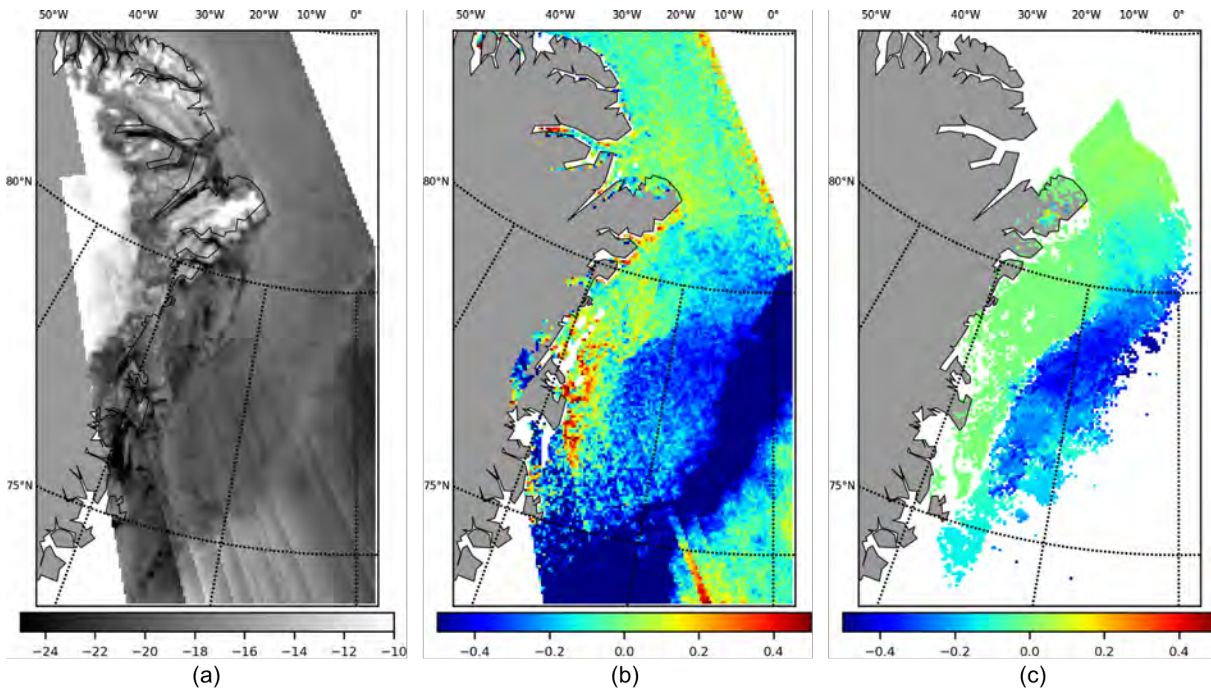
**Table 3-1.** SAR data used in the experiment

Scene ID for Doppler measurement	Scene ID for pattern matching (Master/Slave)
ASA_WS_0PNPDK20100101_205338_000001612085_00358_40993_3764.N1	ASA_WSM_1PNPDK20100101_205336_000001712085_00358_40993_3536.N1 ASA_WSM_1PNPDK20100102_120523_000003672085_00367_41002_3610.N1
ASA_WS_0PNPDK20100103_213100_000001612085_00387_41022_3800.N1	ASA_WSM_1PNPDK20100103_213058_000001712085_00387_41022_3879.N1 ASA_WSM_1PNPDK20100102_120523_000003672085_00367_41002_3610.N1
ASA_WS_0PNPDK20100104_205923_000002522085_00401_41036_3820.N1	ASA_WSM_1PNPDK20100104_205921_000002632085_00401_41036_4065.N1 ASA_WSM_1PNPDK20100103_113327_000003552085_00381_41016_3778.N1
ASA_WS_0PNPDK20100114_204502_000002322086_00043_41179_4020.N1	ASA_WSM_1PNPDK20100114_204500_000002452086_00043_41179_5886.N1 ASA_WSM_1PNPDK20100115_115646_000003062086_00052_41188_5974.N1
ASA_WS_0PNPDK20100117_205043_000002592086_00086_41222_4075.N1	ASA_WSM_1PNPDK20100117_205041_000002692086_00086_41222_6441.N1 ASA_WSM_1PNPDK20100117_123155_000003612086_00081_41217_6351.N1
ASA_WS_0PNPDK20100126_210800_000002252086_0	ASA_WSM_1PNPDK20100126_210758_000002392086_0



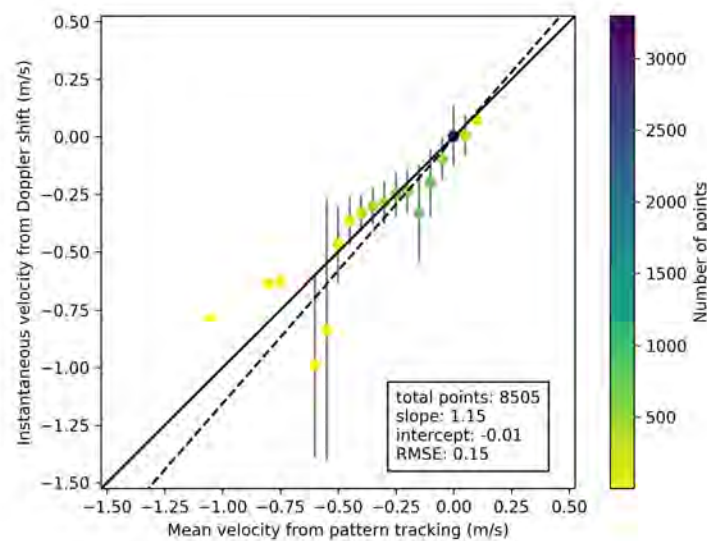
0215_41351_4245.N1	00215_41351_8165.N1 ASA_WSM_1PNPDK20100127_121945_000004472086_00224_41360_8270.N1
ASA_WS_0PNPDK20100127_203646_000002122086_00229_41365_4268.N1	ASA_WSM_1PNPDK20100127_203644_000002202086_00229_41365_8367.N1 ASA_WSM_1PNPDK20100127_121945_000004472086_00224_41360_8270.N1
ASA_WS_0PNPDK20100129_211345_000002232086_00258_41394_4312.N1	ASA_WSM_1PNPDK20100129_211343_000002322086_00258_41394_8767.N1 ASA_WSM_1PNPDK20100130_122104_000004402086_00267_41403_8853.N1
ASA_WS_0PNPDK20100130_204135_000001942086_00272_41408_4334.N1	ASA_WSM_1PNPDK20100130_204133_000002022086_00272_41408_8981.N1 ASA_WSM_1PNPDK20100130_122104_000004402086_00267_41403_8853.N1
ASA_WS_0PNPDK20100203_201518_000003332086_00329_41465_4404.N1	ASA_WSM_1PNPDK20100203_201516_000003432086_00329_41465_9753.N1 ASA_WSM_1PNPDK20100203_115938_000003982086_00324_41460_9643.N1

Fig. 3-12 shows the averaged results for (a) uncalibrated backscattering power, (b) Doppler-derived velocity, and (c) pattern matching-derived velocity. The ice-water boundary can be recognized from the backscattering image and the Doppler-derived velocity map as well. This indicates another potential use of Doppler for investigating marginal ice zone where the ice motion is different from typical large ice floe. As mentioned before, the Doppler-derived velocity map covers almost every pixels in the given source data, while the pattern matching-derive velocity map has successive observation only over the area with distinct features. The sharp boundaries between non-moving fast ice and drifting ice are clearly seen in both results. A quantitative comparison between the two velocity fields is shown as one-to-one scatter plot in the Fig. 3-13. The slope was 1.15, which indicates the instantaneous velocity was 15% faster than the mean velocity, however, this changes from scene to scene as the actual short-term motion of sea ice is highly heterogeneous. Intercept and RMSE are more important parameters here, since they tell how the two genuinely different velocity are related. The intercept was -0.01 m/s, which means the two time averaged velocity fields have negligible difference in their mean. The RMSE indicates how the two velocities disagree in time series.



**Figure 3-**

**12.** Comparison of time averaged velocity fields from (b) SAR Doppler derived instantaneous velocity and (c) pattern matching based mean velocity. The ice-water boundary is recognizable in both (a) the backscattering power and (b) the Doppler derived instantaneous velocity.



**Figure 3-13.** Comparison of time averaged velocity fields from Doppler derived instantaneous velocity and pattern matching based mean velocity.

Since the sensitivity for geophysical motion is different for each sub-swath primarily due to the different in the antenna look angle, we also investigated the relationship between the Doppler-derived velocity and the pattern matching-derived velocity for each sub-swath separately. Fig. 3-14 shows the results for all five sub-swaths (SS1-SS5). As expected from the conversion factor in Eq. 3-1, the matching is better in the far-range sub-swath (SS4-SS5) than in the near-range sub-swath (SS1-SS2). The higher RMSE in SS1 is partly because of the incomplete compensation of the electronic mispointing as shown in Fig. 3.9-11.

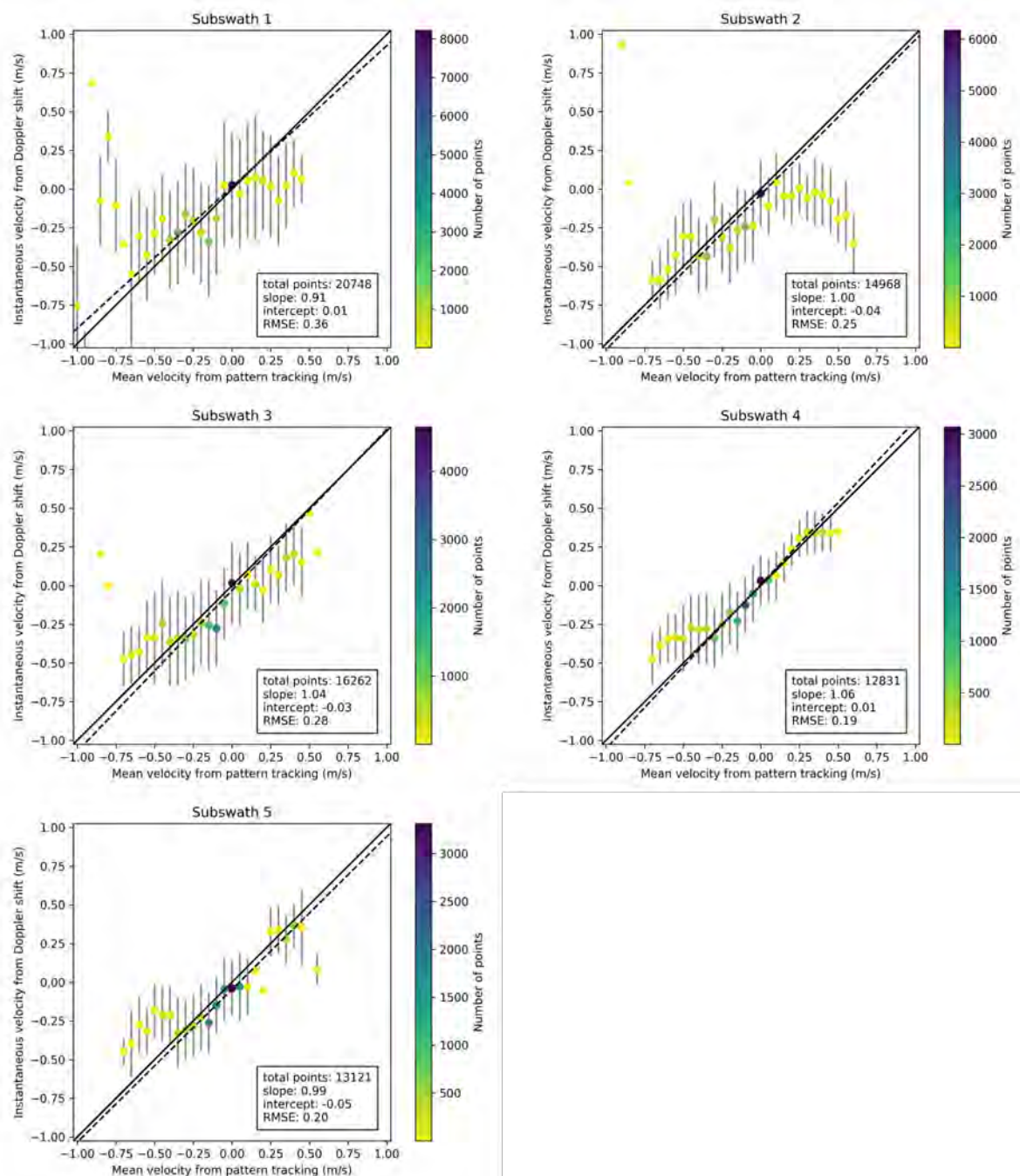


**Figure 3-14.** Subswath-wise comparison of time averaged velocity fields from Doppler derived instantaneous velocity and pattern matching based mean velocity.

### WP3.2 Doppler velocities in areas with little features

The pattern matching algorithm relies on a robust correlation between an image from day 1 and a template from day 2. First year and multi-year sea ice as well as pack ice exhibit distinct features on SAR images originating from inhomogeneities of roughness, pressure ridges, refrozen leads, etc. These features don't rapidly change over time unless ice undergoes melting or deformation. That allows to apply the pattern matching algorithm for areas with stable, undeformed ice and even for individual ice floes. But in the zones of deformation or in other areas where sea ice changes rapidly, for example, in the marginal ice zone (MIZ), the pattern matching fails and gaps in the sea ice drift product occur. At the same time, the instantaneous velocity derived from the Doppler signal is available in the entire swath of observations independent of ice conditions.

We have compared coverage of the ice drift products originating from the pattern matching and the Doppler algorithms. Ice edge was manually detected on images with radar backscatter. Area covered by sea ice and area covered by the pattern matching ice drift product were intercompared for



all available 22 scenes. It was found that the pattern matching product on average covers only  $63\pm 6\%$  of sea ice. The rest of the area belongs to the MIZ or zones with strong deformation.

Figure 3-15 below illustrates comparison of radar backscatter and instantaneous velocity from Doppler with sea ice edge and pattern matching product coverage on four examples. A large gap between the ice edge (shown as black line) and areas where pattern matching performs well (masked by white color) is visible on these examples. Closer look at the radar backscatter image reveals that it is slash and pancake ice typical for MIZ which dominates in these areas. It is also visible that in the middle of the pack there are smaller gaps, often elongated as lineaments. They correspond to sea ice convergence and shear zones appearing between fast ice and floating ice and between ice floes.

The observed gaps are filled with velocity observations from Doppler. Although being noisy, these observations are very valuable. They can show a clear separation between sea ice and open water motion. But in order to be combined with the pattern matching velocities the Doppler velocities have to be calibrated as described in the next section.

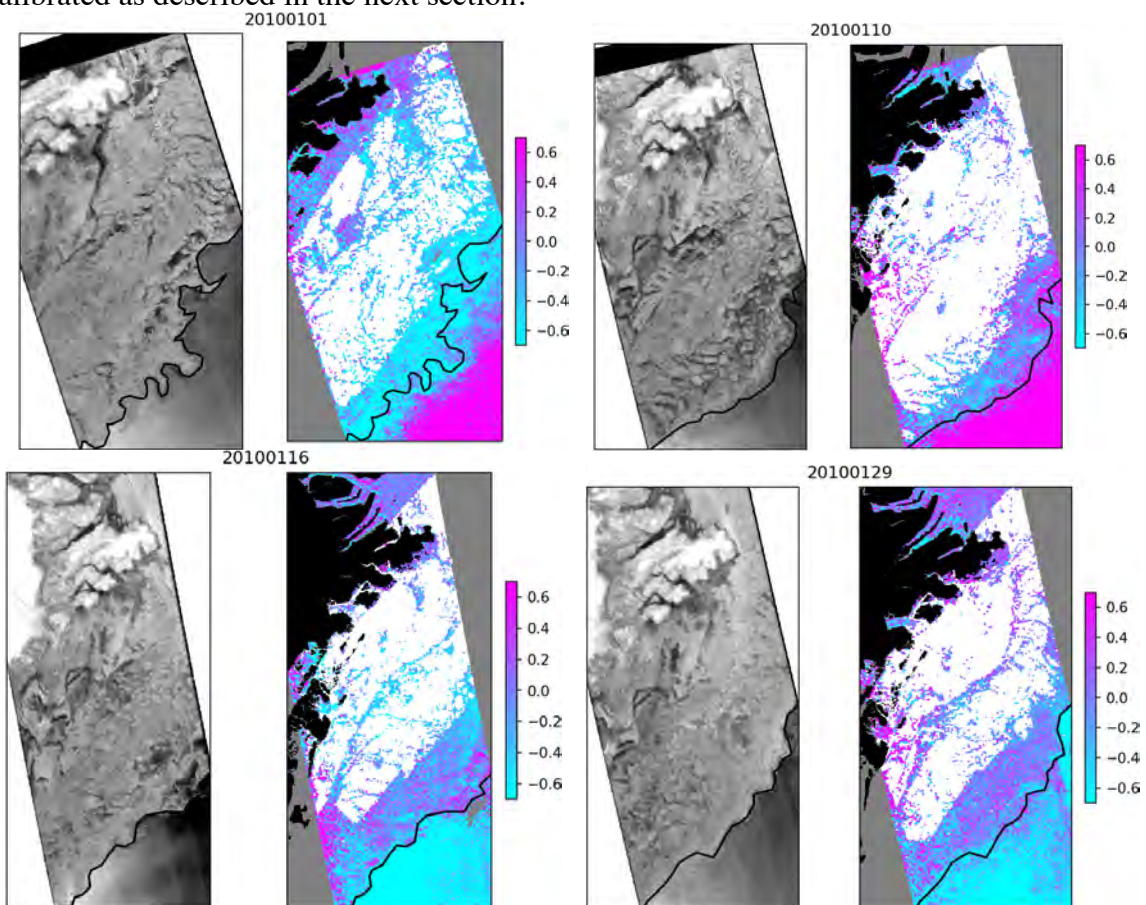


**Figure 3-15.** Examples of normalized radar backscatter (grayscale image), sea ice edge (black line) and Doppler derived instantaneous velocity (colored image, m/s) for four dates: 1, 10, 16 and 29 January 2010. The black color on the velocity image shows land mask, gray color shows areas out of ASAR swath and white color shows areas where the pattern matching algorithm performed well.

### WP3.3 Add Doppler velocities to pattern tracking vectors

Since the Doppler-based velocity measurement has enough sensitivity for deriving ice motion over almost all ice-covered area as shown in the WP 3.1, the Doppler measurement can be utilised to fill gaps where the pattern matching fails. An essential procedure for doing this includes assimilation of instantaneous velocity into mean velocity. Considering the non-linearity of the ice motion, the assimilation is only valid when a stationarity of the ice motion can be assumed.

The example in the Fig. 3-10 is the case because the two velocities match well. The basic strategy is, i) scaling the Doppler derived motion field using the slope and intercept from one-to-one scatter plot, ii) smoothing the scaled Doppler based motion field to suppress noise, and iii) fill the gaps in the pattern matching derived motion field using the rescaled and smoothed Doppler derived motion field. In the Fig. 3-16, the area defined with white lines is sea ice covered area. As shown in Fig. 3-

10(d), although the pair used for pattern matching covers most of the ice covered area, the derived motion field has much smaller coverage as indicates with black lines in the Fig. 3-16. The rest area is to be filled with the Doppler derived measurements. Fig. 3-16(c) shows the original Doppler derived motion field which has slightly different pattern and values from the pattern matching derived motion field in Fig. 3-16(b).

Fig. 3-17 displays a scatter plot of the two measurements for the common points. By scaling using the slope and intercept and filtering with 5x5 median filter, the Doppler derived motion field changes into Fig. 3-16(d). The final merging result in Fig. 3-16(e) looks well balanced except for the boundaries on the upper left side of the black lines. Since the instantaneous velocity and the mean velocity have different nature, it is impossible to match them perfectly, but clearly the Doppler measurement can be used for increasing mapping coverage with marginal disagreement. Recall that the mean RMSE for time averaged product was 0.15 m/s in the Fig. 3-13.

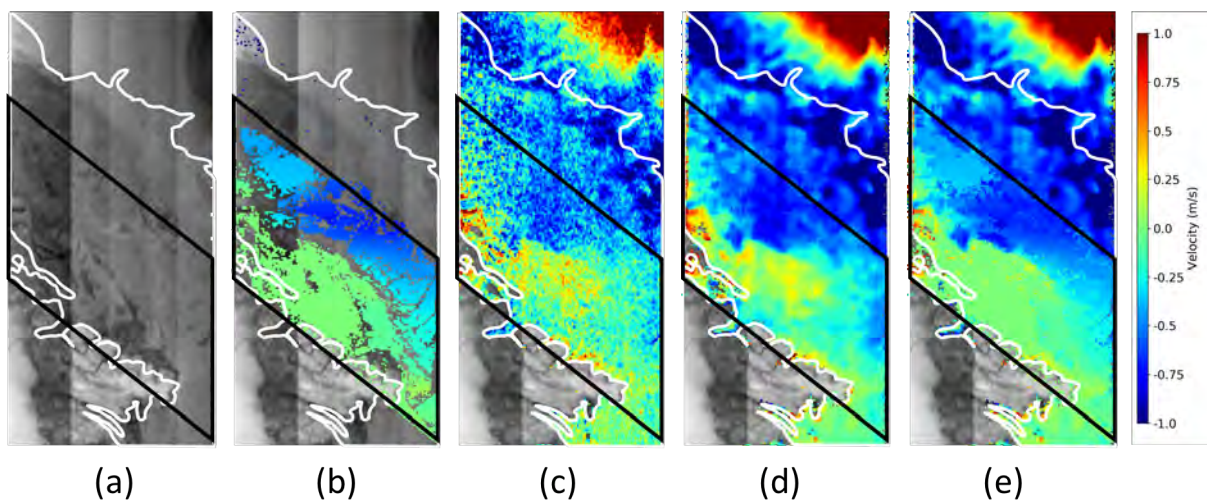


**Figure 3-16.** Combining two velocity measurements by adjusting Doppler based velocity to pattern matching based velocity. Area surrounded by white and black lines indicate sea ice coverage and the derived motion field from pattern matching, respectively. (a) backscattering intensity. (b) velocity field derived from pattern matching. (c) velocity field from Doppler. (d) adjusted and smoothed velocity field by assimilating (c) into (b). (e) combined velocity field.

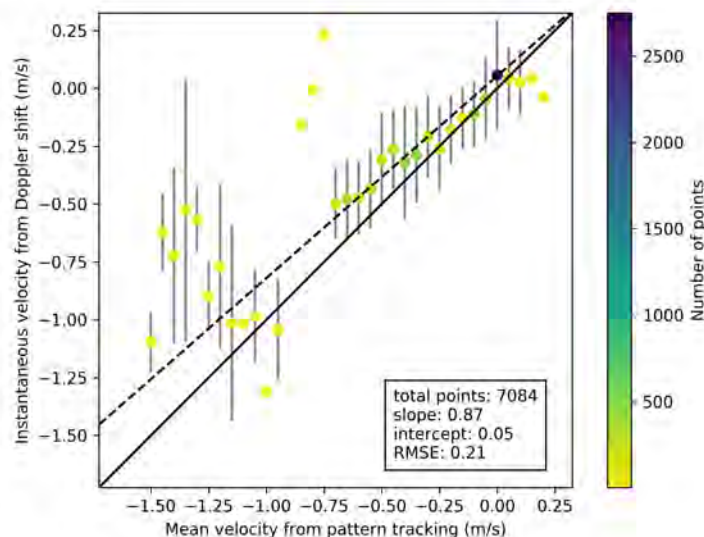


**Figure 3-17.** Scatter plot for common points in Fig. 3-15 (b) and (c). The slope and intercept are used for assimilating Doppler result into pattern matching result as shown in Fig. 3-15 (c)-(d).

## WP3.4 Evaluation of the combined algorithm

### 3.4.1 Limitations and advantages of the combined algorithm

As the direct quantitative validation of the combined algorithm was not possible due to absence of collocated ice drifting buoys in this region in January 2010 and even lower spatial resolution and accuracy of other sea ice drift products (e.g. derived from passive microwave observations) we had to perform a qualitative evaluation.

Due to several uncertainties in the Doppler estimation procedure (see sec. 3.1) the resulting sea ice drift product has generally rather high noise and low sensitivity to the motion of sea ice. The signal-to-noise ratio estimated over the sea ice is close to 1.15. Fig. 3-18 compares a transect of the range components of ice drift speed computed using the pattern matching (orange line) and the Doppler (blue line) algorithms taken along azimuth direction on 1 Jan 2010. It confirms that the Doppler product is somewhat sensitive to actual ice drift but is significantly contaminated with noise.

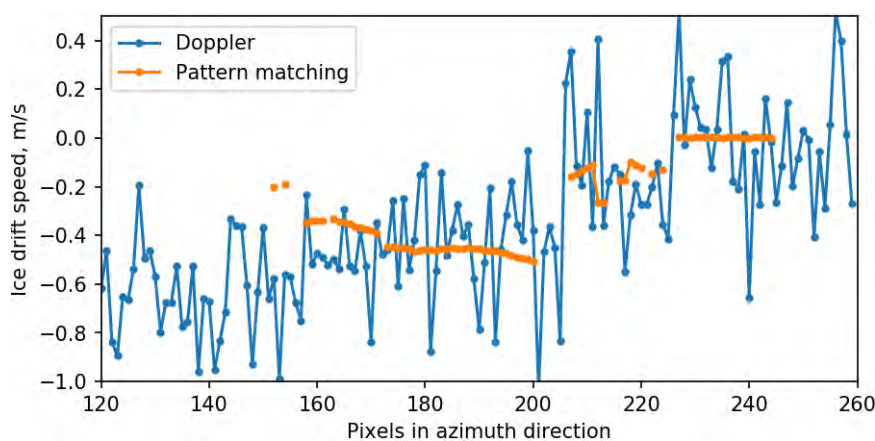


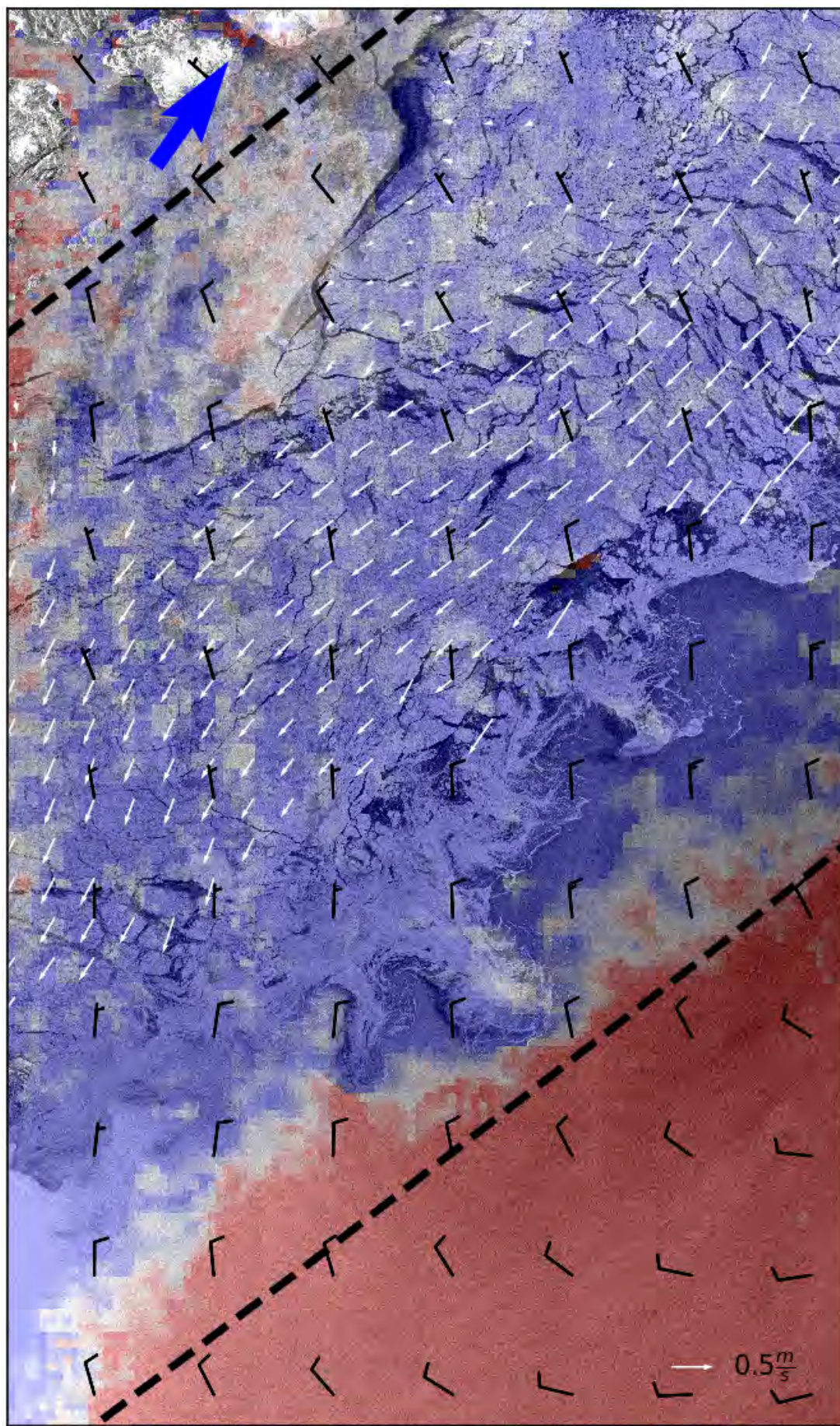
**Figure 3-18.** Values of sea ice drift speed derived using pattern matching (orange line) and Doppler algorithms along a transect from a SAR scene taken on 1 January 2010.

The Doppler product has relatively high spatial resolution (pixel size is 1000 x 1000 m) but in order to reduce noise it has to be filtered with low-pass filter and the effective resolution is reduced to approximately 5 km product. In the Fram strait, where sea ice drifts with sufficiently high speed for detection with Doppler, the only possible configuration for remote sensing is the ascending orbit, when the ENVISAT swath crosses the ice flow at approximately 45° angle. On the descending orbit the ENVISAT flies almost parallel to the ice flow. The ascending orbit crosses the Fram strait approximately every 36 hours.

The aforementioned issues limit possible applications of the Doppler product and combination with the pattern matching algorithm. Due to high noise we cannot derive instantaneous deformation of the sea ice field. Due to low frequency of observations we cannot study relation between instantaneous velocity and average drift speed in details. Due to only one possible orbit configuration we cannot extract two ice drift components from the Doppler product and can use only the range component.

Nonetheless the Doppler algorithm has a great advantage: it provides the range component of ice drift speed in the marginal ice zone and deformation zones where pattern matching does not work. By filling the gaps and extrapolating ice drift field it helps qualitative analysis and understanding the processes of ice/ocean/atmosphere interaction on the case-by-case basis. Fig. 3-19 illustrates the advantage of combining pattern matching (shown as white arrows) with Doppler (shown as blue/red hue) and with auxiliary products (wind speed and direction is shown by wind barbs, SAR image is in the background). Thick dashed lines show boundaries of the second SAR scene taken from descending orbit along the sea ice flow and used for the pattern matching. Blue arrow shows the North direction, map of the scene location is shown on Fig. 3-20.





Doppler instantaneous velocity  
-0.4 -0.2 0.0 0.2 0.4

Figure 3-19. Ice drift in the Fram strait (see text above for explanations).



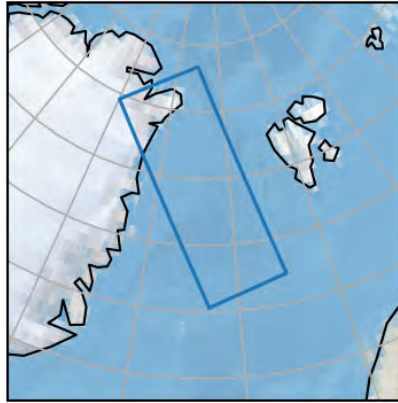


**Figure 3-20.** Location of the SAR scene from Fig. 3-18 is marked by blue rectangle.

Fig. 3-19 reveals that sea ice drifts southwards along the Greenland coast (note direction of white arrows and blue hue of the image indicating negative U component). The fast ice, located in the upper part of the scene, has zero speed as indicated by both the pattern matching (short white arrows) and Doppler (very light-blue hue or no hue) products. As observed only by the Doppler, ice in the MIZ drifts with the highest speed (deep blue hue). Drift of the pack ice in the Fram strait is driven mostly by the East Greenland Coastal Current, however the elongated tongues of slash/pancake ice in the MIZ are driven by the northern wind (shown by black wind bars). It is astonishing how well the Doppler signal corresponds to the sea ice extent visible on the background SAR image. In the open ocean south-western winds generate waves propagating northwards as very well captured by the Doppler (red hue). Small patches without any hue in the MIZ probably indicate locations of the surface motion in the azimuth direction and may correspond to location of the mesoscale eddies at the edge of the East Greenland Current.

## Summary and Outlook

### Key findings

- The combined feature tracking and pattern matching algorithm has been adapted for deriving high resolution sea ice drift from ENVISAT ASAR data. The algorithm has quite high accuracy (ice displacement errors are below 300 m) but does not perform well in the marginal ice zone (MIZ) or in strong deformation zones. The algorithm was outfitted with a new quality measure computed as Hessian of the cross-correlation matrix reflecting peakiness of the cross-correlation maximum.
- Doppler calibration is crucial for identifying relatively slow-moving geophysical phenomenon s like sea ice drift. Considering the sensitivity of Doppler shift to actual motion in LOS direction, the signal uncertainty must be lower than 2-3 Hz. The proposed calibration scheme effectively removes errors comes from attitude anomaly and antenna mispointing which are generic for all SAR sensors including Sentinel-1. The resulting calibrated Doppler signal showed largely reduced uncertainty (RMSE: 1.9 Hz for geometric Doppler correction) and well balanced measurements except the first subswath (SS1), of which native antenna pattern is complex and the sensing geometry is not favorable compared to the other subswaths. Nevertheless, the Doppler calibration has an advantage in universal Doppler observation capability regardless land correction which has been considered crucial for Doppler calibration of individual scenes.
- Sea ice drift in the Fram Strait was derived using both the pattern matching and the Doppler algorithms from 22 SAR scenes in January 2010. The correlation between instantaneous range-directed drift velocity derived from the individual Doppler scenes and drift speed derived from pairs of SAR scenes is quite low due to noise in the Doppler signal and the differences in the temporal scales. Intercomparison of the products averaged over one month (January 2010) showed overall high consistency of the two products (RMSE: 0.15 m/s, slope: 1.15). The



difference is the largest for the first sub-swath (RMSE: 0.36 m/s, slope: 0.9) and decays with incidence angle (RMSE: 0.2 m/s, slope: 0.99).

- Despite the low signal-to-noise ratio, low efficient resolution and only one component of the drift vector, the Doppler algorithm proves to be very useful for complementing the pattern-matching algorithm in the MIZ and ice deformation zones. An approach for assimilation of the Doppler instantaneous velocity into ice drift mean speed is proposed and its efficiency is illustrated in a case study.

### Outlook for processing of Sentinel-1 data

Since the quality of the geophysical Doppler shift provided in the OCN product of Sentinel-1 EW mode is not good enough for application in ice velocity retrieval (see, e.g., Fig. 3-21), various correction schemes needs to be developed. An application of Doppler measurement to sea ice motion extraction is feasible only after successful correction is achieved. The required corrections are i) geometric Doppler compensation for each burst, ii) offset compensation for inter-subswath, and iii) electronic mis-pointing correction. The first correction is specific for Sentinel-1 TOPSAR mode, which steers the antenna beam forward at each burst. This can be easily compensated by correcting the effect of antenna elevation pattern in the level-0 data as suggested in [20]. The latter two corrections are generic for any SAR sensor. Since the OCN product is currently not available over the Arctic and there is an issue on attitude steering of Sentinel-1, we conducted our research using historical Envisat ASAR ScanSAR data.

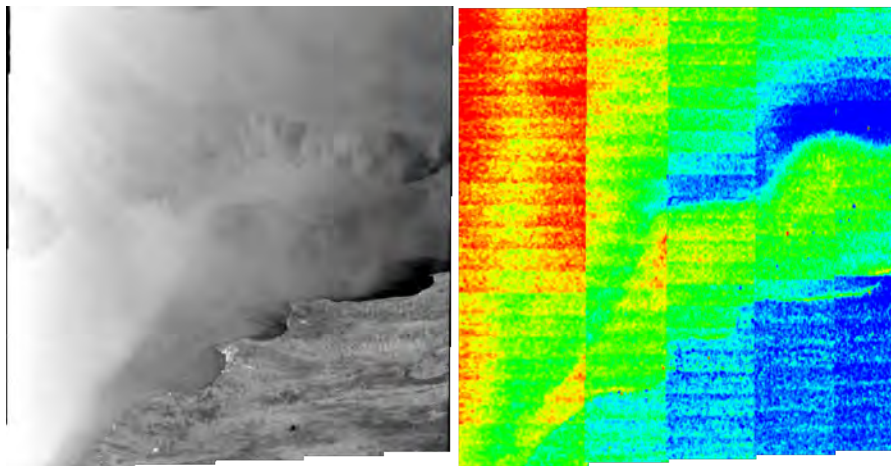


**Figure 3-21.** An example of Sentinel-1 OCN product.

We believe that the Doppler calibration and combination of motion vector derivation algorithms developed in this study has important implications for improving utilization of Doppler centroid shift from Sentinel-1 data. Since the developed Doppler calibration scheme is straightforward and universal for any SAR sensor, the only adaptation required for Sentinel-1 is the corrections specific for TOPSAR that we mentioned above. Once the burst-wise antenna elevation pattern correction is made, the scalloping along azimuth direction in Fig. 3-21 will disappear. The slow varying shaping along the range direction in each subswath and discontinuities between subswaths are related to electronic antenna mispointing. These anomalies can be safely removed by the developed Doppler calibration procedure in this study. Once the TOPSAR related corrections are made and the developed Doppler calibrations are applied, the use of Doppler with Sentinel-1 A/B is expected to produce more informative sea ice motion field thanks to its improved temporal and spatial resolution than Envisat ASAR. Since the Doppler derived velocity represents instantaneous snapshot of the target's motion, the more the Doppler data are time averaged, the more reliable and comparable the Doppler derived velocities with the pattern matching derived velocities.

## References

- [1] Korosov A.A. and Rampal P., “A combination of feature tracking and pattern matching with optimal parameterization for sea ice drift retrieval from SAR data,” *Remote Sens.*, vol. 9, no.3, 258, doi:10.3390/rs9030258, Mar. 2017
- [2] Korosov A.A., Hansen M.W., Dagestad K.-F., Yamakawa A., Vines A., Riechert M., “Nansat: a Scientist-Orientated Python Package for Geospatial Data Processing,” *J. Open Res. Softw.* vol. 4, no.1, e39, doi:10.5334/jors.120, Oct. 2016
- [3] Lowe, D. G., “Distinctive Image Features from Scale-Invariant Keypoints,” *Int. J. Comput. Vis.*, vol. 60, no.2, pp.91–110, Nov. 2004
- [4] Brunelli, R. *Template Matching Techniques in Computer Vision: Theory and Practice*, John Wiley & Sons, Paris, France, 2009
- [5] Jones, E., T. Oliphant, and P. Peterson, SciPy: Open source scientific tools for Python, 2001–. Available online: <http://www.scipy.org/> (accessed on 11 January 2017)
- [6] Itkin, P., G. Spreen, B. Cheng, M. Doble, F. Girard-Ardhuin, J. Haapala, N. Hughes, L. Kaleschke, M. Nicolaus, and J. Wilkinson, “Thin ice and storms: Sea ice deformation from buoy arrays deployed during N-ICE2015,” *J. Geophys. Res.*, vol. 122, no. 6, pp. 4661–4674, Jun. 2017
- [7] Zakhvatkina, N., A. Korosov, S. Muckenhuber, S. Sandven, and M. Babiker, “Operational algorithm for ice–water classification on dual-polarized RADARSAT-2 images,” *Cryosphere*, vol. 11, pp. 33–46, doi:10.5194/tc-11-33-2017, Jan. 2017
- [8] Chapron, B., F. Collard, and F. Ardhuin, “Direct measurements of ocean surface velocity from space: Interpretation and validation,” *J. Geophys. Res.*, vol. 110, no. C7, pp. 1–17, Jul. 2005
- [9] Park, J.-W., and J.-S. Won, “An efficient method of Doppler parameter estimation in the time–frequency domain for a moving object from TerraSAR-X data,” *IEEE Trans. Geosci. Remote Sens.*, vol. 49, no. 12, pp. 4771–4787, Dec. 2011
- [10] Kræmer, T., H. Johnsen, and C. Brekke, “Emulating Sentinel-1 Doppler radial ice drift measurements using Envisat ASAR data,” *IEEE Trans. Geosci. Remote Sens.*, vol. 53, no. 12, pp. 6407–6418, Dec. 2015
- [11] Hansen, M. W., K. Kloster, K.-F. Dagestad, S. Sandven, J. A. and Johannessen, “Retrieval of sea ice drift from SAR Doppler shift,” in *Proc. ESA Living Planet Symposium*, Bergen, Norway, 28 Jun. - 2 Jul. 2010, ESA SP-686
- [12] Smedsrud, L. H., M. H. Halvorsen, J. C. Stroeve, R. Zhang, and K. Kloster, “Fram Strait sea ice export variability and September Arctic sea ice extent over the last 80 years,” *Cryosphere*, vol. 11, pp. 65–79, Jan. 2017
- [13] Hansen, M. W., F. Collard, K.-F. Dagestad, J. A. Johannessen, P. Fabry, and B. Chapron, “Retrieval of sea surface range velocities from Envisat ASAR Doppler centroid measurements,” *IEEE Trans. Geosci. Remote Sens.*, vol. 49, no. 10, pp. 3582–3592, Oct. 2011
- [14] Engen, G., and H. Johnsen, “High-precision Doppler frequency estimation for ocean applications,” in *Proc. SEASAR*, Tromsø, Norway, 18–22 Jun. 2012, ESA SP-704
- [15] Cumming, I. G., and F. H. Wong, *Digital Processing of Synthetic Aperture Radar Data: Algorithms and Implementation*, Norwood, MA, USA, Artech House, 2005
- [16] Envisat-1 mission CFI software mission conventions document, document PO-IS-ESA-GS-0561, Issue 2.0, GMV, S.A, Madrid, Spain, 1997. Available: [http://eop-cfi.esa.int/Repo/PUBLIC/DOCUMENTATION/CFI/ENVCFI/5.9\\_Documentation/mcd2.0.pdf](http://eop-cfi.esa.int/Repo/PUBLIC/DOCUMENTATION/CFI/ENVCFI/5.9_Documentation/mcd2.0.pdf)
- [17] Dragošević, M. V., and R. Ferrara, “Physical characterization and comparison of Doppler and attitude estimates for ENVISAT/ASAR and RADARSAT-1,” in *Proc. CEOS SAR Workshop*, Ulm, Germany, 27–28 May 2004
- [18] Envisat ASAR Monthly Report January 2010, ASAR ENVI-CLVL-EOPG-TN-04-0009, issue 47.0. Available: [https://earth.esa.int/sppa-reports/envisat/asar/monthly/2010-01-01/ASAR\\_Monthly\\_report\\_public\\_201001.pdf](https://earth.esa.int/sppa-reports/envisat/asar/monthly/2010-01-01/ASAR_Monthly_report_public_201001.pdf)

- [19] Recchia, A., A. Monti Guarnieri, N. Miranda, F. Collard, D. D'Aria, D. Giudici, "Impact of the antenna stability on the Doppler Centroid frequency," in *Proc. IGARSS*, Vancouver, Canada, 24-29 Nov. 2011, pp. 1516-1519
- [20] Kræmer, T., H. Johnsen, C. Brekke, and G. Engen, "Comparing SAR-based short time-lag cross correlation and Doppler-derived sea ice drift velocities," *IEEE Trans. Geosci. Remote Sens.*, Advanced online publication, doi:10.1109/TGRS.2017.2769222, 2018

Thanks a lot.

## References

- [1] D. V. Hansen and P. M. Poulain, “Quality control and interpolations of WOCE-TOGA drifter data,” *Journal of Atmospheric and Oceanic Technology*, vol. 13, pp. 900–909, Aug. 1996.
- [2] I. Koszalka, J. H. LaCasce, M. Andersson, K. A. Orvik, and C. Mauritzen, “Surface circulation in the nordic seas from clustered drifters,” *Deep-Sea Research I*, 2011.
- [3] P. Niiler, “The world ocean surface circulation,” in *Ocean Circulation and Climate* (G. Siedler, J. Church, and J. Gould, eds.), pp. 193–204, Academic Press, 2001.
- [4] K. A. Orvik and P. Niiler, “Major pathways of Atlantic water in the northern North Atlantic and Nordic Seas toward Arctic,” *Geophysical Research Letters*, vol. 29, OCT 1 2002.
- [5] R. M. Goldstein and H. A. Zebker, “Interferometric Radar Measurement of Ocean Surface Currents,” *Nature*, vol. 328, pp. 707–709, Aug. 1987.
- [6] R. Romeiser, S. Suchandt, H. Runge, U. Steinbrecher, and S. Gruenler, “First Analysis of TerraSAR-X Along-Track InSAR-Derived Current Fields,” *IEEE Transactions on Geoscience and Remote Sensing*, vol. 48, pp. 820–829, Feb. 2010.
- [7] D. R. Thompson and J. R. Jensen, “Synthetic-Aperture Radar Interferometry Applied to Ship-Generated Internal Waves in the 1989 Loch-Linnhe Experiment,” *Journal of Geophysical Research-Oceans*, vol. 98, pp. 10259–10269, June 1993.
- [8] B. Chapron, F. Collard, and V. Kerbaol, “Satellite synthetic aperture radar sea surface doppler measurements,” in *Proceedings of the Second Workshop on Coastal and Marine Applications of SAR* (L. H., ed.), European Space Agency, ESA Publications Division, Sept. 2003.
- [9] B. Chapron, F. Collard, and F. Ardhuin, “Direct measurements of ocean surface velocity from space: Interpretation and validation,” *Journal of Geophysical Research – Oceans*, vol. 110, pp. 7008–+, July 2005.
- [10] J. A. Johannessen, B. Chapron, F. Collard, V. Kudryavtsev, A. Mouche, D. Akimov, and K. Dagestad, “Direct ocean surface velocity measurements from space: Improved quantitative interpretation of Envisat ASAR observations,” *Geophysical Research Letters*, vol. 35, pp. 22608–+, Nov. 2008.
- [11] M. J. Rouault, A. Mouche, F. Collard, J. A. Johannessen, and B. Chapron, “Mapping the Agulhas Current from Space: an assessment of ASAR surface current velocities,” *Journal of Geophysical Research*, vol. 115, Oct. 2010.

- [12] M. W. Hansen, J. A. Johannessen, K.-F. Dagestad, F. Collard, and B. Chapron, "Monitoring the surface inflow of atlantic water to the norwegian sea using envisat asar," *Journal of Geophysical Research*, 2011.
- [13] M. W. Hansen, V. Kudryavtsev, B. Chapron, J. A. Johannessen, F. Collard, K.-F. Dagestad, and A. Mouche, "A Simulation of Combined Backscatter and Doppler Shifts of Wave-Current Interaction in the Presence of Strong Tidal Currents," *Remote Sensing of the Environment*, 2012.
- [14] M. Hansen, J. Johannessen, and R. R.P., "Mapping the Nordic Seas surface velocity using Envisat ASAR," in *Proceedings of ESA SeaSAR 2012*, 2012.
- [15] A. A. Mouche, F. Collard, B. Chapron, K.-F. Dagestad, G. Guitton, J. A. Johannessen, V. Kerbaol, and M. W. Hansen, "On the Use of Doppler Shift for Sea Surface Wind Retrieval from SAR," *IEEE Transactions on Geoscience and Remote Sensing*, 2012.
- [16] T. Kræmer, H. Johnsen, and C. Brekke, "Emulating Sentinel-1 Doppler Radial Ice Drift Measurements Using Envisat ASAR Data," *IEEE Transactions on Geoscience and Remote Sensing*, vol. 53, Dec. 2015.
- [17] F. Saïd and H. Johnsen, "Ocean Surface Wind Retrieval From Dual-polarized SAR Data Using the Polarization Residual Doppler Frequency," *IEEE Transactions on Geoscience and Remote Sensing*, vol. 52, July 2014.
- [18] C. Donlon, "ESA Data User Element (DUE) GlobCurrent User Requirement Document (URD)," tech. rep., European Space Agency (ESA), 2013.
- [19] A. Korosov, M. Hansen, K.-F. Dagestad, A. Yamakawa, A. Vines, and R. M., "Nansat: a scientist-orientated python package for geospatial data processing," *Journal of Open Research Software*, 2016.
- [20] M. W. Hansen, A. Korosov, A. Vines, T. Olaussen, and T. Hamre, "The nansen-cloud: a scientific platform as a service for the nansen group," in *Proceedings of the 2016 conference on Big Data from Space (BiDS'16)* (P. Soille and P. G. Marchetti, eds.), pp. 244–247, Publications Office of the European Union, 2016.
- [21] M. W. Hansen, F. Collard, K.-F. Dagestad, J. A. Johannessen, P. Fabry, and B. Chapron, "Retrieval of Sea Surface Range Velocities from Envisat ASAR Doppler Centroid Measurements," *IEEE Transactions on Geoscience and Remote Sensing*, 2011.
- [22] R. Bamler, "Doppler frequency estimation and the Cramer-Rao Bound," *IEEE Transactions on Geoscience and Remote Sensing*, vol. 29, 1991.
- [23] G. Engen and H. Johnsen, "Sentinel-1 Doppler and Ocean Radial Velocity (RVL) Algorithm Definition," tech. rep., Norut, 2015.
- [24] I. G. Cumming and F. H. Wong, *Digital processing of synthetic aperture radar data: algorithms and implementation*. Artech House, Inc., 2005.
- [25] G. Engen, H. Johnsen, and Y. Larsen, "Sentinel-1 geophysical Doppler product: performance and application," in *Proc. of EUSAR2014*, June 2014.

- [26] M. Portabella, A. Stoffelen, and J. Johannessen, "Toward an optimal inversion method for synthetic aperture radar wind retrieval," *Journal of Geophysical Research*, vol. 107, no. C8, 2002.
- [27] "The Global Drifter Program GDP Objectives." [http://www.aoml.noaa.gov/phod/dac/gdp\\_objectives.php](http://www.aoml.noaa.gov/phod/dac/gdp_objectives.php); accessed 2018-07-05.
- [28] R. Romeiser and D. R. Thompson, "Numerical study on the along-track interferometric radar imaging mechanism of oceanic surface currents," *IEEE Transactions on Geoscience and Remote Sensing*, vol. 38, pp. 446–458, Jan. 2000.
- [29] IDEAS SAR Team, "Envisat ASAR monthly report January 2010," tech. rep., European Space Agency, 2010. <https://earth.esa.int/sppa-reports/envisat/asar/monthly/2010-01-01/>; accessed 2018-03-21.
- [30] M. Mc Caig, "Envisat MERIS, GOMOS, ASAR & MIPAS in-orbit mispointing report," tech. rep., European Space Agency, 2002. <https://earth.esa.int/documents/10174/1591138/ENVI84.pdf>; accessed 2018-03-23.
- [31] M. Dragošević and R. Ferrara, "Physical characterization and comparison of doppler and attitude estimates for envisat/asar and radarsat-1," in *Proc. CEOS SAR Workshop, Ulm, Germany*, 2004.
- [32] G. W. Davidson and I. Cumming, "Signal properties of spaceborne squint-mode sar," *IEEE Transactions on Geoscience and Remote Sensing*, vol. 35, May 1997.